Laser Heating of Polymers

Dissertation

zur Erlangung des Grades

"Doktor der Naturwissenschaften"

im Promotionsfach Chemie

Fachbereich Chemie, Pharmazie und Geowissenschaften

der Johannes Gutenberg-Universität

in Mainz

Ralf S. Kappes

geboren in Landau in der Pfalz

Mainz, den 29.04.2012

Die vorliegende Arbeit wurde am
Institut für physikalische Chemie der Johannes Gutenberg-Universität Mainz
und am
Max-Planck-Institut für Polymerforschung in Mainz

in der Zeit von Februar 2009 bis April 2012 angefertigt.

Contents

Abstract

In order to investigate laser heating effects on polymers, a setup for temperature measurements was developed. Based on a high performance camera equipped with interference filters for spectral sensitivity, it is possible to acquire the spectral thermal emission from a laser heating process. By fitting Planck's law to the emission spectrum, 2D temperature graphs could be obtained with 1 µs time and 1 µm spatial resolution. In combination with finite element simulations, laser induced thermal ablation of various polymers could be analyzed. Photomechanical ablation was found at threshold for polymers with a glass transition between room and degradation temperature. Low ablation threshold temperatures, only several 10 K above the glass transition temperature were evident, i.e. at temperatures well below the degradation temperature of the polymers. At higher laser energies well above threshold, a thermal decomposition reaction took over as dominating ablation mechanism. The transition was found at higher temperatures in respect to standard thermogravimetric experiments due to the fast heating rates in agreement with the law of Arrhenius. For polymers maintaining their glassy state until degradation, photothermal decomposition takes place at threshold. For these polymers, the threshold was equally shifted according to the law of Arrhenius. At high laser power, high temperatures were measured, several 100 K above the threshold temperature. Experimental evidence suggests however, that a combination of different matter, decomposing polymer, oligomer, monomer, degradation products of the monomer and heated air is at high temperature. No evidence could be found for superheated polymer withstanding high temperatures on the 1 µs time scale, exceeding the prediction of Arrhenius as proposed by literature.

1 Introduction

1.1 Motivation

Nowadays, lasers are ubiquitous in science, industry and daily life, if it is for analytics, material processing or data transfer. In many of these applications, the laser light interacts with a polymer. The kind of interaction can be diverse. It can be a partial absorption of the laser beam in order to characterize or quantify a material, as it is the case for spectroscopy or photometric methods. But it can also be a chemical modification of the material up to ablation, i.e. the removal of material in order to engrave a logo or bar code into a surface of a product. The selectivity and reproducibility of the material interaction, especially with focused laser light, are key issues when using lasers.

Independent of the application, there is often a thermal component in the laser material interaction. This can be the main interaction, i.e. the laser is selectively heating the polymer or it can be a wanted or unwanted side effect. The latter is particularly the case for spectroscopic methods in science. The laser should only be the analytical tool, keeping the system of interest thermally undisturbed as far as possible. On the other hand, laser induced film formation via selective heating is used in industry for large scale printing. If a newspaper or magazine is produced nowadays, it is written and created digitally. Then, in a step called computer-to-plate, the information is transfered onto the printing plate. There are multiple technologies for this transfer on the market. One is schematically shown in figure 1.1. A film of a stable dispersion of polymer nano- or microparticles, also called latex film, including a dye is coated on a substrate. Then, the film is partially illuminated with laser light. The light absorbed by the dye heats up

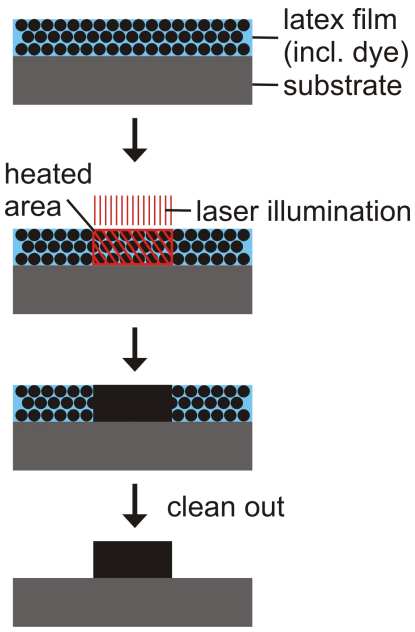

Figure 1.1: Simplified scheme of surface patterning by laser induced film formation.

the film and at the points where the temperature is high enough, the latex particles fuse together. In a following step, the "clean out", the unfused particles are washed away, leaving the polymer on the illuminated areas. The presence or absence of polymer film induces the necessary hydrophilic to hydrophobic contrast for the ink on press.

In order to assure fast processing speeds and good spatial resolution, the time scale and size scale for the computer-to-plate process has to be optimized. By now, illumination times around 1 µs and pixel sizes around 10 µm can be achieved. However, these achievements are based mostly on empirical studies due to the absence of fundamental understanding of heat transfer physics in the process. A temperature measurement method with the desired time and spatial resolution would be required. Knowing the temperature and understanding the physics might lead to further improvements, for example shorter illumination times and better pixel resolutions.

Temperature measurements on the time scale of 1 µs with size scales of 1 µm are challenging. Fundamental research with these orders of magnitude in the area of laser heating is also of high interest. High gradients can be generated. The extension of standard thermodynamics is therefore questionable. Extensive superheating of polymers,

i.e. exceeding the temperature of phase changes or degradation reactions drastically while the material remains metastable, is proposed in literature [1–4]. However, the proof for and the quantification of superheating as well as the influence of stress due to thermally induced expansion or pressure due to shock waves or the formation of gaseous products during the heating process are still problematic. The variety of setup or sample properties permits general statements. Calculations and predictions of laser heating behavior of polymers are therefore vague.

In this work, a temperature measurement based on spectral pyrometry [5] is introduced. The aim was a the time resolution of 1 µs and spatial resolution of 1 µm. It was applied to the laser heating of homogeneous dye-sensitized polymer films. The principle method of data analysis is discussed, as well as influences of systematic errors. The process of photothermally induced ablation, i.e. the removal of material due to laser heating, was analyzed for various polymers. Therefore, 2D temperature graphs and the time dependence of temperature were studied. Finite element simulations were conducted for verification of the measurement data. The influence of sample parameters such as film thickness and dye concentration could be interpreted with the simulations. In this way, it could be shown that stress generated due to laser heating played a significant role. Polymers undergoing glass transition when laser heated, were ablated at a temperature several 10 K above the glass transition, often well below the degradation temperatures at low, quasi-equilibrium heating rates. The hindered thermal expansion in the glassy state led to the generation of stress which was released at the transition point. First, surface deformations occured, but if a threshold input energy respectively a threshold stress was exceeded, material got removed from the surface and was ablated. On the other hand, it could be shown that, at laser input energies well above threshold, thermal decomposition of the polymer took place. High temperatures far above the degradation temperature at quasi-equilibrium time scales were reached. It is discussed if the polymer was superheated at this point, or if decomposing polymer fragments, monomers, fragments of the monomer or heated air were the detected, heated matter. Overall, processes and phenomena typical for microsecond laser heating are explained and set into physical

context to allow prediction of photothermal induced polymer behavior.

1.2 General Section

1.2.1 Laser

Lasers are ubiquitous in science, industry and daily life. Modern communications via fiber optics rely on them just like CD, DVD or Blue-ray player and many material processing or medical applications. The spectral purity and high, well adjustable power density of the laser light is the main reason for the use of lasers in these applications. The word laser is an abbreviation and stands for "Light Amplification by Stimulated Emission of Radiation". The process of stimulated emission is shown in figure 1.2 in context with absorption and spontaneous emission.

For absorption, an electron in a molecule is excited to a higher state by an incoming photon. This can only apply if the energy difference of the upper and lower state matches the energy of the photon:

$$h\nu = E_1 - E_0 \tag{1.1}$$

with the planck constant h, the frequency of light ν, the energy level of the ground state E_0 and the energy level of the higher state E_1.

On the other hand, excited electronic states show spontaneous emission. In this process photons are emitted with a frequency according to equation 1.1. The emission is random in propagation direction and phase of the emitted photon.

Stimulated emission occurs when incoming photons match the energy difference, but electrons are already in the higher, excited state. The incoming radiation field and the photons emitted by stimulated emission are coherent. They have the same frequency, propagation direction, polarization and phase. Therefore, the result is an amplification of the radiation field, the basic process to create laser irradiation.

Absorption and stimulated emission of the same energetic states correspond to each other in terms of quantum mechanics. The only difference is the initial condition, with the electron being in the low or high energy state. Consequently, the same rate is found for both.

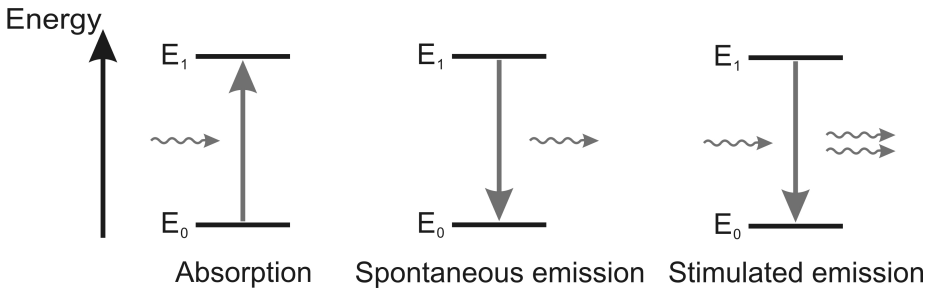

Figure 1.2: Scheme for absorption, spontaneous and stimulated emission.

In order to amplify the radiation field, population inversion is necessary. The population of the upper, excited state must exceed the population of the lower one. Otherwise the radiation field would be damped by the absorption of photons rather than amplified by stimulated emission. This is impossible to achieve for a two state system. Three or four energy states are necessary. Figure 1.3 shows the simplified scheme of energy levels for the active material in a four-level laser, discussed on the example of a Nd:YAG laser.

Neodymium YAG Laser

A Nd:YAG laser is a solid state laser. It consists of an yttrium aluminum garnet crystal which is doped with neodymium ions. The crystal is the matrix and transparent in the spectral range of laser operation. Neodymium, a transition metal, possesses electronic transitions in the 4f valence shell. These transitions are only slightly influenced by the matrix and show sharp transitions, similar to free atoms, and are well suitable for laser energy levels.

In order to gain population inversion, external energy needs to be introduced into the system. For lasers one generally speaks of "pumping energy into the system". This can be done for example via optical pumping with a conventional light bulb or another laser. The active medium is illuminated and excited from E_0 to E_P by absorption, from the ground state into the pumping level (figure 1.3). Only one transition is shown in the scheme, while typically a broad absorption band is chosen for efficient pumping. Then, the energy is converted in a non-radiative transition, typical a vibrational relaxation, into the upper laser level E_U. For efficient lasing, this state should show a high life time and

low rates of spontaneous emission or internal conversion in order to facilitate population inversion in respect to the lower laser level E_L. Once population inversion is established, spontaneous emission of few photons is sufficient to generate stimulated emission. The amplification enables the creation of the laser beam. The following transition into the ground state, E_L to E_0 is non-radiative, and preferably fast. In this way, population inversion can be achieved more efficiently and the material can be pumped again, starting a new cycle. Pulsed and continuous lasing is possible with the described four energy level system, depending on the kind and the extend of pumping.

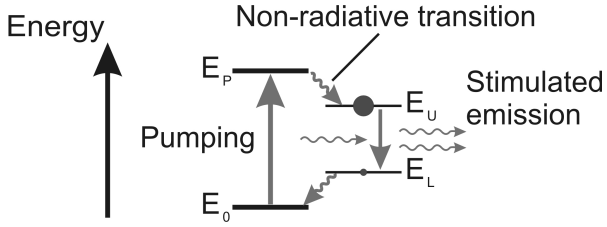

Figure 1.3: Simplified scheme of laser energy levels.

The major components of a laser are shown in figure 1.4. Three components, the active medium, an optical resonator and the energy pump are required. The optical resonator consists of two mirrors, a highly reflective and a partially reflective one. The case of two plane parallel mirrors, a Fabry-Perot resonator (figure 1.4) is the most simplest case. In applications, slightly concave mirrors are often used, because parallel alignment is easier to maintain. As described previously, population inversion is generated through pumping. In the case of the Nd:YAG laser, a diode laser pumps the active material optically. Once population inversion is achieved, spontaneous emission of light starts the laser. Only emitted photons with a propagation direction perpendicular to the mirrors are reflected and therefore kept in the optical resonator. Photons of other directions leave the resonator and do not participate to the laser beam. Stimulated emission is induced by the reflected photons and the radiation field is amplified. Through interference of the photons in the optical resonator, standing waves, also called modes, are developed. For continuous wave operation, a steady-state between pumping and laser output is reached after a certain time, i.e. a constant laser beam is generated.

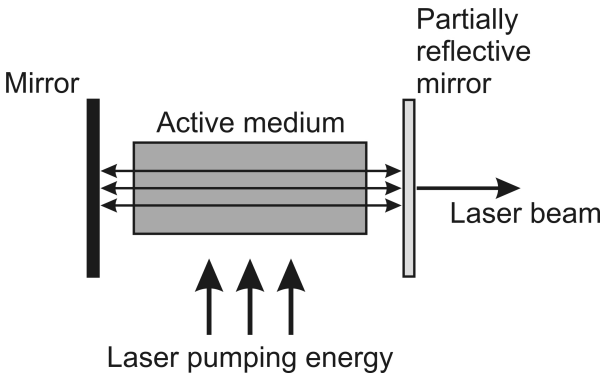

Figure 1.4: Principle of laser construction.

Laser diode

There are many other types of lasers, especially gas lasers like for example helium-neon, argon or exciplex lasers. One of the most cost-effective and widespread is the laser diode, typically built of doped gallium arsenide. The laser energy diagram analogous to figure 1.3 is shown in figure 1.5. Instead of discrete electronic states, continuous energy bands have to be considered. The working principle remains unchanged. Instead of an optical pumping, a potential is applied between the n- and p-doped part of the laser diode. In this way electrons are injected in the conduction band respectively holes in the valence band. Diode lasers are therefore also called injection lasers. In a non-radiative transition the lower part of the conduction respectively valence band is filled. The laser transition is generated analogous to the Nd:YAG laser, only that the generated laser emission follows the equation:

$$E_g < h\nu < F_C - F_V \tag{1.2}$$

Here, E_g is the band gap between valence and conduction band, F_V is the Fermi level of valence and F_C the Fermi level of the conduction band.

Figure 1.6 shows the working principle of a laser diode in a representation more common for semi-conductors. The Fermi level is constant through the p- and n-doped parts of the laser diode when no potential is applied (left graph). Due to the doping, the valence band is not fully occupied while the lower part of the conduction band is filled.

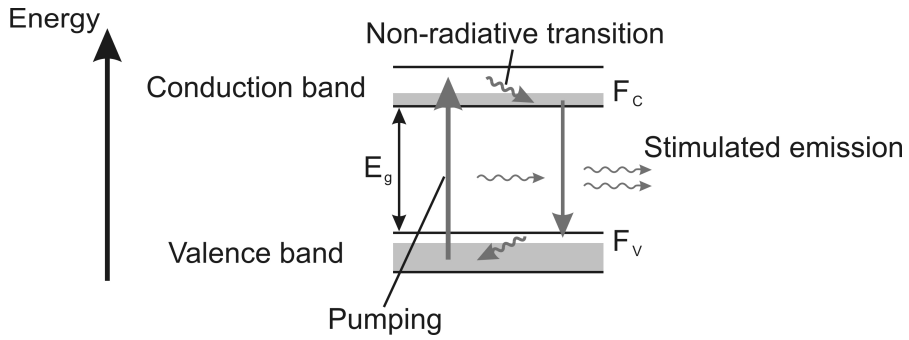

Figure 1.5: Laser energy bands in a diode laser.

Once a potential is applied the Fermi level splits up into F_V and F_C, i.e. the p-band is lowered and the n-band is elevated in energy. If the potential is high enough to promote electrons across the band gap (figure 1.6, right graph), valence and conduction band show population inversion in the active zone.

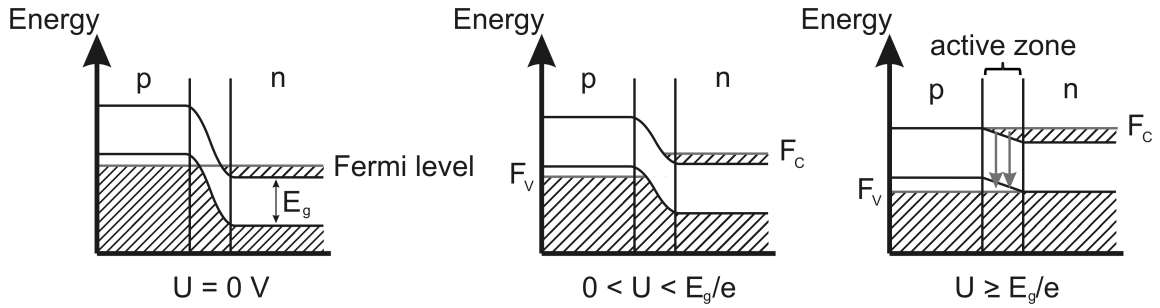

Figure 1.6: Laser diode p-n-transition at difference potentials. The stripes indicate occupation of the energy levels.

The schematic construction of a laser diode is given in figure 1.7. Two plan parallel lattice planes serve as optical resonator. The other two surfaces (drawing plane) are kept rough in order to scatter any emission in this direction out of the optical resonator and suppress any laser emission perpendicular to the drawing plane. The junction of the p- and the n-doped semiconductor is forming the active medium of the laser, for diode laser denoted as the active zone. The connection of both zones to a plus and a minus pole of a voltage source enables pumping and fulfills the last necessary component for laser operation as introduced in early in this chapter.

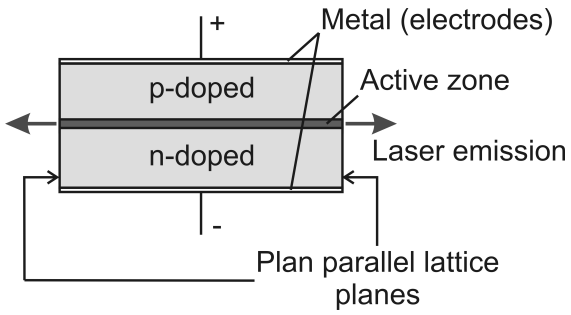

Figure 1.7: Construction of laser diode.

Compared to other laser systems, diode lasers show typically a broader laser emission band, due to the band structure of the energy levels, in contrast to the discrete electronic states of for example the Nd:YAG laser. The beam divergence is also rather high, up to 50°, so laser diodes are often combined with optical elements in order to create the desired beam structure. However, they are cheap in production and available for a broad range of wavelength which makes them popular in a lot of applications.

Pulsed laser

Lasers are nowadays one of the main tools to provide high power densities, i.e. a high amount of energy on a small area in a short time. In nuclear fusion science, laser systems in the order of 10^{18} to 10^{22} W/cm^2 have recently been reported [6]. For material processing, power densities in this range are not necessary. Still, high power density, especially short pulsed lasers are often desirable in order to minimize the thermal load on surrounding material or the substrate as well as to enhance the precision of the modification of the material by the laser radiation. One example would be the generation of microstructures by photothermal laser ablation. In principle there are two methods, which can also be combined, to achieve a short, high energy laser pulse: Q-switching and mode-locking.

Q-switched laser. Compared to the construction of a conventional laser (figure 1.4) the optical resonator is altered with an additional device, a Q-switch (figure 1.8). In this

example, a rotating prism is chosen, a mechanical Q-switch. The optical amplification is depending on the light entering the medium. When the prism is not in the position to reflect the light to the second mirror, the optical resonator is not closed. The light is not getting amplified and the laser does not turn on. The optical resonator possesses a low Q-factor and prevents feedback. The pumping of energy can go on past the level of saturation. Once the rotating prism is in the position to close the optical resonator, as shown in figure 1.8, the Q-factor rises. A large amount of energy is stored in the active medium at this point. Therefore the laser amplification builds up quickly and also depletes as quickly. The net result is a short pulse with high energy. With Q-switching, pulses in the order of 10 ns can be generated, with an energy in the order of 1 J, i.e. a pulse with a power of 100 MW [7].

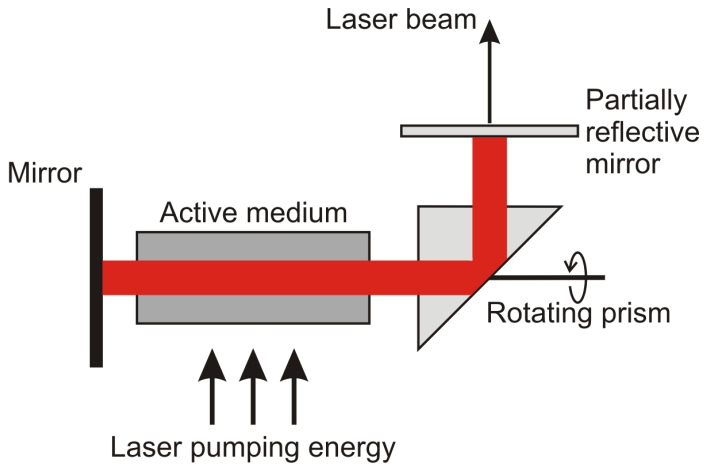

Figure 1.8: Construction of Q-switched laser with a rotating prism (mechanical Q-switching).

A mechanical Q-switching is not the only possibility. There are many others. One method is for example electro-optical Q-switching. Birefringence is induced in an optical material by an electric field, the so called Pockels effect. The electrical field is altered such that the Q-factor of the optical resonator rises suddenly, just like it is the case for the rotating prism. Often a faster transition from low to high Q can be obtained than for mechanical Q-switching.

Mode-locked laser. Another method to create short, high energy pulses is mode-locking. The principle can be understood regarding figure 1.9. Lasers do not create light of a single wavelength or frequency, but of a certain bandwidth or range of frequencies. Although compared to other light sources the bandwidth is typically small. The optical resonator rejects all longitudinal modes which do not follow the resonance criteria:

$$n \cdot \frac{\lambda}{2} = l \tag{1.3}$$

with $n = 1,2,3,...$, the wavelength λ and the length of the optical resonator l. The size of optical resonators is typically much larger than the wavelength of light. Therefore multiple modes are created and amplified in the optical resonator. In figure 1.9 eight exemplary modes are shown. The output is always the interference of the modes in the resonator. In the first row of figure 1.9, the output is generated out of only two modes, with slightly different wavelength. In this case the resulting wave possesses higher wavelength and amplitude. If eight modes are interfering with well defined phase difference and constant amplitude, a pattern presented in the second row of figure 1.9 can be obtained. High maxima are created besides smaller ones. The defined phase difference is crucial in this matter. If it is set arbitrary, no well defined pattern is found (third row). If both phase and amplitude are adjusted, the small maxima of the second row can also be suppressed (fourth row). Pulses of high intensity can be produced.

In general, lasers with a broad laser emission band are preferable for mode-locking. With a broader emission band, more modes can be brought into interference. Pulses in the range of 10 fs (10^{-15} s) can for example be generated in this way by a titanium-sapphire laser, with an emission band of about 300 nm [7].

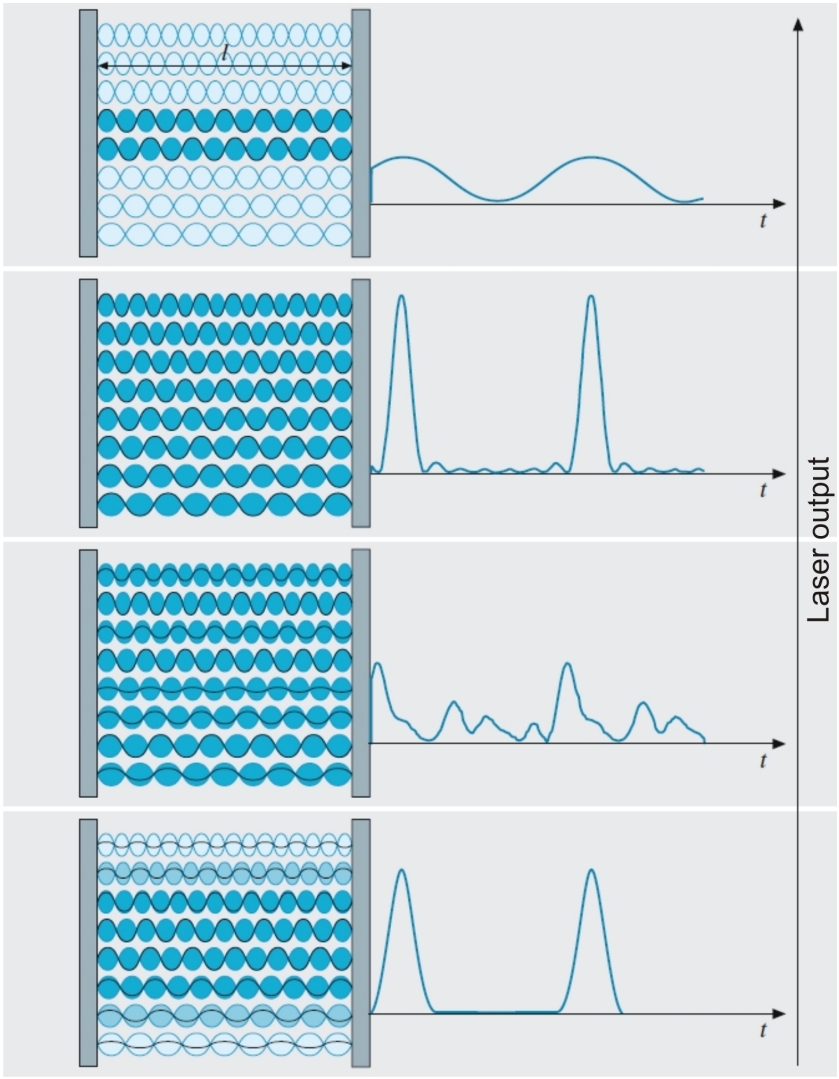

Figure 1.9: Example of mode-locking of eight resonator modes in an optical resonator with length l. On the left side, various modes are illustrated with the amplitude shown by the intensity of the blue scale and the phase by the black lines. On the right side, the corresponding output laser power versus time is given for the interference of the modes (according to [7]).

1.2.2 Light-polymer interaction

One type of laser light-matter interaction is absorption. Free electrons are excited in the case of metals respectively electronic or vibrational states for matter in general, taking up the laser energy [8]. Depending on the material and laser type, absorption is followed by the conversion of the energy into heat, a photothermal mechanism, or a chemical reaction is induced after excitation, a photochemical mechanism [9, 10]. The first is often additionally divided into a photomechanical mechanism for rapid, pulsed heating [1, 11, 12] when generated pressure or stress in the heated material play a significant role and the case when they do not. Material may be modified or removed by the laser irradiation. If material is removed, in general the term "laser ablation" is used, independent on the mechanism causing the material to be removed.

Photothermal mechanism

A photothermal mechanism is usually found for metals, but also for polymers at NIR or IR radiation. In the case of metals, excessive heating leads to desorption of the material through vaporization or sublimation. For high intensities, even ionization and plasma formation can be found. A vast number of applications is based on this mechanism of heating via laser light, for example joining and cutting of metals. The high reliability and precision of lasers are key issues in this regard.

In the case of polymers, the processes are often more complex, depending on the material, wavelength and time scale. Polymers do not simply vaporize but rather show thermal decomposition upon heating [13]. In general four classes of mechanism may appear: (1) random chain scission, (2) end-chain scission, sometimes also called "unzipping", (3) "chain-stripping", i.e. cleaving reactions in the side chain and (4) cross-linking [13]. The first two lead to lower molecular weights and formation of volatile species, oligomers or the monomer, which undergo vaporization. The last two lead, if solely occurring, to graphite like structure or char formation of the carbon based polymer. In this process, the loss of side chains facilitates the cross-linking between adjacent chains. The eliminated parts of the polymer are typically lost through the gas phase. Depending

on heating rates and the presence of oxygen or air, the reaction pathway often is rather complex, going along more than one class of mechanism. If glass transition or melting of the polymer occurs before decomposition, the influence on the reaction pathway must also be considered. The change in diffusion times of the polymer chains or fragments of reactive species respectively can be altered significantly.

In the case of polystyrene (PS), mainly random and end-chain scission is found in thermogravimetric experiments [14]. The gaseous products consists not only of monomers or oligomers. Further decomposition of the monomer takes place depending on the temperature. Besides styrene, carbon dioxide, water, benzene, toluene, xylene, benzaldehyde and methylstyrene could be identified by gas chromatography-mass spectrometry [15]. The special composition varies for polystyrene of different production routes or additives, if applied.

For laser ablation of polystyrene, studies at 248 nm [16] and 351 nm with PS including a doping agent [17] showed a photothermal dominated mechanism. The ablation products corresponded to the thermal decomposition products of thermogravimetric studies discussed above. In both studies, time-of-flight mass spectroscopy was used to identify the monomer and its degradation products. Additionally, in the case of the 351 nm irradiation, the velocity distribution of the ablated monomer could be fitted to a Maxwell-Boltzmann distribution at elevated temperatures underlining a thermally induced ablation [17].

In general, larger polymer fragments are generated and brought into the gas phase via photothermal laser ablation compared to low heating rate experiments like thermogravimetry. Depending on laser power density, monomer decomposition can be prevented. In this way, polymers can be brought into the gas phase and deposited as thin films on a receiving substrate. Resonant infrared pulsed laser deposition, RIR-PLD, makes use of this effect. A laser wavelength corresponding to vibrational transitions of the polymer is used to heat and ablate the material respectively fragments of the material into vacuum. A receiver substrate is set up to collect the ablated material. Various polymers like polystyrene [18], biodegradable polymers [19] or conducting poly-

mers [20] could be deposited with this technique. The structure and function of the polymer is maintained, only a reduction of molecular weight was found typically due to some inevitable fragmentation [4].

Arrhenius law

The temperature and the time scale are important parameters for thermally activated chemical reactions. The laser pulse duration is therefore crucial in addition to the temperature level reached. The law of Arrhenius connects both, the time scale and the temperature:

$$k_r = A_a e^{\frac{E_a}{RT}} \tag{1.4}$$

with the rate constant of the reaction k_r, the pre-exponential factor A_a, the activation energy E_a, the universal gas constant R and the temperature T. Faster reaction rates are reached for higher temperatures. On the other hand, higher temperatures are required for shorter time scales. In consequence, if experiments at low heating rates, like thermogravimetric experiments, are compared to pulsed laser heating, there should be a pronounced difference in reaction temperature. Unfortunately, quantification according to the law of Arrhenius is often difficult, especially for thermal decomposition reactions. Not only one reaction, but a cascade of reactions with different pathways occur. A determination of the activation energy is therefore difficult. Another complexity lies in the definition and quantification of the concentration that contributes to the rate constant, in particular for laser induced reactions. Qualitatively, Arrhenius' equation can however be applied in order to determine if a thermally respectively photothermally dominated mechanism is possible at a given temperature.

Photochemical mechanism

If UV laser radiation is used, polymers are often ablated by a photochemical mechanism. The principle can be understood regarding the energy level diagram in figure 1.10. Besides heating of the sample through internal conversion and the photothermal pathway,

a decomposition reaction can be induced by the excitation of an electronic state. The excited state is still bound at first because of the slow nuclear motion. The bonding energy level is however exceeded. Dissociation of the bond is therefore possible. Once a critical number of bonds is broken, material is ablated from the surface, accelerated by excess energy of the chemical reaction [21].

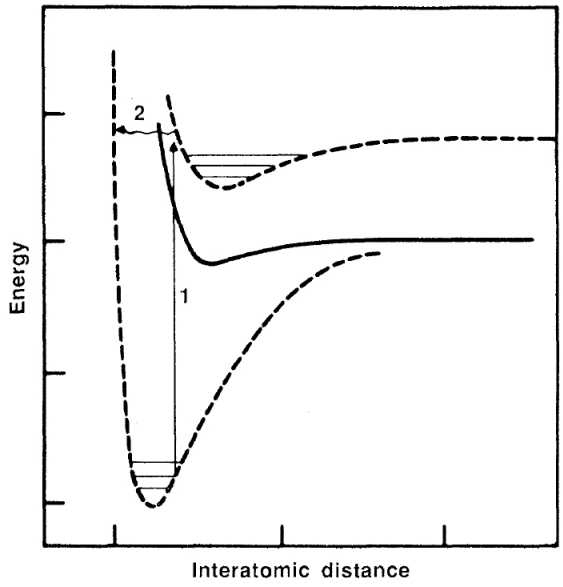

Figure 1.10: Energy level diagram for theoretical A-B bond. The lower dashed line represents the ground state, the other lines excited electronic states [21].

Details of photochemical decomposition reactions are often complicated, because several reaction pathways are possible. The analysis of ablation products from photochemical ablation yields, in contrast to a pure photothermal ablation, only small amounts of the monomer, depending on the polymer and the wavelength of the laser [16, 22]. Figure 1.11 shows a scheme of proposed reactions on the example of poly(methyl methacrylate) (PMMA).

The first reaction step after excitation of the monomer unit is the side chain scission, the so called Norrish type I reaction (figure 1.11, 1) [22]. This reaction is followed by carbon monoxide or carbon dioxide elimination respectively hydrogen abstraction (figure 1.11, 2). Then either the main chain is cleaved under double bond formation or

a double bond is formed along the main chain (figure 1.11, 3). Finally, the chain end radical unzipps, yielding the monomer (figure 1.11, 4). Even though photochemically induced, the temperature plays a crucial role especially in the last reaction step. For one radical only about 6 monomers are formed via this reaction at room temperature, while about 200 are formed above glass transition [23]. The low monomer fraction in the ablation products is therefore a direct indicator for a photochemical mechanism. Vice versa, if higher fractions are found, the photothermal contribution should not be neglected as it is case for example for PMMA at 308 nm [23].

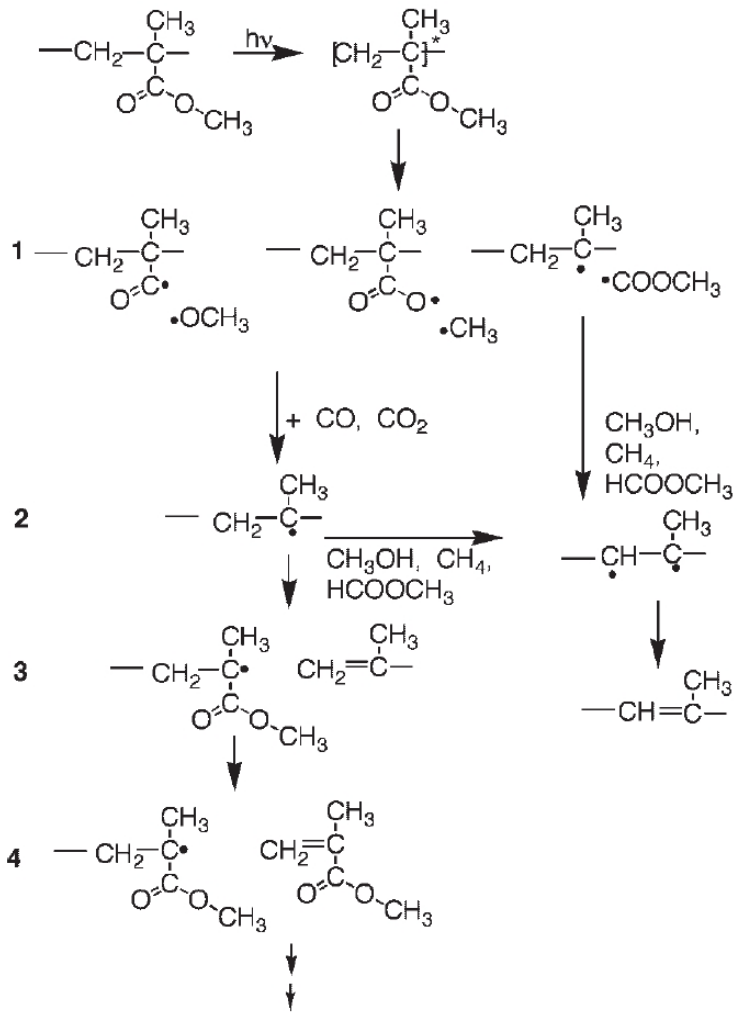

Figure 1.11: Photochemical decomposition mechanism for poly(methyl methacrylate) [22].

Photomechanical mechanism

Pressure or stress generated by the laser material interaction may often not be neglected. If it dominates the mechanism is said to be photomechanical. The fast time and small size scales which can be achieved by laser heating and therefore high temperature gradients are the main cause for photomechanical degradation. In literature, examples can be found for refractory materials like titanium or titanium nitride at up to 10 µs pulse time scale [11], for biological tissue [12] and PMMA at NIR wavelength laser irradiation with 100 ps pulse time scales [1].

A scheme of photomechanical ablation on the example of a solid thin film is shown in figure 1.12. Two different cases can be defined. In the first, shown in figure 1.12 (b), the laser pulse heats the material isochorically. This occurs if the pulse duration is shorter than the time for thermal expansion. As long as enough energy is provided in order to exceed the adhesion energy E_{adh}, material is ablated and scattered away from the substrate. If not enough energy is provided, the surface will only be deformed or cracked after the laser pulse. This case is called shock-assisted ablation. In the second case, shown in figure 1.12 (c) to (e), for pulse duration longer than the time for thermal expansion, surface deformation occurs during the laser pulse. The stress generated by this deformation can built up during the pulse and also lead to ablation if the adhesion energy is exceeded. This case is called stress-assisted ablation.

NIR laser ablation of titanium and titanium nitride are good examples for the latter case. Figure 1.13 presents time-resolved micrographs for titanium nitride irradiated with a laser pulse of 110 ns from a Q-switched Nd:YAG laser. The coating is expanding from the surface in the first 20-30 ns before it breaks away. The white parts in the center of the transmission images indicates the development. The transmission of the coating lies in the order of few per cent. Once it is ablated, the transmission increases drastically. On the other hand, the expansion of the layer can well be followed in the first three images with grazing incident. The melting point of titanium nitride at standard pressure is 2930°C [11]. Even with the higher stress due to fast expansion, the material is not melting but cracks and breaks apart when ablated from the surface. Titanium

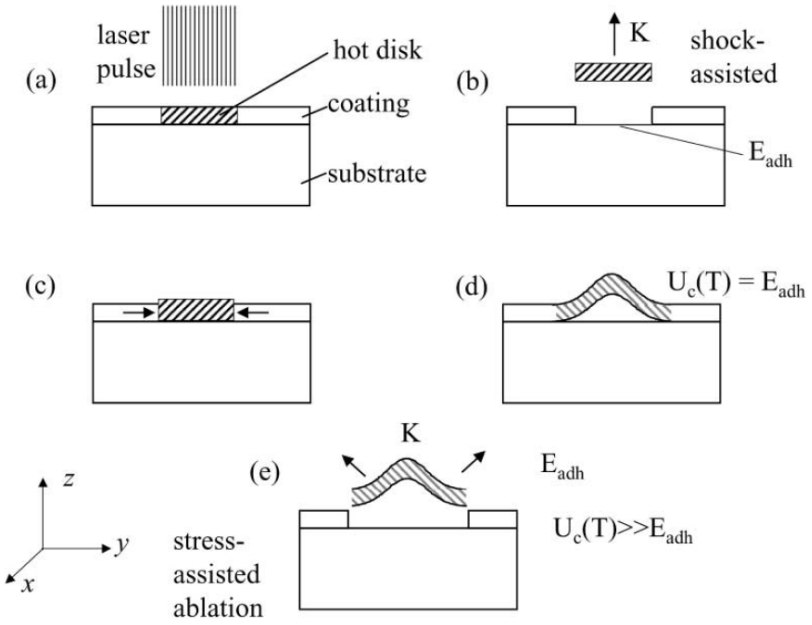

Figure 1.12: Photomechanical decomposition mechanism [11].

with a melting point of 1675°C in contrast shows partially melting at corresponding laser settings [11].

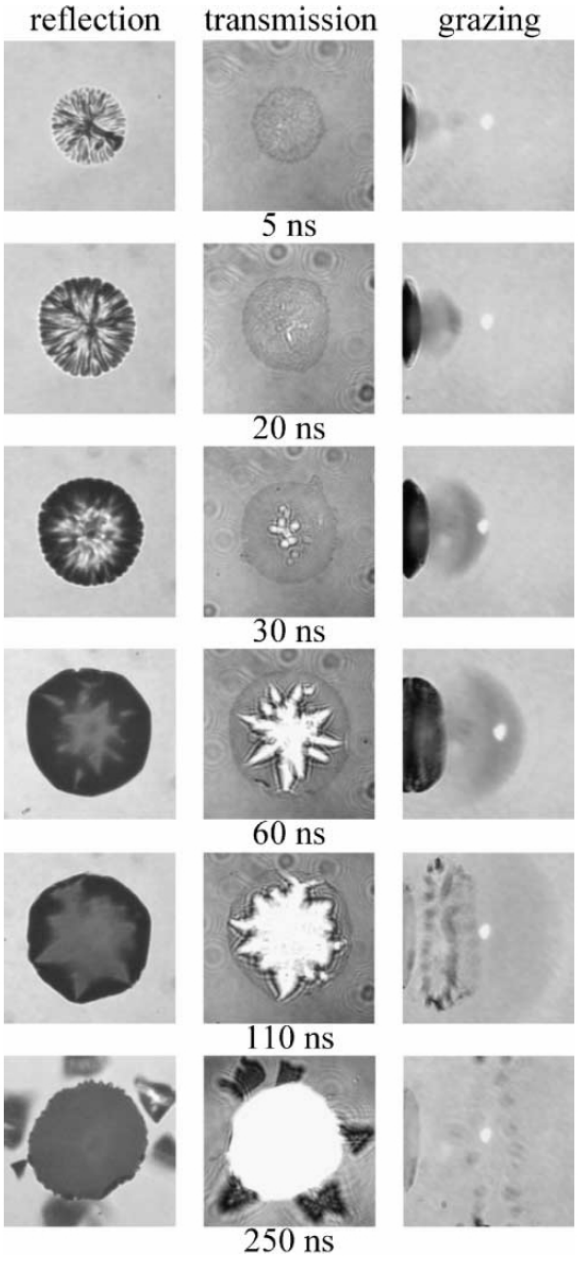

Figure 1.13: Time-resolved micrographs of photomechanical ablation of titanium nitride film on glass by 110 ns laser pulse. Each image shows 60 × 60 µm^2 with light source and detector in reflection, transmission and grazing incidence configuration ([11] respectively [24]).

In order to find out if a shock- or stress-assisted mechanism is applicable, the following equation can be used according to Hare et al. [1]. For small strains ($\delta x/x << 1$) the inertial confinement time τ_h can be calculate in the acoustic approximation:

$$\tau_h = \frac{d}{c_{ac}} \tag{1.5}$$

with the film thickness d and the acoustic velocity c_{ac}. The calculated time can then be compared to the laser pulse duration.

The time scale for inertial confinement in the case of titanium or titanium nitride can be found in the order of 10 ps [11]. Thus, in agreement with the results of the time-resolved microscope studies showed above, the condition necessary for a shock-assisted mechanism is not fulfilled with a 110 ns laser pulse. For PMMA and a NIR laser which is Q-switched and mode-locked to generate pulses of 150 ps, it is [1]. In this case the increase in temperature and pressure must be included into thermodynamic calculations in order to explain the phenomenon quantitatively.

The expansion of a polymer can also be visualized by time-resolved interferometry for example for PMMA [25]. Figure 1.14 shows the interference fringes of such an experiment with a 30 ns laser pulse at 248 nm laser irradiation with an energy of about 1/3 of the ablation threshold energy. The expansion is delayed in respect to the laser pulse. Indeed it is still visible long after the pulse at a delay time of 5 µs. And it is completely reversible at the applied energy. These experiments indicate, that a photomechanical contribution can not be neglected.

Laser energy distribution

The intensity and therefore absorption profile is important for laser induced processes. It determines how much energy is available for a certain volume at a given time. For an incident light on matter, the law of Lambert-Beer describes the decrease of the light intensity perpendicular to the surface. The intensity cross-section in plane is determined by the applied optics. In the case of lasers, optics forming a Gaussian or a flat-top cross-section profile are typically used. According to [9], the intensity as a function of space

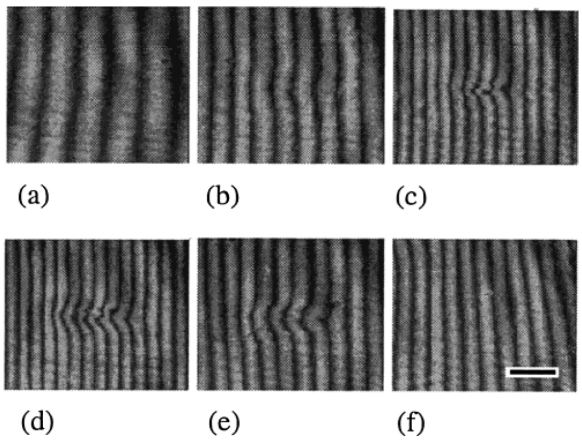

Figure 1.14: Nanosecond time-resolved interferometric images of laser heated PMMA below the ablation threshold. Presented are the images for the delay times of $-\infty$ (a), 29 ns (b), 71 ns (c), 5 µs (e) and $+\infty$ (f) in respect to the peak of the 30 ns laser pulse. A fringe shift to the left represents an expansion. The scale bar indicates 1 mm [25].

and time $I(x, y, z, t)$ follows in general the equation:

$$I(x, y, z, t) = I_p(t) I_{sp}(x, y)(1 - R)e^{-\alpha z} \tag{1.6}$$

with the pulse shape in time described by I_p, the beam cross-section at the materials' surface I_{sp}, for example a Gaussian function in x and y (Gaussian beam), the reflectivity R and the absorption coefficient α.

If ablation occurs and the sample is illuminated by the laser on the front side, equation 1.6 is not strictly valid any longer. An additional loss by the absorption of the evolving plume, i.e. the material which is removed from the surface, needs to be accounted. An example of the development of such a plume can be seen in figure 1.13 for titanium nitride in the grazing incident micrographic images. The plume is typically even more pronounced, especially for polymers [4]. The intensity is additionally reduced due to partial absorption of the laser light. This effect is therefore called "plume shielding" [26]. The plume can be used in order to analyze the laser ablation process [4, 16, 17, 27–29]. For calculating the intensity profile, it is however often neglected. Quantification of

plume formation for example by simulation would be necessary in order to account it in a correct way.

The absorption coefficient in equation 1.6 is important for the process. The so called penetration depth $1/\alpha$, the depth at which the intensity is reduced to 1/e, enables a good estimation of the vertical intensity distribution. For small penetration depths, surface absorption can be assumed. This is typical for example for metals with penetration depth in the order of 1-10 nm [9]. As long as the film thickness of the illuminated material is not in the same range, the depth dependence of the intensity in equation 1.6 can then be neglected. In contrast, for large penetration depths in the order of several µm or more the absorption of the volume and its depth dependence must be accounted [30], especially if the film thickness ranges in the order of the penetration depth [26].

Laser induced forward transfer

A method of particular interest in the field of laser material interaction is **l**aser **i**nduced **f**orward **t**ransfer, LIFT (figure 1.15). A laser is focused on the backside of a donor film through a transparent substrate. Induced by the laser pulse, the donor film is lifted of the carrier substrate and accelerated toward the receiver substrate, which is placed behind a typically µm sized gap. The process was first applied in 1986 for copper deposition [31]. Nowadays, it is a versatile tool for the transfer of various materials. Brittle oxids [32], functional organic light emission diode pixels [33], living cells [34] or liquid like glycerol water mixtures [35] could for example be transfered by LIFT.

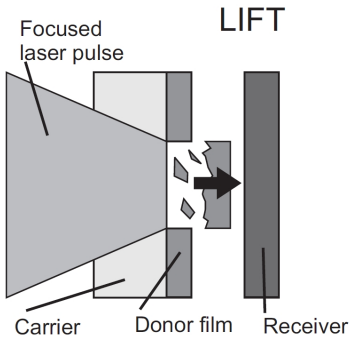

Figure 1.15: Scheme of classical laser induced forward transfer [32].

Depending on the material, different strategies are developed in order to assure a good transfer. Figure 1.16 is giving an overview. In the traditional LIFT, the transfered material itself is heated and accelerated from the carrier to the receiving substrate. Some thermal damage and scattering of the material are therefore inevitable. In order to avoid these disadvantages, an additional layer can be introduced underneath the material of interest for transfer (figure 1.16 (b)). This layer can either be an energy absorbing layer, which is taken the part of light absorption and conversion into heat, or it can be a dynamic release layer. The first is transferring the heat onto the donor material, protecting the material only from direct laser radiation. The latter, a dynamic release layer, is designed to decompose upon laser irradiation into gaseous products, propelling the material onto the receiver substrate. In this way the thermal damage can be minimized and very brittle or sensitive samples can be transfered [32, 33]. If the material would moreover be damaged by the acceleration for transfer, a matrix can be added (figure 1.16 (c)). LIFT is not restricted to the transfer of solid films. Liquids can be transfered as well. The laser settings and sample properties need to be adjusted corresponding to the viscosity of the system to assure a good transfer [36]. With the combination of the dynamic release layer and the matrix method, Chrisey et al. were for example able to transfer stripes of living cells via LIFT [34].

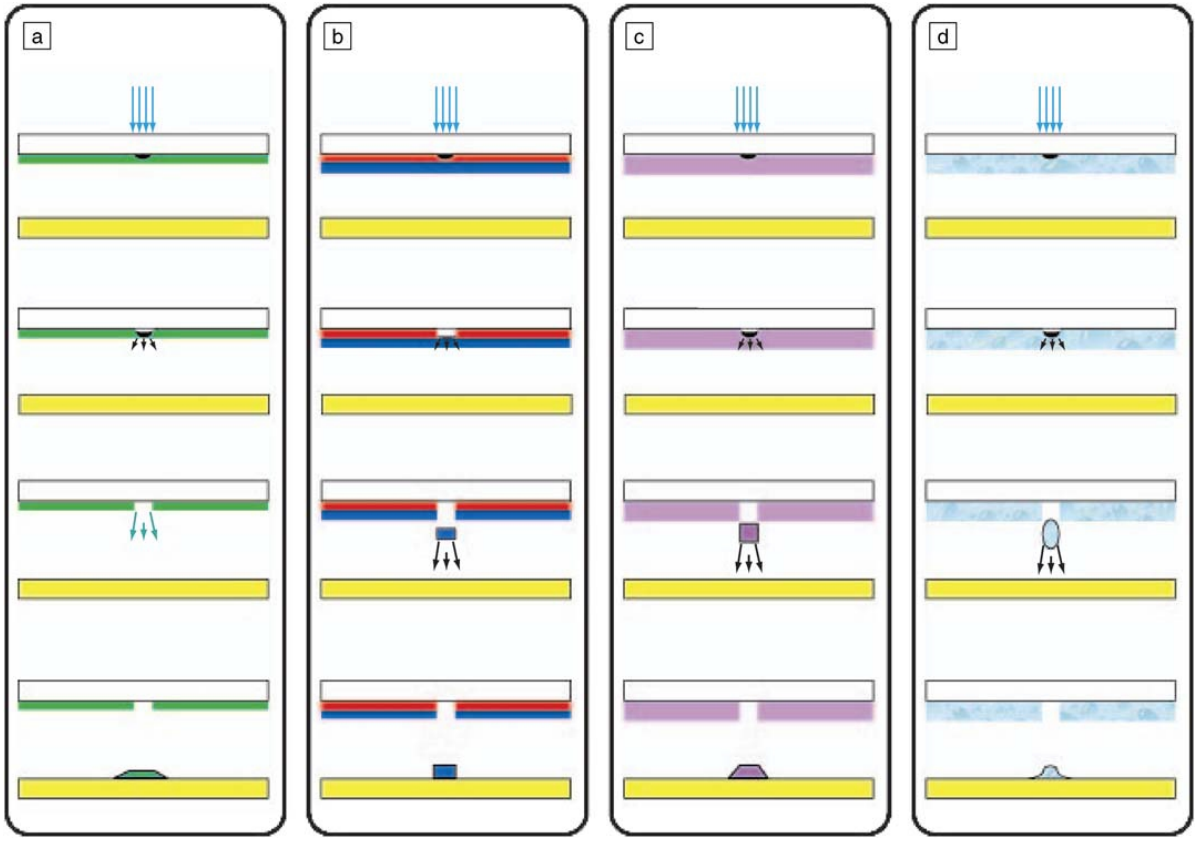

Figure 1.16: Scheme of different strategies in laser induced forward transfer. Traditional LIFT (a), LIFT with energy absorbing or dynamic release layer (b), matrix assisted LIFT (c) and LIFT of rheological system (d) [37].

A material applied for dynamic release layers is the aryltriazene polymer (figure 1.17). The triazene group in this polymer can be cleaved photochemically, for example with 308 nm laser irradiation, but also thermally, if the temperature exceeds about 250°C. In both cases, the triazene group decomposes into nitrogen and radical intermediates. The main chain of the polymer is going along the triazene group, i.e. the polymer is fragmented in this reaction. In further reaction steps, low molecular mass polymer fragments as well as gaseous and volatile products are formed which leave the reaction through the gas phase. This is advantageous, because in LIFT the receiver substrate should not be contaminated with residues from the dynamic release layer. The formation of nitrogen provides the thrust to accelerate the flyer, the material to be transfered.

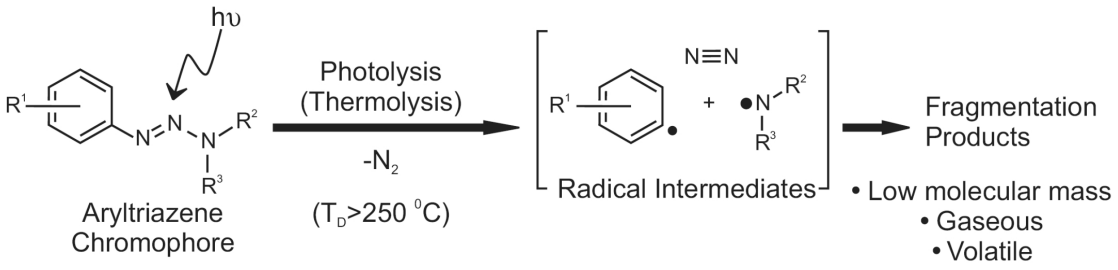

Figure 1.17: Scheme of decomposition reaction of triazene polymer. The polymer backbone goes along R^1 and R^2 [32].

1.2.3 Basics of heat transfer

In principle, heat transfer is described by three different mechanisms: conduction, convection and radiation (figure 1.18). In conduction, only thermal energy is transported. In convection, a mass transport is connected with the heat transfer. When for example a liquid or gaseous phase is flowing over a surface with different temperature, heat is transfered to or from the surface by the fluid. Convection can also be induced by a heated surface. A preexisting flow is not required. In general, the terms natural or free convection is used if a flow is induced by the heat transfer. Forced convection is used

for a preexisting flow. Finally, matter emits electromagnetic radiation according to its temperature. Matter of higher temperature emits more energy. Consequently, there is a net heat transfer from matter of higher temperature to matter of lower temperature.

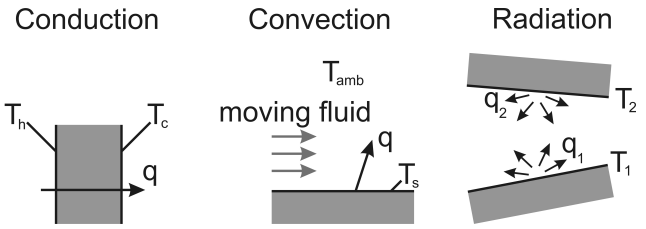

Figure 1.18: Scheme illustrating the different heat transfer mechanisms (according to [38]).

Conduction

Conduction is in general described by the heat conduction equation:

$$\frac{\partial T}{\partial t} = K\nabla^2 T + Q_{extern} \tag{1.7}$$

with temperature T, time t, the heat input or output from or to an external source Q_{extern} and the thermal diffusivity K. In a cartesian coordinate system with the temperature and the heat input respectively output as a function of x,y,z and t, this can also be written as:

$$\frac{\partial T}{\partial t} = K\left(\frac{\partial^2 T}{\partial x^2} + \frac{\partial^2 T}{\partial y^2} + \frac{\partial^2 T}{\partial z^2}\right) + Q_{extern} \tag{1.8}$$

The thermal diffusivity can be expressed by the thermal conductivity k_{mater}, the density ρ and the heat capacity at constant pressure c_p:

$$K = \frac{k_{mater}}{\rho c_p} \tag{1.9}$$

In order to determine the temperature distribution as a function of space and time, a solution must be found for the differential heat conduction equation. Finding an analytical solution is often demanding, sometimes even impossible. Numerical methods have

to be applied in this case. The method of finite element simulation (further described in chapter 1.2.4) is in many applications the best way to solve the problem.

Convection

In the case of convection, the movement of particles in a liquid or gas determines the rate of heat transfer. Two cases are in general distinguished: diffusion, i.e. Brownian motion, and macroscopic flow. Diffusion can be described with the diffusion differential equation:

$$\frac{\partial c_i}{\partial t} = D\nabla^2 c_i \tag{1.10}$$

with the concentration of the diffusing species c_i, time t and diffusion coefficient D. This equation is formally equal to the differential equation for heat conduction (equation 1.7) except for the lack of the second term on the right side. Temperature is just exchanged by the concentration.

The description of bulk, macroscopic flow, i.e. the collective motion of a large number of molecules, is very complex. The geometry is crucial, as well as if forced or free convection is present. For example, forced convection of a fluid parallel to a planar, heated surface, typically induces laminar heat flow close to the surface. This can be quantized rather well. However, further away from the surface the flow gets disturbed and turbulent, making a calculation difficult.

Therefore, a description with material flow is only conducted if necessary. If convection is taken into account, finite element simulations represent a feasible, well applicable method, analogous to heat conduction. Nevertheless, the following simple equation is used more often to describe convective heat flux from a surface to a fluid:

$$q = h_{tc}(T_s - T_{amb}) \tag{1.11}$$

Here, h_{tc} is the heat transfer coefficient, T_s is the temperature of the surface. T_{amb} is the temperature of the fluid far away from the surface. Hence, the problem is reduced to

process	h_{tc} [W/(m^2 K)]
Free convection	5-25
Forced convection (gases)	25-250
Forced convection (liquids)	50-20000
Convection with phase change (e.g. boiling)	2500-100000

Table 1.1: Overview of heat transfer coefficients for convection. (according to [38])

determination of a heat transfer coefficient, which fits the problem. Table 1.1 is giving an overview of heat transfer coefficients for different processes.

Radiative heat transfer

Every matter at finite temperature emits radiation. The theory of black body radiation is describing the wavelength and temperature dependence of the radiation. According to Planck's law the spectral radiance $\tilde{M}$ as a function of wavelength λ and temperature T is given by:

$$\tilde{M}(\lambda, T) = \frac{2\pi hc^2}{\lambda^5} \frac{1}{\exp(\frac{hc}{\lambda kT}) - 1} \tag{1.12}$$

with the Planck constant h, the speed of light c and the Boltzmann constant k. The spectral radiance describes the transfered power per area for a wavelength respectively wavelength interval. The typical unit for the spectral radiance is given by W/(m$^2 \cdot$ nm).

The distribution of emitted photons of wavelength λ of a black body at temperature T is given by the specific spectral radiance M. It can be derived when equation 1.12 is divided by the photon energy.

$$M(\lambda, T) = \frac{2\pi c}{\lambda^4} \frac{1}{\exp(\frac{hc}{\lambda kT}) - 1} \tag{1.13}$$

with the unit Photons/(s $\cdot$ m$^2 \cdot$ nm).

However, equation 1.13 is only valid for the physical idealized "black body", i.e. matter that absorbs all incident electromagnetic radiation. The emitted radiation from a black

body depends only on its temperature. For real matter, an additional parameter, the emissivity ϵ, must be introduced into equation 1.13:

$$M(\lambda, T) = \frac{2\pi c\epsilon}{\lambda^4} \frac{1}{\exp(\frac{hc}{\lambda kT}) - 1} \tag{1.14}$$

The emissivity in this equation is a number between 0 and 1. It reflects, how much the emitting matter resembles the idealized black body. Just like the spectral radiance, it is typically wavelength and temperature dependent. If the emissivity respectively its dependence on wavelength and temperature is unknown, it is often set to one, the so called "black body approximation" or set constant, "grey body approximation" (further discussed in chapter 1.2.5).

The radiative heat flux is described by the Stefan-Boltzmann law:

$$q = \epsilon_g \sigma T^4 \tag{1.15}$$

with the integrated emissivity ϵ_g, the Stefan-Boltzmann constant
$\sigma = 5.67 \times 10^8$ W/(m^2 K^4) and temperature T of the emitting matter. The emissivity in the Stefan-Boltzmann law is equal to the emissivity in equation 1.14, but integrated in respect to the wavelength.

For two opposite walls at temperature T_h and T_c separated by vacuum the heat flux is given by:

$$q = \epsilon_g \sigma (T_h^4 - T_c^4) \tag{1.16}$$

In contrast to conduction or convection, the heat flux is depending on the temperature to the power of four. As a consequence, radiative heat transfer becomes more dominating for higher temperatures.

Radiation differs also in another point from conduction and convection. No medium is required for radiative heat transfer. For the life on our planet this fact is very important. The energy from the sun is transported via radiation heat transfer to the earth and enables life on our planet.

1.2.4 Finite element simulations

The finite element method is a technique to solve partial differential equations, like for example the heat equation (equation 1.7) or integral equations with a numerical approximation. The matter of interest is therefore divided in a finite number of elements. In these elements, functions are applied in order to find approximate solutions in combination with the starting and the boundary conditions.

In order to solve the numerical problem, computer programs like Comsol Multiphysics (www.comsol.de) can be applied. The following example of a light bulb which is switched on, illustrates the method (built according to the tutorial model "Free Convection in a light bulb" from the Comsol model documentation).

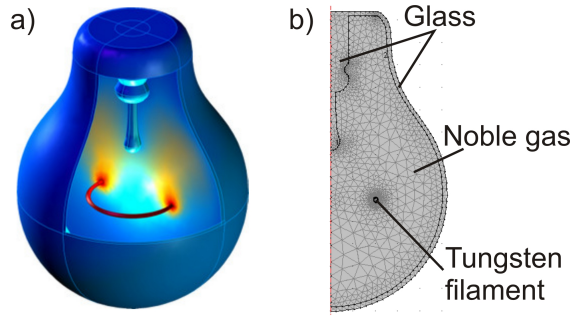

Figure 1.19: Example for finite element simulation: Light bulb. 3D illustration of a light bulb (a) and simplified 2D model including the finite element mesh (b) (according to www.comsol.de).

The principle geometry of a light bulb is presented in figure 1.19 (a). The problem is rotationally symmetric. Therefore it can be simplified to a 2D model, exploiting the symmetry (figure 1.19 (b)). A mesh is generated, i.e. the geometrical structure is divided in a finite number of elements. In principle, the approximation with smaller element sizes results in a higher quality of the approximation. At the same time, the computing time increases. An optimum between element sizes and computing time must therefore be found. Interphases, especially if curved or consisting of edges, are typically divided in smaller parts, as can be seen in figure 1.19 (b). At these points higher gradients are prevailing, leading to a more pronounced change in the physical relevant parameters, for

example in the temperature. The mesh type and size can be very important to find a good approximation. Several attempts with different mesh type and size are often used for the same problem, to make sure, that the choice of mesh does not affect the result.

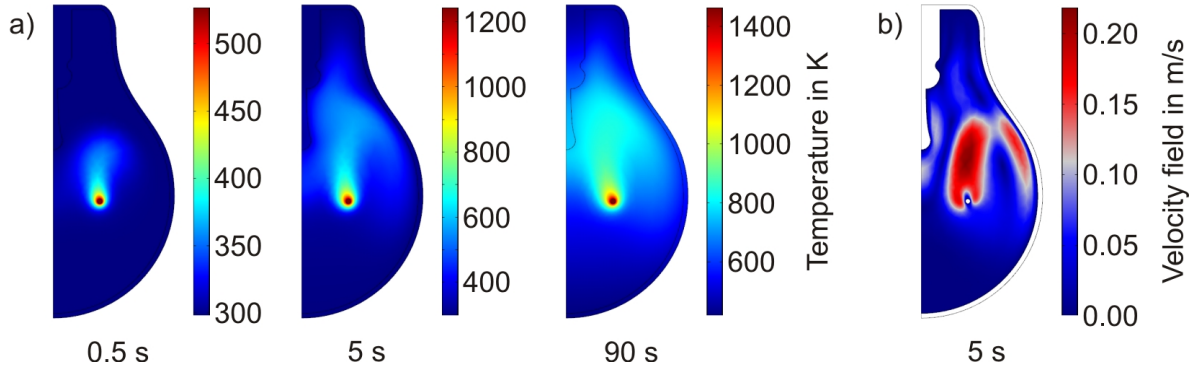

Figure 1.20: Temperature distribution in a finite element simulation of a 60 W light bulb. Temperature profile (a) for 0.5, 5 and 90 s after the light bulb is switched on and velocity field of the convection (b) for 5 s.

The simulated temperature distributions for several delay times after the light bulb is switched on are presented in figure 1.20. It illustrates how the temperature increases in the first seconds after the light bulb is switched on. In this example, conductive, convective and radiative heat transfer play a role. All contributions can be accounted for by simulations. The velocity field for the convection in the light bulb is also plotted in figure 1.20. In combination with the temperature distribution, it is obvious that the convection is contributing significantly to the heat transfer. Otherwise a more radial temperature distribution would be expected.

1.2.5 Temperature measurement

The temperature is an important parameter for many processes. There are multiple ways to measure the temperature, for example a resistance or a mercury thermometer. Important for a thermometer is a reliable and well reproducible dependence of a certain property from the temperature. In the examples named before, these would be the electrical resistance and the volume of mercury in the thermometer. Both methods of temperature measurement and many others are applied nowadays. However, there are still challenges if it comes to temperature measurements, especially for small size scales and short time scales. One way is the combination of scanning force microscopy with means of temperature measurements, the so called scanning thermal microscopy [39].

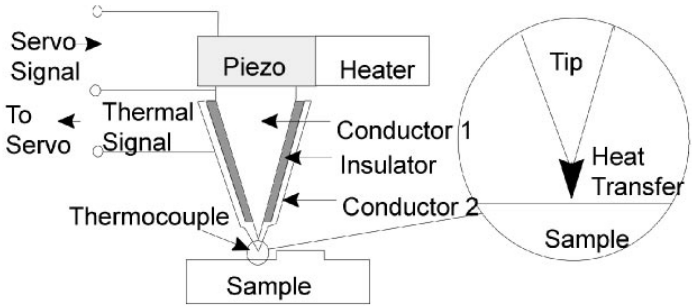

Figure 1.21: Scheme of scanning thermal profiler based on a coaxial thermocouple on the tip [39].

Figure 1.21 shows the scanning thermal profiler originally published by Williams et al. [40]. The tip of an atomic force microscope is modified to form a thermocouple in a coaxial configuration. The first conductor can be found at the inner part of the tip, the second is surrounding the tip. Both conductors are separated by an insulator, besides on the tip itself. A tip size of about 100 nm could be realized. A change in temperature of the sample can be followed by the change in potential between the two conductors in the tip, if it is located in close proximity to the sample surface. Absolute temperature measurements can also be realized, after appropriate calibration. The heat conduction of the tip is however significantly influencing the sample surface temperature. Therefore,

the tip sample gap is typically maintained constant through a feedback control system.

The original purpose of the setup was actually not to measure surface temperatures, but high resolution surface profiles of insulating materials. Therefore, the thermocouple sensor in the tip was brought to a different temperature than the sample by Joule or Peltier heating/cooling. The thermal resistance between tip and sample was used analogue to the tunnel current in scanning tunneling microscopy to keep a constant distance. A lateral resolution was in the order of the tip size, about 100 nm. A depth resolution of 3 nm could be achieved in this way [40]. The application for measurements of surface temperatures was evolved later [39].

If the surface temperature is probed by scanning thermal microscopy, the tip represents an additional heat sink. The surface temperature is lowered significantly, depending on the tip-sample distance. The heat transfer must therefore be considered for the interpretation of the data. Fundamental knowledge of the heat transfer is required. Through a calculation or simulation, undisturbed surface temperature of the sample can however also be obtained [39].

Spectral pyrometry

Another method to determine the temperature on small scales or at fast time scales is spectral pyrometry, sometimes also called optical pyrometry. In principle, it incorporates all techniques which use the similarity of the emission spectrum to the black body spectrum to determine the temperature [5]. The typical spectral range is 200 to 1100 nm, i.e. the visible part including UV and NIR radiation.

If talking in general about pyrometry, there is no limitation of the range of wavelengths. Devices nowadays often applied in industry and daily life make for example use of IR radiation in order to extend the temperature range to low temperatures down to -30°C. However, although based on the same physical principles, other physical parameters are relevant for these devices than it is the case for spectral pyrometry. These devices are therefore not included or discussed in this chapter.

The typical setup of a spectral pyrometer consists of a spectrometer, for example a

diffraction grating spectrometer [41] or a system containing multiple spectral selective filters and photodetectors [42, 43]. Additionally, a heating device, for example a laser [44] or a device to excite the material of interest is included. This can also be a microwave pulse to start a chemical reaction [41] or a light-gas gun to study high pressure heating phenomena [42, 43].

Theoretical background. Black body radiation is described by Planck's law, already introduced in chapter 1.2.3 (equation 1.13 and 1.14). In order to determine the temperature, the measured emission spectrum is fitted with Planck's law:

$$n_p(\lambda, T) = \frac{A}{\lambda^4} \frac{1}{\exp(\frac{hc}{\lambda kT}) - 1} \tag{1.17}$$

Here, n_p is the number of photons per wavelength or wavelength interval for a given temperature. A is the fitting parameter, which includes a constant emissivity according to the grey body approximation. It is important to notice, that with this approach, the same temperature is resulting from the fit for a black and a grey body approximation.

Depending on temperature and wavelength, three different regions can be identified in the description of thermal emission: the Wien, the Transition and the Rayleigh-Jeans region.

Wien region For short wavelengths and low temperatures, or more generally for $hc/\lambda kT \gg 1$, the denominator in equation 1.17 can be simplified:

$$n_p(\lambda, T) = \frac{A}{\lambda^4} \frac{1}{\exp(\frac{hc}{\lambda kT})} \tag{1.18}$$

This assumption is especially useful because the equation can be rearranged into a linear representation:

$$\ln[n_p(\lambda, T) \cdot \lambda^4] = \ln A - \frac{1}{T} \frac{hc}{k\lambda} \tag{1.19}$$

When the natural logarithm of the number of photons times the wavelength to the power of four is plotted against $hc/k\lambda$, the temperature is given by the inverse of the

slope of a linear regression. In spectral pyrometry with typical wavelengths of 200 to 1100 nm, the approximation is valid for a temperature up to several 1000 K. Most physical transitions or chemical reactions occur in this temperature range. Therefore, the Wien approximation is often applied in spectral pyrometry.

Transition region In the Transition region, for $hc/\lambda kT \approx 1$, no simplification of equation 1.17 is possible and an exponential fit needs to be conducted. This is the case for wavelengths in the visible region of the spectrum with temperatures in the range of 10.000 to 100.000 K.

Rayleigh-Jeans region In the Rayleigh-Jeans region, long wavelengths and high temperatures, i.e. for $hc/\lambda kT \ll 1$, the denominator can be approximated in the following way:

$$\exp \frac{hc}{\lambda kT} \approx \frac{hc}{\lambda kT} + 1 \tag{1.20}$$

Thus, equation 1.17 can be simplified to:

$$n_p(\lambda, T) = \frac{A}{\lambda^3} \frac{kT}{hc} \tag{1.21}$$

In this case, the emission spectrum depends only weakly on temperature in contrast to the Wien region. Equation 1.21 shows a linear relationship, while for the Wien region an exponential dependence was valid. The application of spectral pyrometry is therefore limited. However, if the emissivity is known, pyrometry can in principle be applied.

Example of spectral pyrometry. There are many examples in literature for the application of spectral pyrometry in science [5]. A good example is the temperature determination of the solid state chemical reaction of titanium and copper(II) oxide [5, 41].

$$\mathbf{Ti} \quad + \quad \mathbf{2} \quad \mathbf{CuO} \quad \rightarrow \quad \mathbf{TiO_2} \quad + \quad \mathbf{2} \quad \mathbf{Cu} \tag{1.22}$$

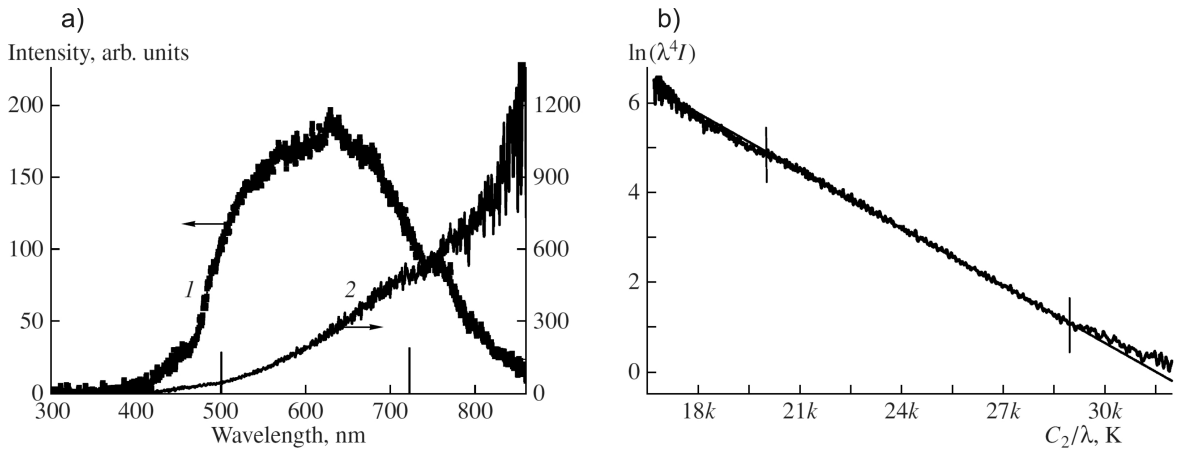

Figure 1.22: Emission spectrum for chemical reaction of titanium and copper(II) oxide powder mixture. (a) shows the spectrum as measured (1) and relative intensity (2), (b) the linear analysis according to the Wien approximation (equation 1.19). The constant C_2 is given by hc/k [5].

High temperatures are reached due to the exothermic nature of the reaction. The recorded emission in the visible range is shown in figure 1.22 (a). The Wien approximation is valid in this case. Therefore, the data is plotted according to equation 1.19 (figure 1.22 (b)). A linear fit results in a temperature of 2336 $\pm$ 3 K [5]. The quality of the linear fit reveals the thermal nature of the recorded emission and the low dependence of the emissivity on the wavelength. Although it is possible that the dependence of the emissivity is hidden in a plot according to equation 1.19, in most cases the applied grey body model can be confirmed this way.

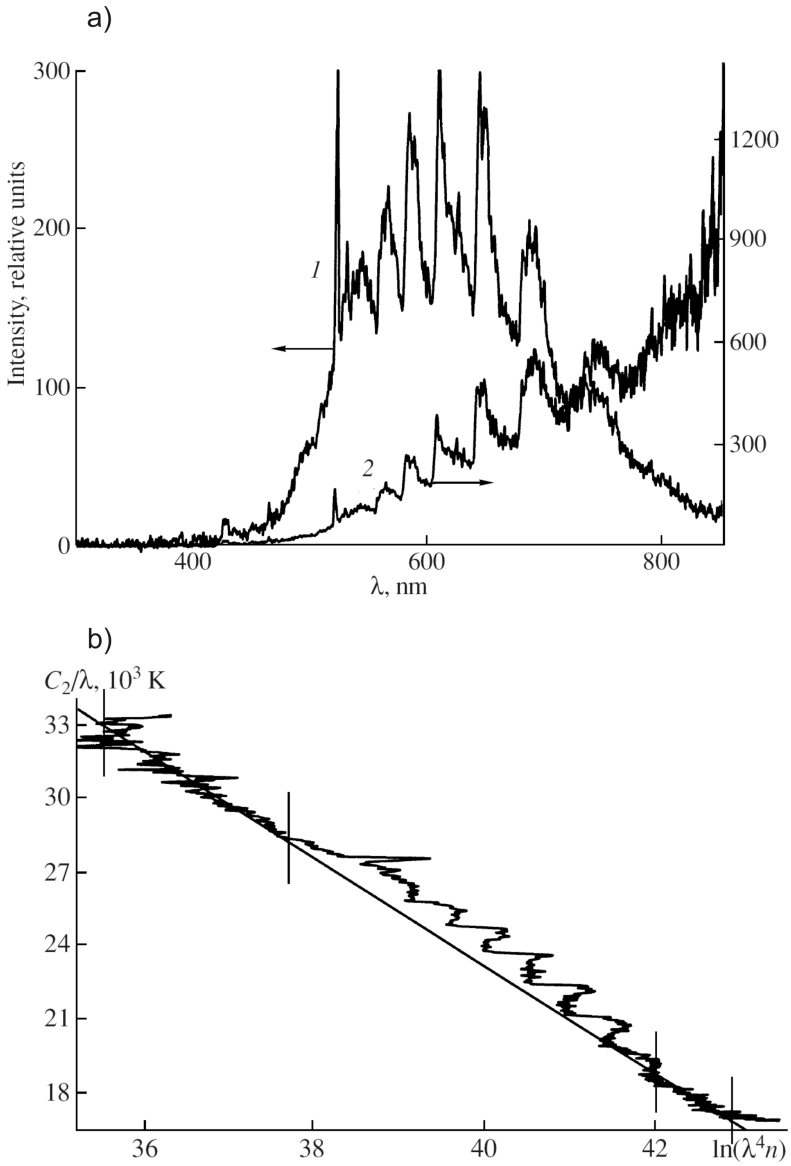

Figure 1.23: Emission spectrum of microwave discharge for chromium(VI) oxid powder. (a) shows the spectrum as measured (1) and relative intensity (2), (b) the linear analysis according to the Wien approximation (equation 1.19). The constant C_2 is given by hc/k. The exchange of x and y axis for the linear representation in respect to the plot in figure 1.22 does not influence the result (according to [45]).

In general, if no line fit can be found for the emission data, the dependence of the emissivity on wavelength is significant. Alternatively, there are contributions of non-thermal nature overlapping with the emission spectrum. In these cases, a temperature can only be fitted, if the dependence of the emissivity is known or can be estimated respectively if the non-thermal parts of the spectrum can be excluded. An example for the latter was described by Batanov et al. on the microwave discharge glow at the surface of chromium trioxide [45]. The spectral line of chromium and a number of molecular bands can be excluded and the thermal parts of the spectrum can be identified for fitting (figure 1.23).

Kirchhoff's law of thermal radiation. If necessary, a determination of the emissivity is possible via Kirchhoff's law. According to it, the spectral emissivity is equal to the spectral absorptivity in thermal equilibrium. The relationship is based on energy conservation. If a black body is in thermal equilibrium with another black body, it absorbs and emits equal amounts of energy at all wavelengths. Hence, there is no net transfer of energy. If real matter with an emissivity of arbitrary spectral dependence is taking the place of one of the black bodies, thermal equilibrium implies also zero net heat transfer. The reduced emission must be compensated by reduced absorption at equal wavelength in order to satisfy the equilibrium condition. Hence, the spectral emissivity $\epsilon_\lambda(T)$ is equal to the spectral absorptivity $\alpha_\lambda(T)$ for a given temperature:

$$\epsilon_\lambda(T) = \alpha_\lambda(T) \tag{1.23}$$

As a consequence, the emissivity is in principle experimentally accessible if the absorption can be measured. However, this excludes completely transparent and opaque materials. Furthermore, the temperature dependence of the emissivity may not be neglected, i.e. a temperature dependent absorption measurement is required. Spectral pyrometry is typically applied for temperatures higher than 800 K. Absorption measurement at elevated temperature in this range are not trivial. Although there are examples in literature. This method was applied for silicate glasses at temperatures up

to 1200 K [46]. However, other experimental techniques are usually preferred for the determination of the emissivity. The direct comparison of the spectrum of the real matter and a black body heated simultaneously was for example described by Rozenbaum et al. [47]. Alternatively, the temperature was simultaneously measured by thermocouples attached to the sample while the emission spectrum was recorded [48].

Another important consequence arises from Kirchhoff's law for transparent substances. Ideal crystals should for example not show any emission for wavelengths with an energy falling in the band gap [5]. Experiments confirm however, that this is not the case, for example for potassium or caesium bromide [43]. The phenomenon is not fully understood. A strong dependence of the emissivity with temperature could be observed for several materials [5]. The presence of impurities or defects induced by heating are possible explanations for this behavior [5].

Inhomogeneous temperature distributions in spectral pyrometry. Most object are not homogeneously heated. Especially when it comes to high temperatures, domains of higher and lower temperature are often formed. The spectral emission recorded with a detector in spectral pyrometry consists of contributions of both. Figure 1.24 shows a numerically simulated spectrum of a surface with Gaussian temperature distribution. The representation is analogous to equation 1.19, but instead of the number of photons the intensity is given by the radiant flux (compare chapter 1.2.3). Hence the wavelength to the power of five results at the y-axis.

The numerical simulated curve deviates from the linear dependence of homogeneous emitter. A fit through the entire wavelength range results in a temperature of 2616 K, as compared to the peak temperature of the simulated Gaussian distribution of 3000 K. If only the long wavelength part is fitted, 2264 K is found, whereas 2810 K is found for the short wavelength part.

In general, different temperature distribution models, stepwise or triangular, yield temperatures rather close to the maximum, comparable to the shown example of a Gaussian distribution [45]. If only parts of the spectrum can be used in order to obtain

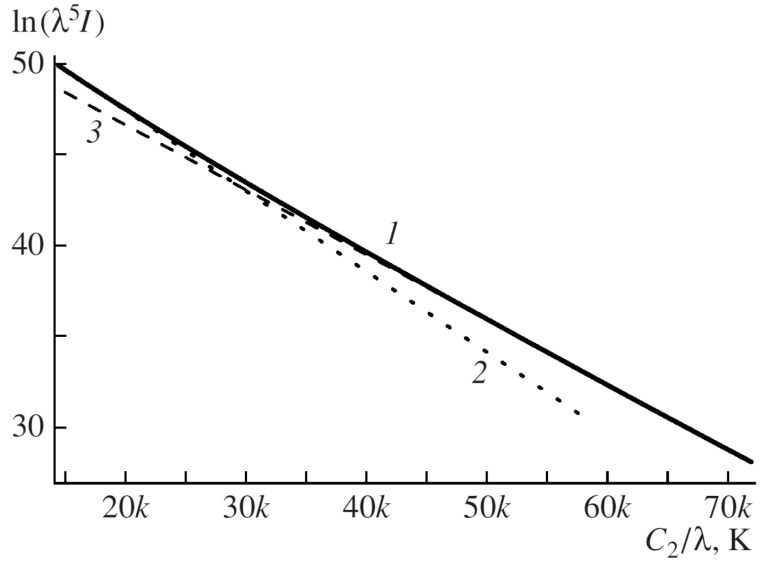

Figure 1.24: Numerically simulated emission spectrum for Gaussian temperature distribution with T_{max} = 3000 K in the linear plot according to the Wien approximation (equation 1.19) with the radiant flux instead of the number of photons. Numerical simulation (1), linear fit for long wavelength (2) resulting in 2264 K and linear fit for short wavelengths (3) resulting in 2810 K. A fit for the entire wavelength range results 2616 K (not shown). The constant C_2 is given by hc/k [5].

temperatures, higher temperatures closer to the maximum are deduced by the short wavelength regime while the opposite is true for the long wavelength regime. For unknown temperature distributions and a restricted wavelength regime this is an important conclusion.

Temperature measurement by pump-probe experiments

If it comes to laser heating, an important category of temperature measurements are based on pump-probe experiments. In principle, two laser pulses are used in this technique, a pump pulse which provides the energy for laser heating and a probe pulse which allows temperature determination. The temperature dependent parameter for the probe

beam can be diverse. In one example, the absorption of a dye molecule at constant wavelength is linked to temperature [2, 49–51]. I.e. the dye is used as a molecular thermometer. In another example, the temperature dependence of a Raman transition in the probe molecule is used, so called "time-resolved coherent Raman spectroscopy", CARS [1]. Pump-probe techniques are favorable for very fast time scales. A time resolution in the order of 1 fs is accessible.

Pump-probe experiments based on a molecular thermometer. An example for the application of a molecular thermometer, is the laser heating of poly(methyl methacrylate) (PMMA) by a Q-switched Nd:YAG laser with a wavelength of 1064 nm [2, 49–51]. The molecule in use is the dye "IR-165", with the chemical structure shown in figure 1.25. It is an organic NIR dye with an absorption maximum around 1100 nm (figure 1.26 (a)). The wavelength used to determine the temperature is however not at the maximum, but with 633 nm of a Helium-Neon probe laser at smaller wavelengths. The temperature dependence at this wavelength is shown in figure 1.26 (b). For calibration, the absorption was measured at slow time scales with a heating cell included in a standard spectrometer. It increases linearly and can therefore be extrapolated to higher temperatures for the pump-probe experiment.

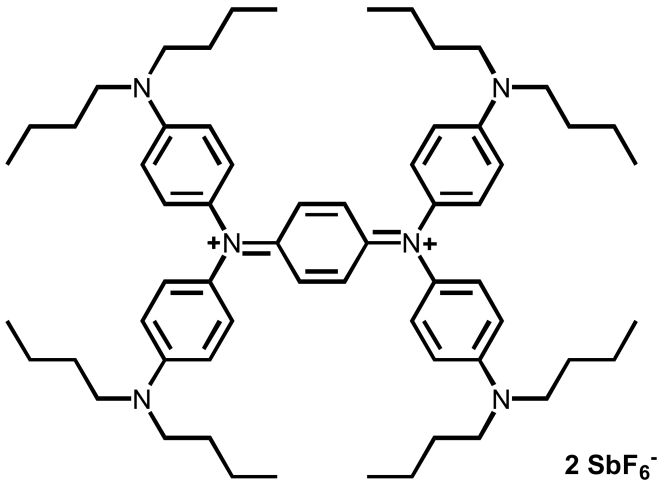

Figure 1.25: Chemical structure of molecular heater dye "IR-165" (according to [49]).

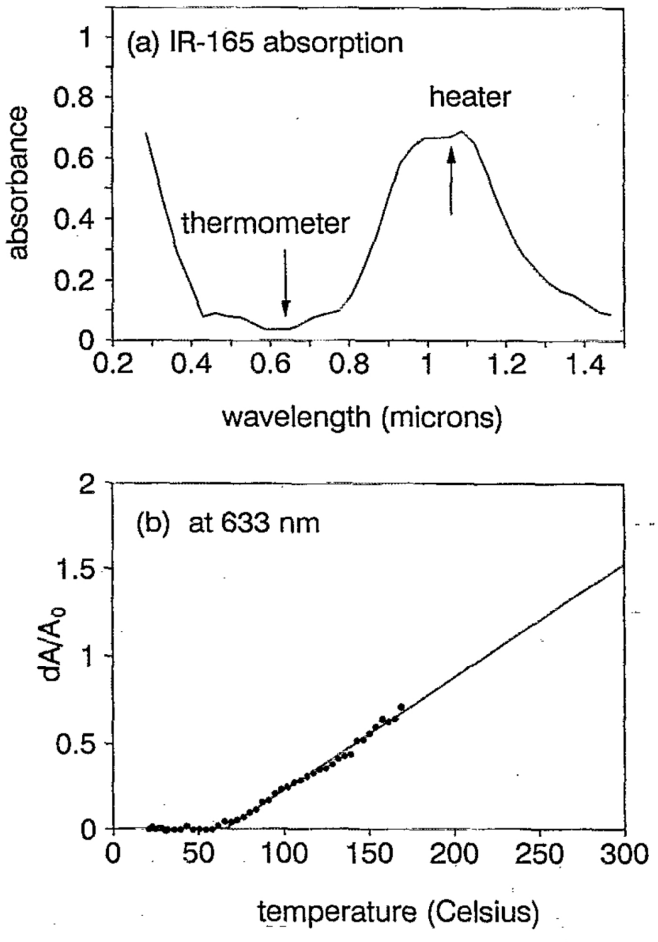

Figure 1.26: Absorption spectrum of molecular heater respectively thermometer dye (a) and temperature dependence of absorption strength at 633 nm (b) [2].

The NIR dye in this study does not only work as a thermometer, but simultaneously as a heater. The energy of the 1064 nm pump pulse is absorbed from the dye molecule and converted via internal conversion and vibrational cooling [50]. The surrounding polymer matrix takes up the energy via a mechanism called "multiphonon up-pumping" [50], i.e. the multiple absorption of phonons by the polymer from the dye. In this way the laser energy is converted into thermal energy on the order of a few ps.

Ablation and the ablation threshold was studied applying this temperature measurement method by Lee et al. [2]. Figure 1.27 (I) shows the peak average temperature during 100 ns laser pulses of different energies and the corresponding calculated maxi-

mum surface temperature. Ablation was found for peak average temperatures of about 330°C. The maximum surface temperature at this point was already about 600°C. Furthermore, the temperature levels off at a maximum temperature (T_{lim}). About 390°C respectively about 710°C at the surface were determined in the experiment.

If the time dependent temperature evolution is regarded (figure 1.27 (II)), a drawback of the method is obvious. The sudden rise in absorption of the curves at higher pulse energies are due to ablation of the polymer, not due to an increase in temperature. Ablation products additionally absorb light of the probe beam. A temperature measurement after the ablation onset is therefore not possible. The time dependence of the first 200 to 300 ns can however be used to extrapolate the temperature, and allow the calculation of the peak average and the maximum surface temperature (figure 1.27 (I)) even if ablation occurs.

It is important to notice, that the measured temperatures exceed the calibration window significantly. The authors of the studies took great care to ensure, that the measured temperatures are reasonable in terms of thermodynamics by comparing the calculated heat capacity based on the pump-probe experiments with the one measured by standard differential scanning calorimetry [2, 49–51]. However, generalization of this approach is questionable.

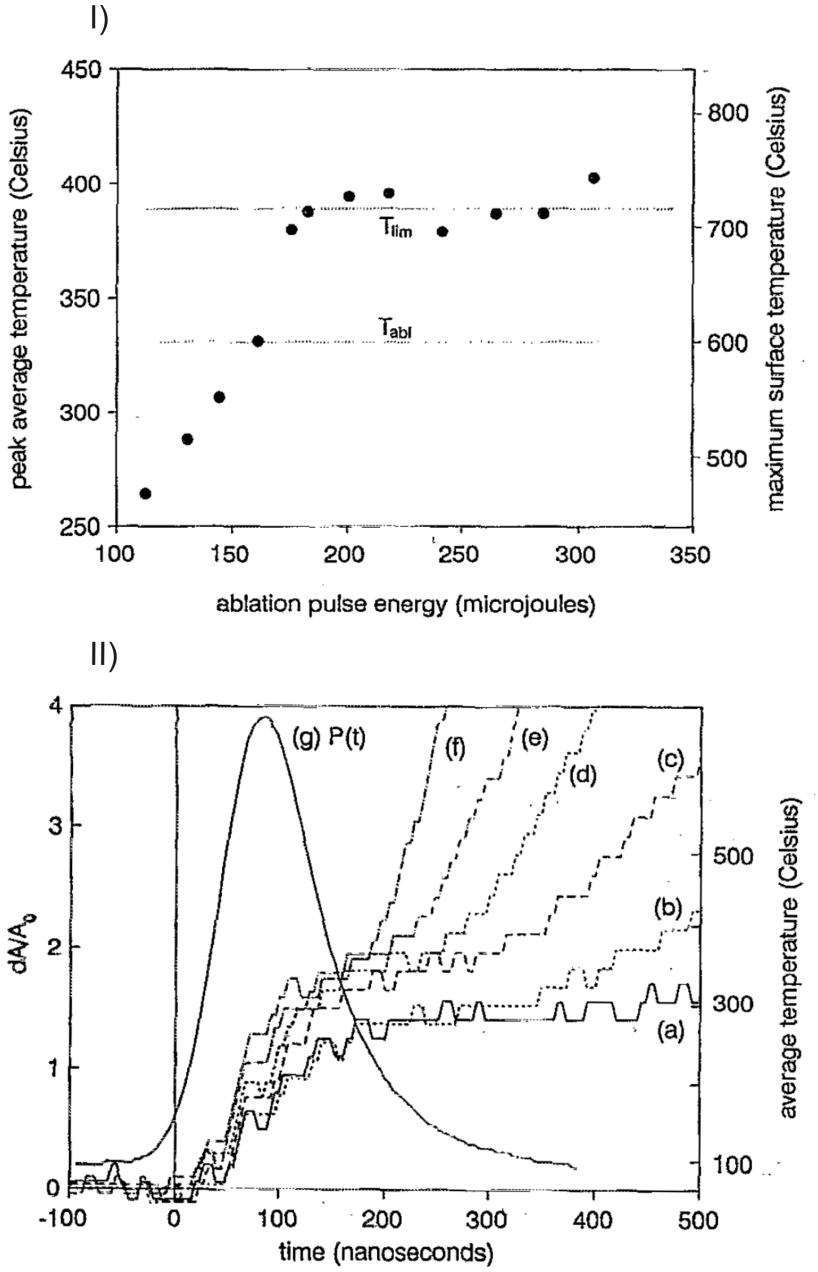

Figure 1.27: Result of temperature determination in a pump-probe experiment with a molecular thermometer. Measured peak average temperature and calculated maximum surface temperature (I). The time dependent absorption and average temperature for different pulse energies (II) in µJ: 131 (a), 161 (b), 184 (c), 242 (d), 307 (e) and 603 (f). The solid line (g) represents the envelope of the pump pulse (according to [2]).

Pump-probe experiments based on time-resolved coherent Raman spectroscopy. Time-resolved coherent Raman spectroscopy (CARS) was also applied on the example of laser heated PMMA [1]. As temperature sensitive parameter, the frequency shift of a vibrational band at ≈ 808 cm^{-1} of the PMMA was chosen. However, the frequency shifts not only with temperature, but also with pressure. Figure 1.28 shows the result of static experiments, for different pressures at constant temperature and for different temperatures at constant pressure. This data is used for calibration of the frequency shift in pump-probe experiments.

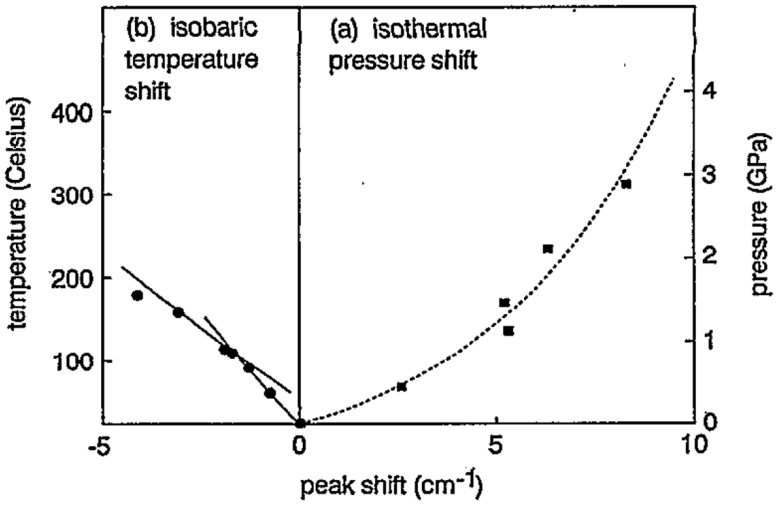

Figure 1.28: Frequency shift with pressure (T = constant) (a) and temperature (p = constant) (b) at ≈ 808 cm^{-1} of PMMA in static experiments [1].

The static experiments reveal, that a frequency shift occurs for changes in pressure and temperature, in different directions respectively. PMMA expands when heated [52]. Thus, for a laser heating experiment of the polymer, both, pressure and temperature change simultaneously. In order to separate one from the other, the time scales of the changes need to be accounted and compared to the laser pulse duration.

The experiment was conducted with a setup described by Hare et al. [53]. It consists of a Q-switched and additionally mode-locked Nd:YAG laser with a pulse duration of 150 ps. If compared to the inertial confinement time, $t_h = 1.3$ ns [1], introduced in

chapter 1.2.2 (equation 1.5), the condition for inertial confinement is met. The relaxation time of the pressure is consequently in the order of 1 to 10 ns. In contrast, thermal relaxation times for PMMA lie in the order of 10 µs [1]. Thus, pressure and temperature can be discriminated by a time dependent frequency shift measurement of the chosen Raman band. The principle, how this can be achieved is shown in figure 1.29. A first fast change in pressure and temperature is followed by a fast drop in pressure due to an isentropic expansion and a slow cooling. Therefore, the frequency shift after pressure relaxation can be used to determine the temperature. Then a shock wave model can be applied to obtain temperature and pressure at earlier times.

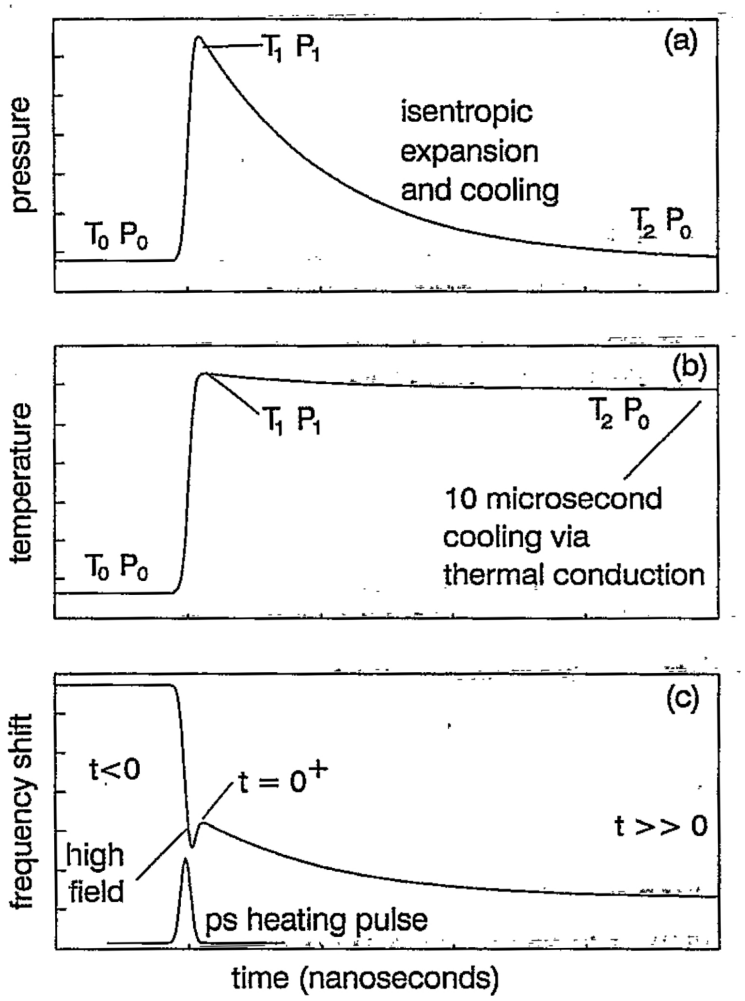

Figure 1.29: Scheme of behavior of pressure (a), temperature (b) and frequency shift (c) for laser heated PMMA with pulse durations of 150 ps [1].

Analogous to the studies presented in chapter 1.2.5, the NIR dye "NIR-165" was included in the polymer matrix. In this way sufficient laser energy absorption was guaranteed. The result of the CARS measurement for a 150 ps pump pulse is shown in figure 1.30, again on the example of PMMA ablation. The pressure and temperature was obtained for different laser pulse energies. A first slow increase of temperature and pressure until about 220°C and 0.2 GPa was followed by a faster increase up to about 520°C and 2.5 GPa for high laser pulse energies. The authors addressed the change in slope to the onset of ablation. The steeper increase in pressure was associated to the formation of gaseous and volatile ablation products. Therefore, they used the terms "thermophysical pressure" for the slow increase at pulse energies below and "thermochemical pressure" for the fast increase above the ablation threshold. The ablation threshold temperature was determined to be about 280°C at 0.5 GPa. [1]

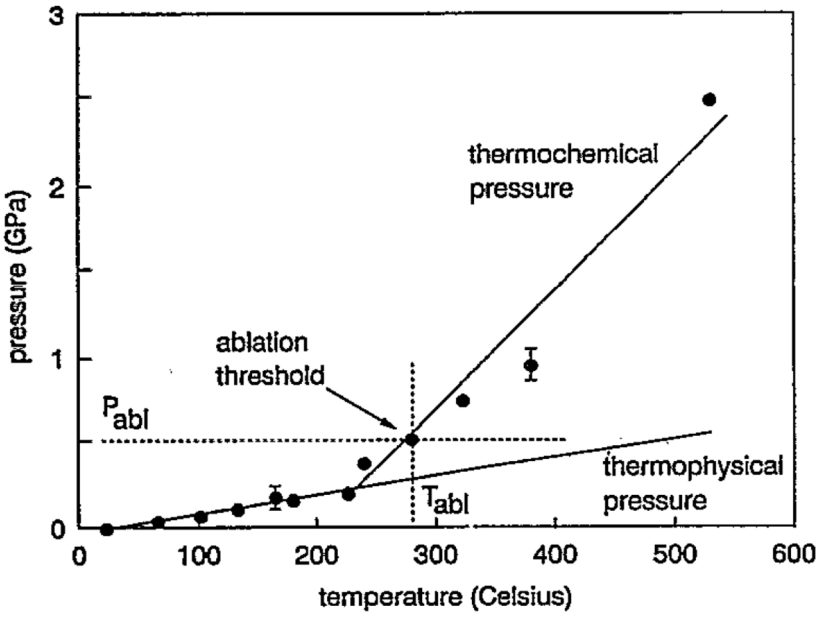

Figure 1.30: Peak pressure vs. peak temperature of CARS for laser heated PMMA for laser pulse durations of 150 ps and various pulse energies [1].

A critical point for the method is, that just like for the molecular thermometer, the temperatures measured in the experiment exceed the calibration range. Especially when

material is ablated, temperatures above 500°C are obtained, while the highest point of the calibration measurement is below 200°C. Analogous to the previous study using a molecular thermometer, a comparison of the calculated heat capacity based on the results of the pump-probe experiment with differential scanning calorimetry values could however verify the plausibility of the results.

Both pump-probe experiments presented here analyze the photothermal ablation behavior of doped PMMA. The pump-pulse duration is however different by three orders of magnitude. As already discussed in chapter 1.2.2 different ablation mechanism are dominant, a stress-assisted in the case of the molecular thermometer study and a shock-assisted for the study based on CARS. The difference in ablation threshold temperature is due to this difference in mechanism [1].

1.2.6 Rylene dyes

Rylene dyes represent a versatile group of dyes. They are built up of naphthalene units which are linked at the peri position. Therefore, these dyes are sometimes also called oligo- or poly(peri-naphthalene) (figure 1.31). Especially, higher homologues of rylene dyes are insoluble pigments. However, via appropriate functionalization they can be made water soluble [54] or soluble in organic solvents [55].

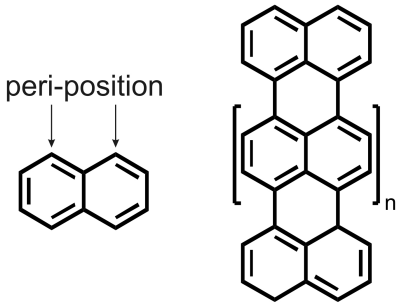

Figure 1.31: Chemical structure of naphthalene and poly(peri-naphthalene).

A lot of applications could already be realized based on rylene dyes in the field of optoelectronics, photovoltaics, thermographic processes, light-emitting diodes, NIR absorbing systems and single molecule spectroscopy [56]. High absorption coefficients in the combination with high chemical, thermal and photostability are the main reasons for the versatility of the dye family [56–58].

An advantage of rylene dyes is, that the optical properties, for example the absorption maximum, can be tailored via functionalization. Figure 1.32 shows how this can be done on the basis of the "push-pull family of perylenes" [56] by variation of electron donors or acceptors. Functionalization at the bay position with different electron donor substituents causes a hypsochromic shift (structure 8 in figure 1.32). Via choice of the appropriate donor the shift can be adjusted (structure 6 and 7). On the other hand, variations of the electron donors at the peri-position allows a bathochromic shift. Also the electron acceptor, the imide group may be exchanged, to obtain even higher wavelengths for the absorption maximum (structure 11 in figure 1.32).

A promising functionalization for perylenes is the introduction of phenoxy groups at

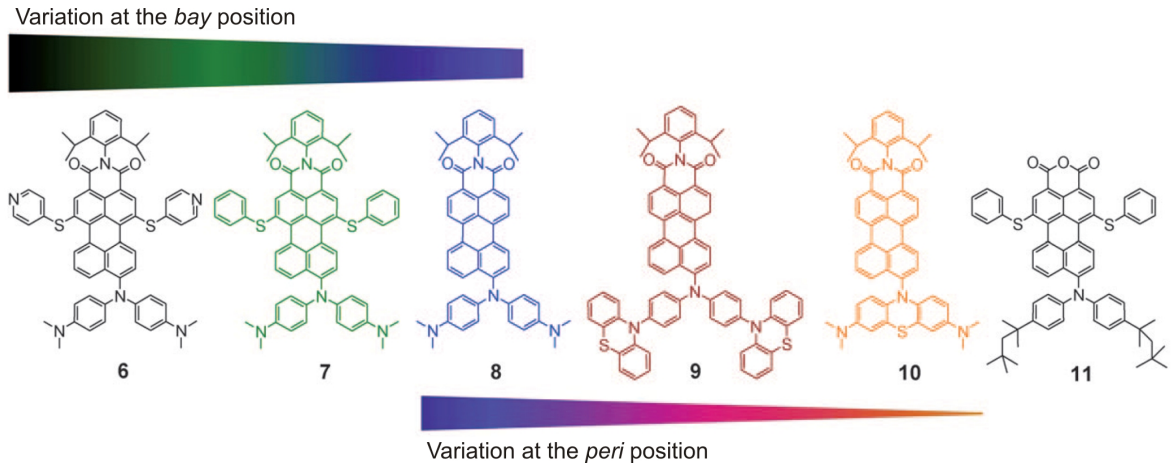

Figure 1.32: Chemical structure of various functionalized perylene dyes with absorption maximum shifted throughout the visible region (as indicated by their color and the color bar above respectively below the structures) [56].

the bay position. The example of perylene diimide and its tetraphenoxylated analogue illustrates this issue (figure 1.33). The tendency of aggregation via π-stacking is reduced, increasing the solubility [56]. Additionally, the absorption and emission spectrum is altered with the functionalization. The substituents are electron donors, leading to a bathochromic shift of the maxima. Furthermore, the tetraphenoxylated perylene diimide shows less vibronic fine structure, indicating the presence of more vibrational states with low energy difference. This can be attributed to the additional degrees of freedom gained by the phenoxy groups. Besides, a stronger transition from the ground state into the S_2 is observed and the functionalization increases the photostability [55, 56].

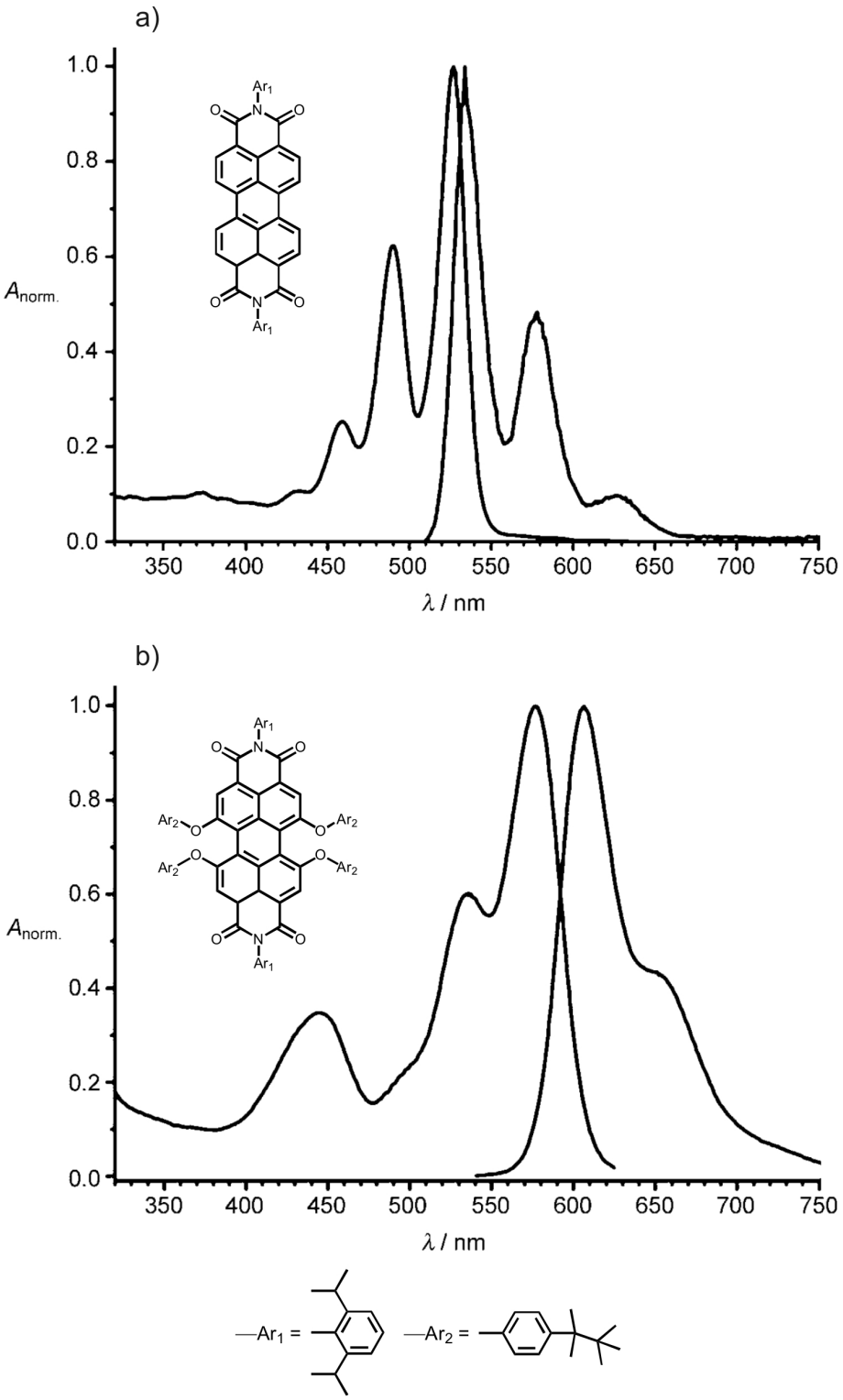

Figure 1.33: Absorption spectra and emission spectra of perylene diimide respectively tetraphenoxy functionalized perylene diimide (according to [56]).

Higher homologues of rylenes can also be solubilized via tetraphenoxy functionalization. The absorption maximum shifts with each additional naphthalene unit by about 100 nm to higher wavelengths (figure 1.34). Considering the simple quantum mechanical model of the electron in a box, a lowering of the energy levels and therefore a bathochromic shift of the absorption maximum is consistent with the enlargement of the conjugated π-system. Additionally, the absorption coefficient increases with number of naphthalene units. Another difference between the homologues is the tendency to fluorescence. The perylene (PDI) and terylene diimide (TDI) exhibits quantitative respectively almost quantitative fluorescence. In contrast, the quaterrylene (QDI) and higher homologues show almost no fluorescence [59]. The energy is instead converted to thermal energy by internal conversion and vibrational relaxation [58].

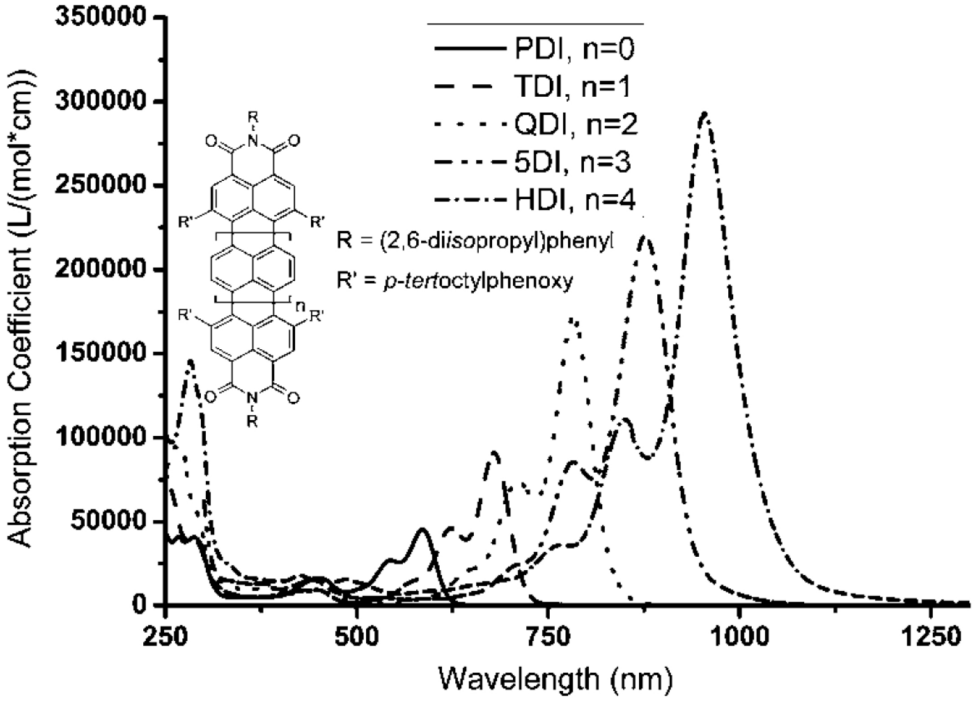

Figure 1.34: UV-Vis absorption spectra of tetraphenoxy functionalized perylene diimide and its higher homologues [59].

The higher homologues can therefore not be used in applications with obligatory good fluorescence properties. However, other application, for example QDI in heat blocking

layers, make use of the property of low fluorescence but non-radiative conversion [59]. A thin polymer layer including QDI is placed between two glass plates. The QDI absorbs the NIR part of the spectrum. The visible part of the spectrum passes by mostly, i.e. the transparency of the glass remains. The absorbed energy is converted into heat and transfered to the glass plates. The outside glass plate is cooled more efficiently through convective heat transfer, especially if an air flow is present. Therefore, the inside is effectively blocked from heat due to sun light. Daily life application like car windscreens or architectural glasses can be realized in this way.

In an analogous way, the heating effect of the dye can also be used for laser welding of plastics [59]. The laser can in this respect heat very selectively, and for example join two dye-sensitized polymer plates or foils together at one point. The printing plate technology based on laser induced film formation applies the same effect. Instead of macroscopic plates or foils, polymer micro- or nanoparticle are fused together via heating. The formed polymer film lay the foundation for the necessary hydrophobic-hydrophilic contrast on press.

1.2.7 Confocal white light profilometry

A versatile method for surface analysis, well suited for the analysis of the surface morphology, is confocal white light profilometry. It is based on the principle of confocal microscopy, illustrated in figure 1.35 (a). In confocal microscopy, not the whole sample is illuminated, but only a small area. In order to achieve this, a pinhole is applied in front of the light source (illumination pinhole) before the light is focused on the sample. Light from outside the focal volume is blocked in the detection pathway through a pinhole (receiver pinhole) before it reaches the detector (indicated by the dotted blue line). As a consequence, an image is not directly acquired but, results from a scan of the sample. The focal volume is moved across the sample respectively the sample is moved with a translation stage. The intensity for each point is recorded and evaluated later on to yield an image. 3D images can be acquired in this way. A disadvantage of confocal microscopy is, that it is relatively slow. However, the setup can be slightly modified to achieve faster image acquisition. Figure 1.35 (b) represents the typical setup for a white light confocal profilometer. With such a device live 3D surface images can be recorded.

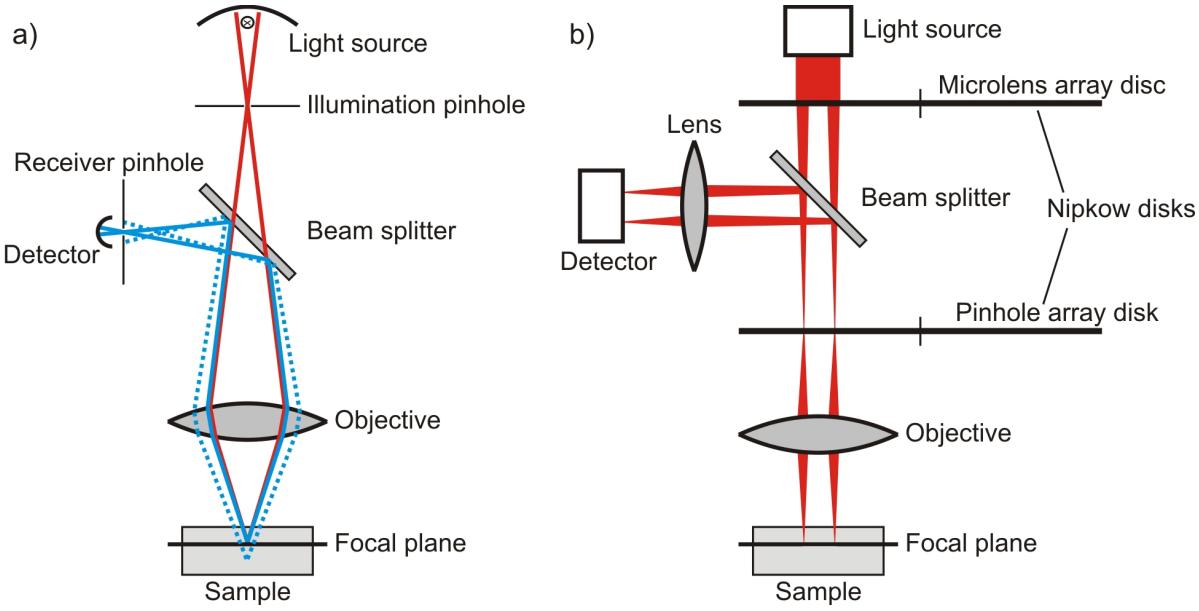

Figure 1.35: Scheme of principle setup in confocal microscopy (a) and in white light confocal profilometry (b).

The key components of the setup in figure 1.35 (b) are the Nipkow discs, equipped with microlenses respectively pinholes. An example of a Nipkow disc, illustrating the working principle, is shown in figure 1.36. Holes are arranged spirally in a circular disc. The illuminated area consists of a small sector of the disc. In this way, the illuminated area respectively the image is divided into lines. I.e. a two dimensional image is split up and discriminated into a line, "a one dimensional image". The same principle was applied in the first television setup. The image was projected on a Nipkow disc, just like the illumination area in figure 1.36. A phototube was set behind the disc to record the light intensity in time, the "one dimensional image". On the other hand, for projecting the image, the setup was reversed. The electrical signal from the phototube was adapted to a light source and projected on a Nipkow disc to generate the image on a screen located behind the disc. If the same recording procedure was repeated for multiple images, and then replayed one after the other on the projecting setup, a movie could be created.

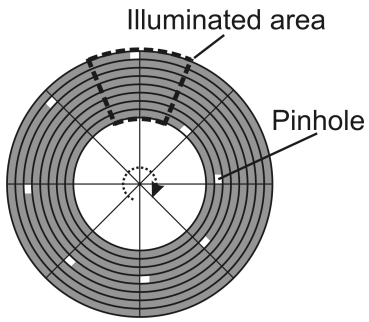

Figure 1.36: Scheme of a Nipkow disc.

In a similar way, the acquired light intensity in a confocal white light profilometer is split up into lines and reconstructed to form a three dimensional image.

Figure 1.37 shows an example of a surface profile acquired by white light profilometry, a star on the 1 cent coin. Small scratches or deformation can be seen, especially in the height image or the 3D surface profile with higher magnification. Furthermore, the surface roughness in the area surrounding the structure is well visible on the lower left side in the 3D surface profile. The height of the star can be determined to be 31.5 µm, or the scratch on the high resolution zoom in with a depth about 1.3 µm and a width

of about 20 µm.

The method is not restricted to hard surfaces and, in contrast to electron microscopy, there is no need for vacuum. It works in ambient conditions. In principle, any interface can be analyzed, as long as an optical contrast between the phases is present. Even buried structures can be visualized, if the top layer is transparent. An example is the topography of a substrate underneath a transparent polymer layer. This makes confocal white light profilometry a versatile tool in science, but also in industry for product development or quality management.

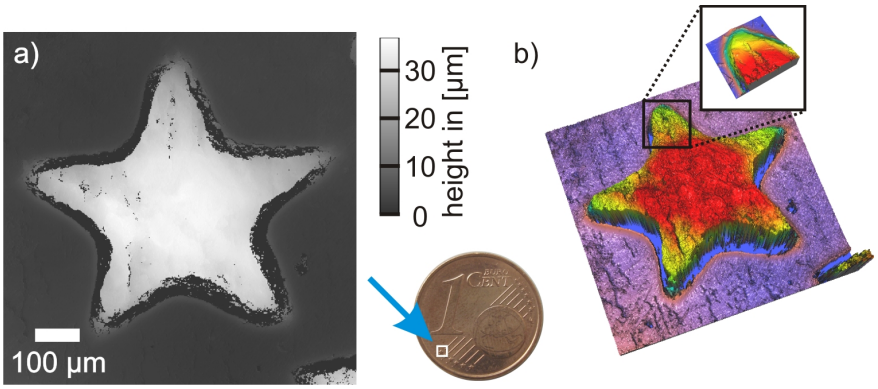

Figure 1.37: Confocal white light profile of star on 1 cent coin. Height image (a) and 3D surface profile (b).

2 Materials and methods

2.1 Experimental details

2.1.1 Temperature measurement setup

The experimental setup for recording the thermal emission was already described in [60, 61] and in parts also in [62]. It consisted of a laser, a sample stage, some optics including bandpass filters and a camera (figure 2.1).

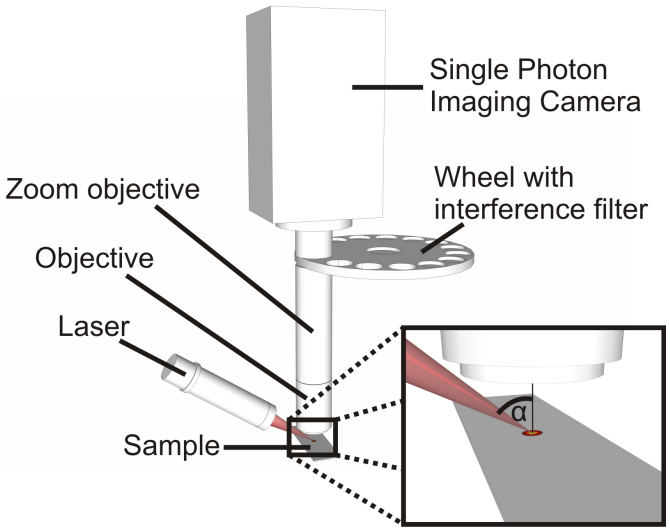

Figure 2.1: Scheme of the experimental setup.

A 810 nm diode laser (Schaefter + Kirchhoff GmbH) with up to 70 mW was focused on the sample surface, which allows power densities up to about 100 kW/cm^2. The intensity profile across the beam was Gaussian. For the experiments, angles of 67° and 56° were used (compare figure 2.1). The energy profile was therefore distorted along one

axis. Out of geometrical reasons, the angle of 56° was the minimum angle possible. The two diameters of the elliptical illumination spot were determined to be 6.9 × 17.7 µm^2 for 67° and 6.9 × 12.3 µm^2 for 56° ($(1/e^2)$, measured by Beam Scan model 1180 optical profiler, Photon Inc.).

Pulses were created by switching the laser "on" and "off". The control of pulse length and laser power was achieved with two electrical signals. A digital signal, to turn the laser "on" or "off" and an analogue signal to adjust the laser power via a potential. The relationship between potential and laser pulse energy (figure 2.2) was measured by a laser power meter (OP-2 Vis, Coherent GmbH). In the range between 0.3 V and 2.5 V a linear relationship was found. Pulse energies of 0.019 to 1.04 µJ were obtained for a typically applied 15 µs laser pulse (figure 2.2). This equals an average fluence of 0.028 to 1.56 J/cm^2 over the area defined by the $1/e^2$ diameters for an angle of incidence of 56°. Following literature, the fluence is used in this work as an experimental parameter to define the laser power. However, the term "fluence" stands for the average fluence over the area defined by the $1/e^2$ beam diameters. One has to keep in mind, that the Gaussian intensity distribution locally implies much higher fluences.

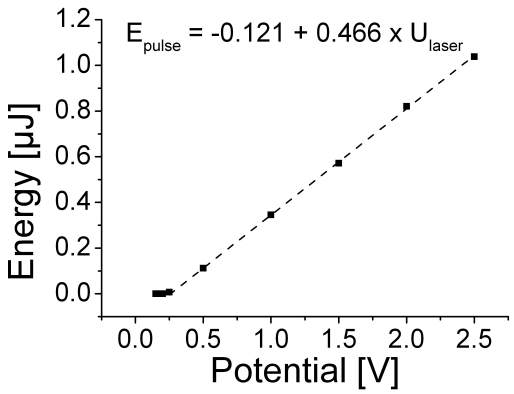

Figure 2.2: Control of the laser power by an applied potential. Pulse energy vs potential for 15 µs laser pulses.

The digital pulse, which was switching the laser "on" and "off" was synchronized with the camera. The scheme in figure 2.3 illustrates the definitions of the "delay time" and

the "integration time". The delay time and the laser pulse were started simultaneously. The start of the integration time, in which data is acquired, is in turn given by the delay time. Synchronization with a time resolution on the 1 ns time scale was achieved. Furthermore, time dependent measurements were obtained by variation of the delay time.

It is important to notice that the "laser pulse duration" is the time set for the digital pulse to "on". The digital pulse describes a rectangular shape on the 1 µs time scale, whereas the corresponding laser intensity time profiles do not (figure 2.4). The profiles show a shark tail type characteristic and they change with laser pulse energy applied. For simplification purposes, only the laser pulse duration is given for each experiment.

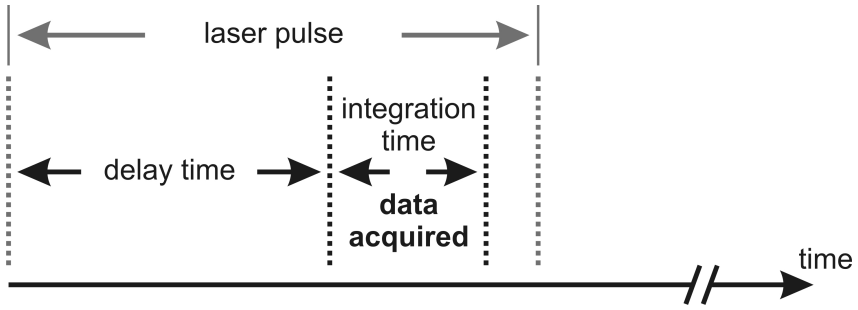

Figure 2.3: Scheme of switching and synchronization of the laser and camera in time.

The detection of the thermal emission was done with a "Single Photon Imaging Camera" (Theta System Elektronik,GmbH). It consists of a firewire CCD-camera system including a multichannel plate as amplifying unit and an external high frequency pulse generator. The pulse generator was controlled, just like the laser, with a digital pulse, which was set to "on" for the time of data acquisition (figure 2.3) as discussed above. The high frequency pulse generator allows integration times of 1 µs up to about 4 ms. For temperature measurements, the integration was typically set to 1 µs, to assure maximum time resolution.

Light was detected through a 100x objective with long working distance (ULWD 100x, Motic Incorporation Limited) and a zoom objective (Zoom 70XL, Qioptiq Imaging Solution). The latter was modified to allow the incorporation of a bandpass filter wheel

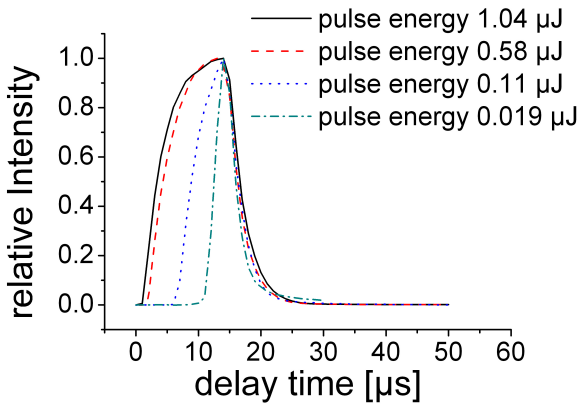

Figure 2.4: Time profile of 15 µs laser pulses for different pulse energies. Measured with the camera included in the setup, with no filters (without bandpass and notch filter) in the beam path.

for spectral sensitivity of the light detection. Twelve bandpass filters (Andover Corporation) with center wavelengths of 500 to 760 nm and a bandwidth of about 10 nm (full width half maximum) were incorporated in the wheel (details see table 2.1). In addition, a notch filter (Single Notch Filter for 808 nm - E grade, Semrock Inc.) was included in the beam path to filter out traces of laser stray light.

A calibration of the detector system (camera, optics) was carried out. Therefore, a halogen lamp with a known spectrum (Cal CL2, Bentham Instruments Ltd.) driven by a stabilized voltage source (NTN 350-20, FuG Elektronik GmbH) was connected to the detector system and measurements were conducted. In this way, calibration factors were calculated for each bandpass filter (table 2.1).

The control of laser and camera, i.e. the digital pulses and the set potential, was conducted via a desktop PC with a multi functional PCI card (M-Series, PCI-6221 (37 Pin), National Instruments Corporation).

The sample was adapted to a sample holder which was mounted on three motor stages (Micos GmbH) in order to enable movement in three dimension. These stages, as well as the bandpass filter wheel, were controlled by the desktop PC via two motor controller cards (SMC-PCI, SM-Series, Micos GmbH). Automation and data acquisition

Center wavelength [nm]	FWHM [nm]	Calibration factor
500.693	10.456	2.113
542.414	9.530	1.631
571.875	9.193	1.737
602.924	10.101	1.087
622.912	10.505	0.951
642.918	10.941	1.065
662.170	9.545	1.184
682.555	10.131	1.074
700.648	9.207	1.152
722.728	9.908	1.143
741.805	10.137	1.179
761.888	10.503	1

Table 2.1: Bandpass filters included into the filter wheel with calibration factors at the wavelength interval for the detection system (center wavelength and FWHM according to the distributor LOT Oriel GmbH Darmstadt).

was implemented in Labview 8.5.1 programs (National Instruments Corporation).

The programming allows fully automatic data acquisition for a temperature measurement. For one laser pulse only the thermal radiation for one bandpass filter, i.e. one wavelength interval can be acquired. To obtain a spectrum of the thermal radiation, the laser pulse has to be repeated for each bandpass filter. Therefore, the sample was moved to a new position and the next bandpass filter was brought in the beam path. For statistical reasons, typically 150 images were taken for each bandpass filter and averaged later on. In this way, statistical errors in performance of the laser and the camera can be neglected. The method can only be applied if the sample surface is sufficiently homogeneous. However, a broadening of the temperature profiles has to be considered due to inhomogeneity and roughness of the sample surface.

For an easier alignment of the sample along the moving direction two tilt stages were

M_n [g/mol]	M_w [g/mol]	PDI
3900	4380	1.12
158000	167000	1.06
314000	337000	1.07

Table 2.2: Molecular weight distribution of polystyrene (GPC, PS-Standard).

included in addition to the three motor stages at the sample holder. Several adjustment experiments were carried out before the automated program was started. The z position of the sample is critical, because not only the laser has to be focused on the surface but also the camera objective. For adjustment, the thermal emission was regarded without a bandpass filter in the beam path and the optimal position in z and a 0° tilt in x and y direction was found in multiple iterative experiments.

2.1.2 Sample preparation

Polymers

Polystyrene was made by anionic polymerization with different molecular weight ranging from 3900 g/mol up to 314.000 g/mol (table 2.2). Films of various thicknesses were prepared by blade coating from tetrahydrofuran solutions of concentrations ranging from 10 to 50 mg/ml. Coating was proceeded with the following parameters: a slit h of 500 µm, a speed u of 1.7 mm/s, a blade with thickness d of 2 mm and an angle φ of 45°(figure 2.5). The NIR-dyes (see below) were included into the solution to guarantee good dispersion of the dye in the polymer film. Various concentrations of the dyes were used. Films were casted on glass substrates (standard object slides). The polymer films were used without further treatment. By comparison of laser heating experiments for an annealed film (80°C for 24 hours at 20 mbar) with non-treated samples it was verified, that residual solvent had no influence on the result.

Besides polystyrene, a few other polymers were used to test the influence of the polymer on the laser heating experiment. The chemical structures are shown in figure 2.6.

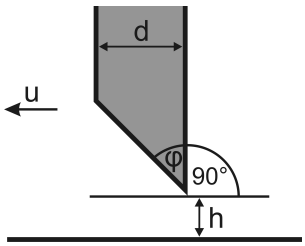

Figure 2.5: Geometry of blade coating setup (according to [63]).

Poly(α-methylstyrene) (2) (M_n = 76500 g/mol, M_w = 78600 g/mol, PDI = 1.03, GPC, PS-Standard, made by anionic polymerization) is known to be thermally less stable than polystyrene. Films were blade coated on glass slides from tetrahydrofuran solutions including 100 mg/ml of the polymer and 4.2 mg/ml of dye 1 (QDIBr, figure 2.7), corresponding to 4 % in relation to the polymer. The coating parameters were chosen analogous to the ones of polystyrene. The films were used without further treatment.

Furthermore a thermally more stable polymer, the polyimid (3) (M_n = 746 g/mol, M_w = 2350 g/mol, PDI = 3.15, GPC, PS-Standard) was compared to polystyrene. The polymer was synthesized by XXX XXX (MPI for Polymer Research, Mainz) according to the synthesis route of Hahm et al. [64]. Films of the polyimid could be obtained by spin coating a solution with the concentration of 4.2 mg/ml of the polymer in cylcopentanone on glass slides including about 2.3 mg/ml dye 1 (QDIBr), corresponding to 36 % in relation to the polymer. In order to enhance solvent evaporation, the substrate was preheated. The spinning speed was set to 500 rpm for 60 s with an acceleration of 500 rpm/s. Due to the low vapor pressure of the solvent, the films were kept in a vacuum chamber at low pressure for 24 hours after spin coating to remove residual solvent.

Additionally, a triazene polymer (4), a polymer which is often applied in laser induced forward transfer (LIFT, introduced in chapter 1.2.2) was used. The polymer was kindly provided by XXX XXX (Laboratory for Functional Polymers, EMPA, Dübendorf) and XXX XXX (Materials Group, Department of General Energy Research, Paul Scherrer Institute, Villingen). A 1:1 mixture of chlorobenzene and cyclohexanone was used as

solvent. Polymer films were spin coated on glass slides from solution including 4 % of the polymer and 0.4 % dye 1 (QDIBr), corresponding to 10 % in relation to the polymer. The coated process was conducted with a spinning speed of 1000 rpm for 60 s and an acceleration of 1000 rpm/s. Analogue to the polyimid film, residual solvent was removed by keeping the triazene polymer films in a vacuum chamber at low pressure for 24 hours.

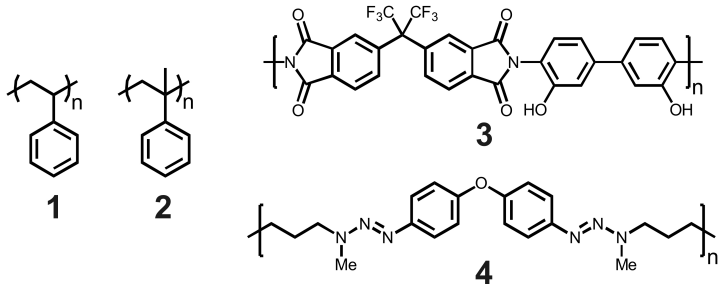

Figure 2.6: Chemical structures of polymers. (1) polystyrene, (2) poly(-α-methylstyrene), (3) polyimid and (4) triazene polymer.

Dyes

Most polymers are transparent at the NIR wavelength of the laser. Therefore a dopant, a dye, was added to the polymer solution which absorbs in the NIR wavelength region. A prominent group of dyes showing strong absorption in this region are quarterrylene dyes introduced in chapter 1.2.6. Three different functionalized quarterrylene dyes (figure 2.7) were used. They were synthesized by XXX XXX (MPI for Polymer Research, Mainz) according to literature [59, 65].

Heatable cantilever

As a reference system to the laser heated polymer films, a heatable atomic force cantilever (ThermaLever Probes AN2-200, Anasys Instruments Corp.) with a length of 200 µm, a thickness of 2 µm and a height of 3-6 µm was measured with the detecting part of the setup. These cantilever can be heated by an external voltage source (Ex 354D Dual Power Supply, Thurlby Thandra Instruments) in steady state.

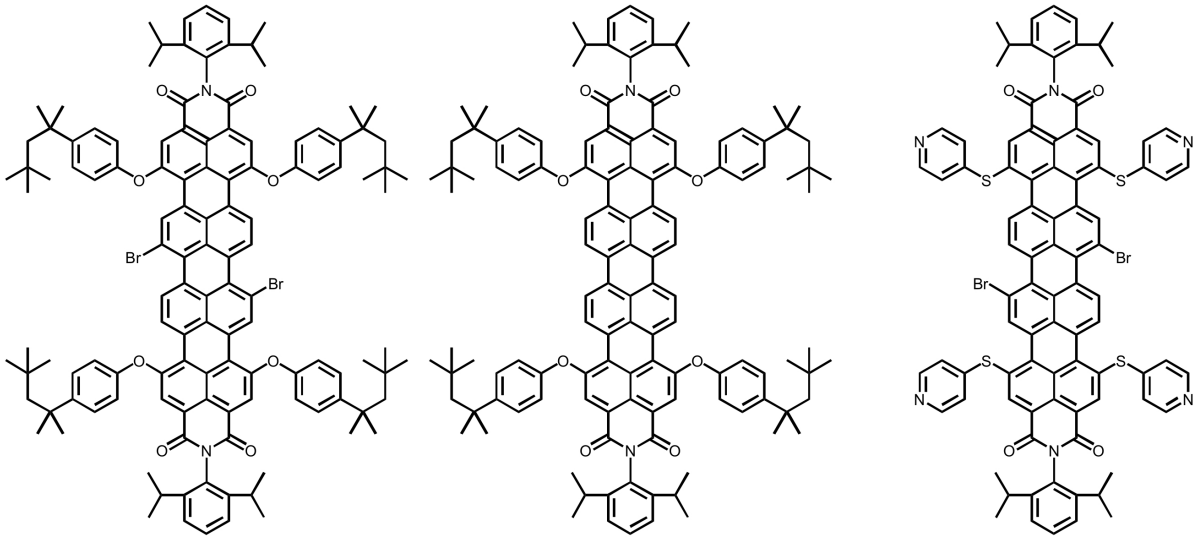

Figure 2.7: Chemical structures of different dyes.

2.1.3 Other experimental techniques

Topological studies of the polymer films were conducted using a white light confocal profilometer (µsurf, Nanofocus AG) equipped with an UMPLFL 100x objective. The film thickness was also determined with this technique. Scanning electronic microscopy images were taken with a Gemini 1530 (Zeiss/Leo). Thermogravimetric measurements of the polymers were performed with a TGA 851 (Mettler Toledo GmbH), differential scanning calorimetry with a DSC 30 respectively a DSC 822 (Mettler Toledo GmbH). A standard absorption spectrometer (spectrometer Lambda 900, Perkin Elmer) was used for absorption measurements of the polymer films.

2.2 Simulation details

Finite element simulations were conducted for polystyrene films. The simulations were carried out using the finite element simulation software Comsol Multiphysics version 4.0a (www.comsol.de). The model geometry comprised the substrate layer, the polystyrene layer including the dye and an airbox (figure 2.8). The boundaries of the model were aligned with the half axes of the elliptical laser spot and the computational domain was reduced by exploiting the symmetry of the problem. Conductive heat transfer was taken into account in all parts of the model cell. Additionally, convective heat transfer was considered in the airbox. Radiative heat transfer was neglected due to its limited relevance in the applied temperature regime (i.e. below 1000 K). The thermal conductivity of polystyrene $k(PS)$ was described with two temperature domains according to literature [66]:

$$273K \leq T \leq 416K : k(PS) = a_1 + b_1(T - 273.2K)^2 \tag{2.1}$$

$$T > 416K : k(PS) = 0.1659 \text{ W/(m K)} \tag{2.2}$$

with a_1 = 0.1455 W/(m K) and b_1 = 1.0 × 10^{-6} W/(m K^3). The heat capacity of polystyrene was defined in a similar way according to literature [67]:

$$273K \leq T \leq 373K : c_p(PS) = a_2 + b_2T \tag{2.3}$$

$$T > 373K : c_p(PS) = a_3 + b_3T \tag{2.4}$$

with a_2 = -95.668 J/(kg K), b_2 = 4.393 J/(kg K^2), a_3 = 740.25 J/(kg K) and b_3 = 2.934 J/(kg K^2).

For the thermal conductivity of the substrate (soda-lime glass) a line fit was used, based on the data for 173, 273 and 373 K [68]:

$$k(glass) = a_4 + b_4T \tag{2.5}$$

with a_4 = 0.5053 W/(m K) and b_4 = 1.750 × 10^{-3} W/(m K^2). The heat capacity was taken from literature [69] and implemented in the following form:

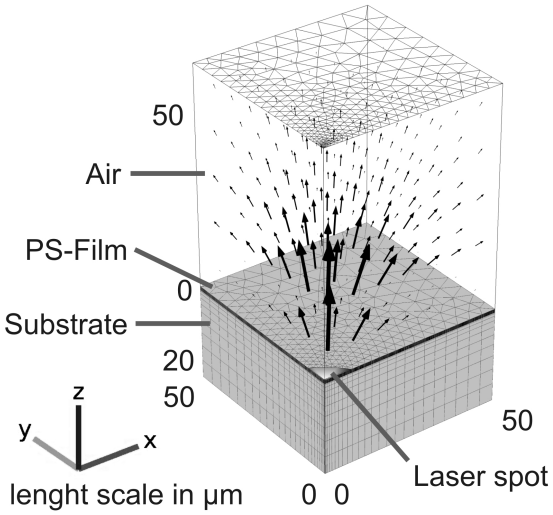

Figure 2.8: Geometry of the simulation model, including the mesh for the polystyrene film and the substrate. The arrows illustrate the velocity field of the thermal convection while the laser is heating the polymer surface.

$$c_p(glass) = a_5 + b_5 T - \frac{c_5}{T^2} \tag{2.6}$$

with $a_5 = 828$ J/(kg K), $b_5 = 0.4418$ J/(kg K^2) and $c_5 = 1.7186 \times 10^7$ J K/kg. The density of polystyrene was set to 1050 kg/m^3, the density of glass to 2530 kg/m^3.

The laser energy was introduced in the polymer layer via a volumetric heat source. The input energy was set to be the laser energy (measured with laser power sensor OP-2 Vis, Coherent GmbH) minus the transmitted and the reflected portion. The transmission was calculated according to an absorption measurement (spectrometer Lambda 900, Perkin Elmer) while the reflection was calculated according to the Fresnel coefficients. Only the reflection at the polymer air interface was taken into account. The reflection at the bottom of the polymer layer, i.e. the polymer glass interface was neglected.

The time dependence of the laser pulse shape was interpolated according to the measurement described in chapter 2.1.1 with results shown in figure 2.4. Furthermore, the heat source implies two Gaussian profiles in x and y direction based on the measured

beam dimensions of 6.9×12.3 µm^2 ($1/e^2$). Additionally, an exponential decay according to Lambert-Beer's law was used in z direction, based on an absorption measurement. Phase changes of the polymer layer while heated were neglected.

The mesh used for the finite element simulation was based on a triangular mesh type applied on the sample surface with 25 elements distributed along the two edges. A length ratio of 1/50 (center to outside) was applied. This mesh was extruded along the z-axis into all parts of the model. In the polymer layer a constant element thickness of 25 nm respectively 50 nm for films thicker than 1.5 µm along the z-axis were applied. For the substrate layer and the airbox, 10 elements were used in z direction with a ratio of 1/20, with small element size close to the polymer film. Within several numerical studies it was made sure that typical errors in the simulated temperatures due to discretization, mesh structure and limited extension of the model are well below 1 K.

3 Results and discussion

3.1 Temperature measurements

3.1.1 Data analysis

In order to prove the thermal nature of the recorded emission from the laser heating experiments, the data of several dye doped polystyrene films of different film thicknesses were analyzed. The emission in the center of the laser spot was integrated over an area of 1.3×1.3 µm^2. The result was plotted with the logarithm of the number of photons times the wavelength to the power of four versus $hc/k\lambda$ (figure 3.1). For thermal emission, a linear dependence should be evident in this plot according to the linearized form of Planck's law in the Wien region (equation 1.19). Plotted are only the wavelength intervals (bandpass filter) with reasonable signal-to-noise ratio (for (a) 600 to 760 nm, for (b) 570 to 760 nm and for (c) 540 to 760 nm). Indeed, a linear behavior was observed. For the thinnest film (figure 3.1 (a)), the linear fit resulted a temperature of 500 ± 9 K, the film in (b) resulted 630 ± 25 K and the thickest film (c) 760 ± 30 K. For two reasons, a higher temperature for thicker polystyrene films was expected. The higher absorption of thicker dye-sensitized polymer films is one reason. The other is the better thermal insulation behavior of the polymer in contrast to the substrate. This is discussed in more detail in chapter 3.2.3.

Only small deviations can be seen which stay within the error. The deviations towards high $hc/k\lambda$, i.e. small wavelength, increase. This is due to the lower thermal emission at smaller wavelengths and hence the lower signal-to-noise ratio which is also represented by the increase in size of the error bars in y-direction. At this point, it is important

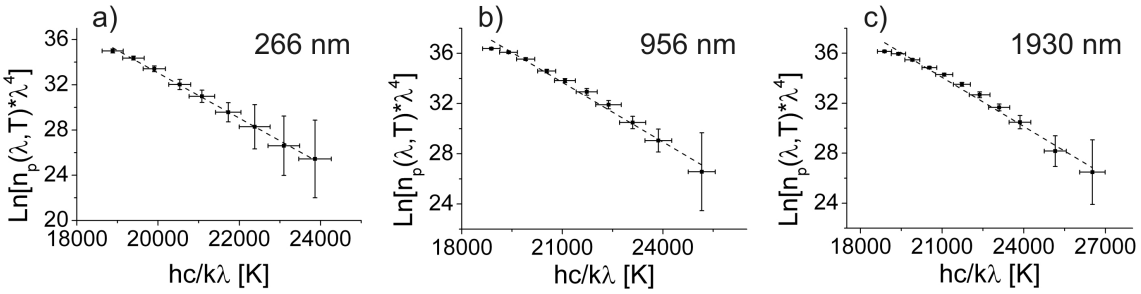

Figure 3.1: Integrated thermal emission at the center of the laser spot fitted with the linearized Planck formula (Wien region, Eq. 1.19). Data is based on area of 1.3 × 1.3 µm^2 of the thermal emission of a 266 nm (a), 956 nm (b) and 1930 nm (c) thick PS film including dye 1 (QDIBr) at a delay time of 14 µs. Other parameters: 1 µs integration time, 15 µs laser pulse with a fluence of 1.56 J/cm^2 (average fluence over area defined by $1/e^2$ beam diameters, as described in chapter 2.1.1).

to notice, that a better signal-to-noise ratio is found for higher temperatures. This is evident in the number of filters with reasonable signal-to-noise ratio and therefore with the number of data points increasing from (a) to (c).

The deviation at low $hc/k\lambda$, i.e. long wavelength is not so easy to explain, especially for the thicker films and higher temperatures found in (b) and (c). The filter at 760 nm shows a significant lower y-value as expected for a linear fit. A possible explanation can be a spectral dependence of the thermal emission. The film may not emit light according to the grey body approximation applied here, but with an additional wavelength dependence. This may either be the reason for the deviation at higher wavelengths, or the reabsorption of the film may play a role. Part of the thermal emission can be reabsorbed by the dye in the polymer film and consequently be invisible for the detector. The absorption of the dye has a strong dependence to the wavelength in the recorded range of 500 to 760 nm. This issue and its influence on data analysis will be discussed in more details in chapter 3.1.2.

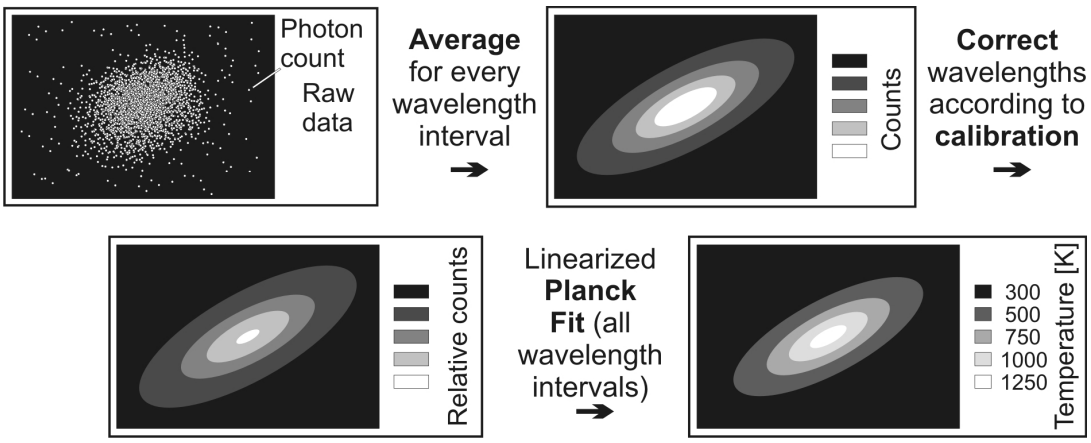

Figure 3.2: Scheme of data analysis for 2D temperature.

2D temperature distribution

In order to get a full 2D temperature graph the fitting procedure applied in figure 3.1 had to be conducted for every pixel of the recorded thermal emission images including data from every bandpass filter. The scheme in figure 3.2 illustrates the analysis. First the raw data, the single images of thermal emission for one filter, were averaged with a computer program (program written in labview 8.5.1). Then the photon counts were corrected according to the calibration (table 2.1) to get relative counts for each wavelength interval. After that a linearized Planck fit (equation 1.19) was conducted for every pixel including the data of all bandpass filters (wavelength intervals). The correction and the pixel-by-pixel analysis was done with a computer program (written in Python, version 2.5). Figure 3.1 already showed, that the signal-to-noise ratio is temperature dependent. For higher temperatures, the data for filters of lower center wavelength may be included while they must be excluded for lower temperatures. This led to the necessity to apply the following algorithm in the pixel-by-pixel analysis.

Instead of only one fit, multiple line fits were calculated for every pixel. First only the data of the highest three wavelength intervals were included in the calculation and subsequently one after another data point of the lower wavelengths was added. Then by comparison of the error of temperature resulting from each fit, the best fit was chosen. If the best fit for a pixel resulted in physical not meaningful temperature, i.e. below 300

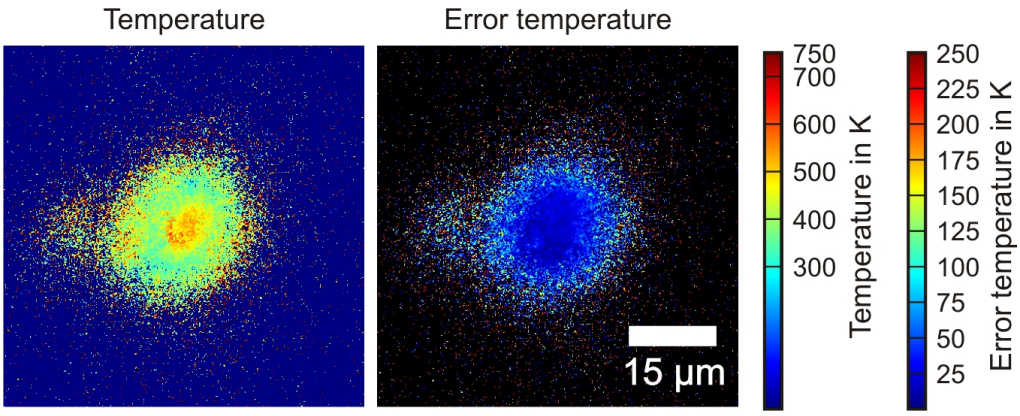

Figure 3.3: 2D temperature and error graph for 266 nm thick PS film including dye 1 (QDIBr) at a delay time of 14 µs. Other parameters: 1 µs integration time, 15 µs laser pulse with a fluence of 1.56 J/cm^2).

or above 3000 K, the next best fit was chosen. Additionally a fit with an error of more than 250 K was rejected. If no fit was found in between this temperature range with an acceptable error the pixel was set to 1 K for the temperature and 1000 K for the error. These pixels are colored in blue for 2D temperature graphs respectively in black for 2D error graphs.

Figure 3.3 shows a typical example for a 2D temperature and error graph. In the center of the spot the temperature is well defined. The uneven distribution is most probably due to physical effects, for example ablation, or differences from pulse to pulse. To the outer parts the noise becomes more evident, with single pixels resulting in a much higher temperature than their surrounding. A more rigorous setting of higher and lower limits or a smoothing of the temperature profile might lower the noise. However, it would also alter the result significantly with no additional information. Therefore no further processing is conducted on the 2D temperature and error graphs.

3.1.2 Influences of emissivity and absorptivity on the thermal emission

In chapter 1.2.5 the grey body approximation, i.e. constant emissivity over the regarded wavelength range, and its application in literature was introduced. In figure 3.1 a deviation of the emission was visible for the filter with longest wavelength (smallest $hc/k\lambda$), especially for the thicker films (figure 3.1 (b) and (c)). Even more important, these films showed a slight curvature besides the linear trend. This might be due to a spectral dependence of the emissivity. As discussed in chapter 1.2.5, according to the law of Kirchhoff (equation 1.23) the spectral emissivity is equal to the spectral absorptivity.

$$\epsilon_\lambda(T) = \alpha_\lambda(T) \tag{3.1}$$

According to this equation, the thermal emission should show a spectral dependence similar to the absorption spectrum. Figure 3.4 (a) shows the absorption spectrum of a polystyrene film including dye 1 (QDIBr).

In order to prove if there is a trend from the emissivity underlying the recorded thermal emission, an easy fit function according to equation 3.2 was applied. This fit function does not follow the fine structure of the spectrum but its basic trend. Only the relevant range of 500 to 760 nm is fitted.

$$f(\lambda) = a\lambda^8 \tag{3.2}$$

In the grey body approximation the emissivity is included in the fitting parameter A (see also equation 1.17).

$$n_p(\lambda, T) = \frac{A}{\lambda^4} \frac{1}{\exp(\frac{hc}{\lambda kT}) - 1} \tag{3.3}$$

If the emissivity is included with the dependence given in equation 3.2 the following equation results:

$$n_p(\lambda, T) = \frac{A' \cdot (a\lambda^8)}{\lambda^4} \frac{1}{\exp(\frac{hc}{\lambda kT}) - 1} \tag{3.4}$$

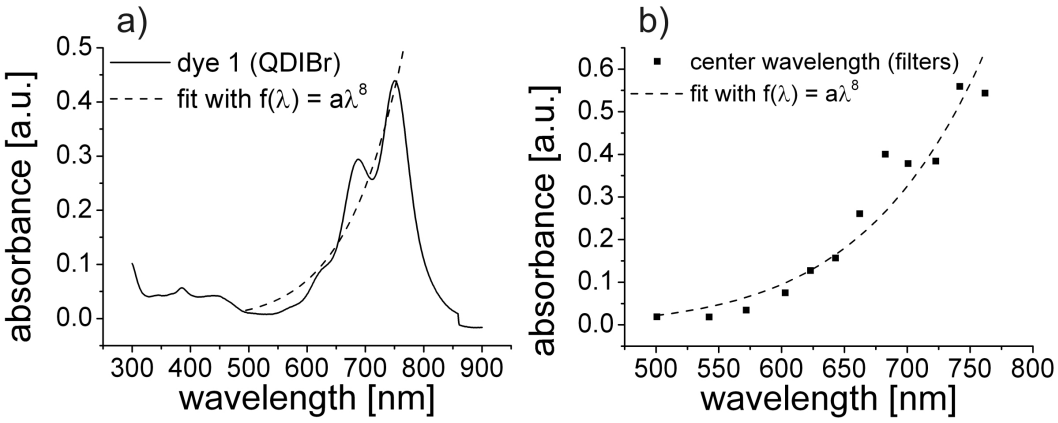

Figure 3.4: Absorption spectra of polystyrene film with dye 1 (QDIBr) including function $f(\lambda) = a\lambda^8$. Complete spectrum (a) and wavelength intervals (b) of the spectrum according to the bandpass filters of the detection system (table 2.1).

with the new fitting parameters A' and a. For simplification A' and a can be combined to one parameter $A'' = A' \cdot a$. Applying the Wien approximation analogue to 1.2.5, the following linear representation of Planck's law is obtained.

$$\ln[n_p(\lambda, T) \cdot \lambda^{-4}] = \ln A'' - \frac{1}{T}\frac{hc}{k\lambda} \tag{3.5}$$

Hence, a linear representation similar to the grey body approximation in equation 1.19 is found only with the logarithm of the number of photons per wavelength interval times the wavelength to the power of minus 4 instead of plus 4. With this result a linear fit of the recorded data was conducted, analogue to figure 3.1.

The graphs with the linear fits are plotted in figure 3.5. If compared to the graphs shown in figure 3.1 the line fit did not improve significantly. In contrast, the fit is slightly worse. The trend is now even more pronounced then it was without the correction of the emissivity. So the thermal emission according to the spectral emissivity can not be the reason for the deviation at long wavelengths or the non-linear trend.

Another possibility is the partial absorption of the light emitted by thermal radiation by the dye included in the polymer film. The polymer film might act as a filter. Thermal emission which originates from lower parts of the polymer film passes trough the film

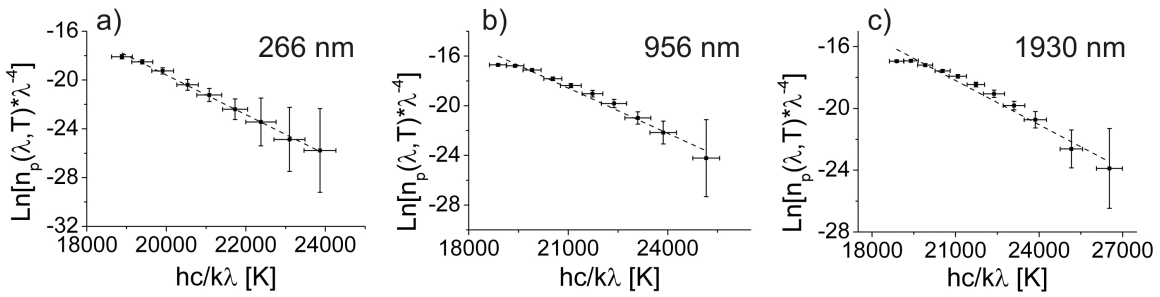

Figure 3.5: Integrated thermal emission at the center of the laser spot fitted with the linearized Planck formula including the emissivity in the form of equation 3.2 (fit equation: 3.5) for 266 nm (a), 956 nm (b) and 1930 nm (c) thick PS films. Experimental parameters analogue to figure 3.1.

before being recorded at the detector. This hypothesis can also be tested easily. The trend found in figure 3.4 can be used and applied in equation 3.3, inverse in respect to the application in equation 3.4.

$$n_p(\lambda, T) = \frac{A'}{\lambda^4 \cdot (a\lambda^8)} \frac{1}{\exp(\frac{hc}{\lambda kT}) - 1} \tag{3.6}$$

Analogue rearrangements of the equation results in equation 3.7 with an exponent of 12 for the wavelength on the left side of the equation instead of 4 or -4.

$$\ln[n_p(\lambda, T) \cdot \lambda^{12}] = \ln A'' - \frac{1}{T}\frac{hc}{k\lambda} \tag{3.7}$$

The corresponding graphs are shown in figure 3.6. Here, an improvement of the fit is apparent. For more systematic studies on several PS films with various film thicknesses and dye concentrations, an equal outcome is found (figure 3.7). While for the calculation including the emissivity a higher fit error is computed, the opposite is true if the polymer film is regarded as a filter for the thermal emission.

The temperatures resulting from the fits of figure 3.6 are presented in table 3.1. If the emissivity is included (T_{emiss}), higher temperatures are found. If the polymer film is included as an absorption filter (T_{filter}) the temperature is decreased. The fit for the temperatures in the latter case show the lowest fit error. But compared to the

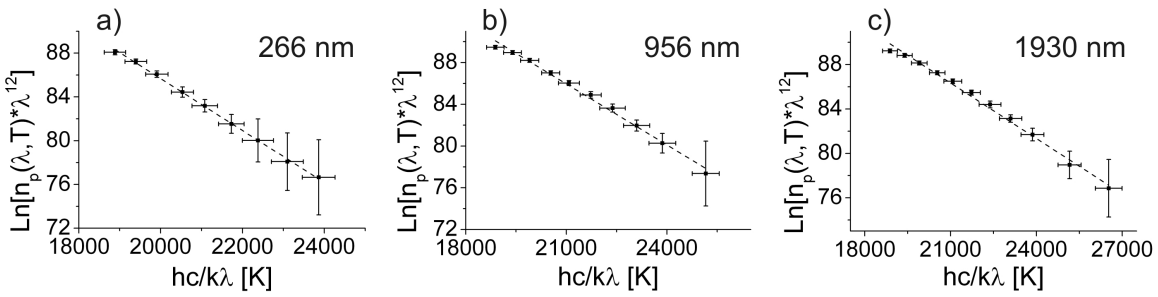

Figure 3.6: Integrated thermal emission at the center of the laser spot fitted with the linearized Planck formula including the polymer film as an absorption filter (fit equation: 3.7) for 266 nm (a), 956 nm (b) and 1930 nm (c) thick PS films. Experimental parameters analogue to figure 3.1.

film thickness [nm]	T (not corrected) [K]	T_{emiss} [K]	T_{filter} [K]	T_{sim} [K]
266	500	620	420	554
956	630	820	510	818
1930	760	1050	600	904

Table 3.1: Overview of the results of the correction including the emissivity or the film as a filter for the thermal emission.

temperatures found in a finite element simulations (T_{sim}), they seem unrealistic low. A loss of 60 to 70 % of the input energy would lead to temperatures in this range. Furthermore, the assumption of the polymer film as a filter for the thermal emission seems to be an exaggeration. Only parts of the thermal emission are passing through the polymer film on the way to the detector, not the whole thermal emission.

Influence of dye. Samples including different dyes were analyzed in a similar matter. In this way, it can be proven that the behavior is not unique for dye 1 (QDIBr). The absorption spectra of polystyrene films including the different dyes are shown in figure 3.8. All three dyes show considerable absorption at the laser wavelength. They are all efficient molecular heater (further discussion of the behavior of the different dyes can be found in chapter 3.2.7).

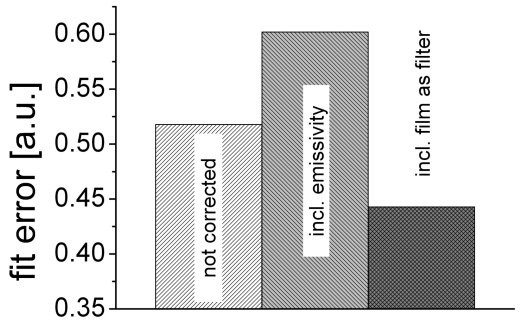

Figure 3.7: Results of the fit for linear fits for various polystyrene films illuminated at different laser power.

The spectral dependence of the absorption in the range used for data analysis differ from each other. In order to quantify the influence, a simple fit function was found in the range of 500 to 760 nm (figure 3.9) analogue to the dye 1 (QDIBr). Equation 3.8 is used for dye 2 (QDI) and equation 3.9 for dye 3 (QDIS).

$$f(\lambda) = a\lambda^9 \tag{3.8}$$

$$f(\lambda) = a\lambda^7 \tag{3.9}$$

With these fit functions for the emissivity, the linear representation of Planck's law does have an exponent of -5 respectively -3 for the wavelength in the logarithm. If the polymer film is regarded as a filter, analogue to the calculation with dye 1 an exponent of 13 respectively 11 is found.

The data is plotted in figure 3.10. The conclusion is similar to the one for dye 1 (QDIBr). The line fit gets worse if the emissivity is taken into account according to Kirchhoff's law (equation 1.23). If the polymer is regarded as an absorption filter the fit improves. This is also evident for the fit error (figure 3.11).

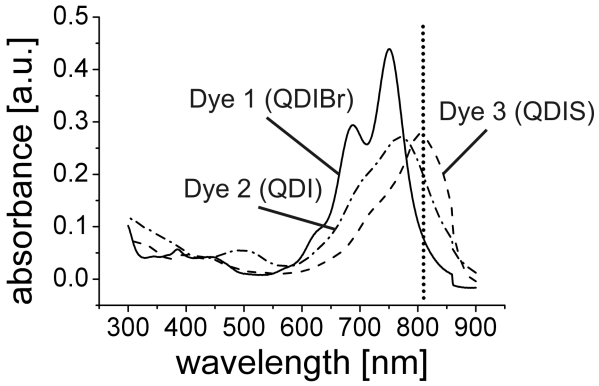

Figure 3.8: Absorption spectra of polystyrene films with different dyes. The dotted line represents the laser wavelength of 810 nm.

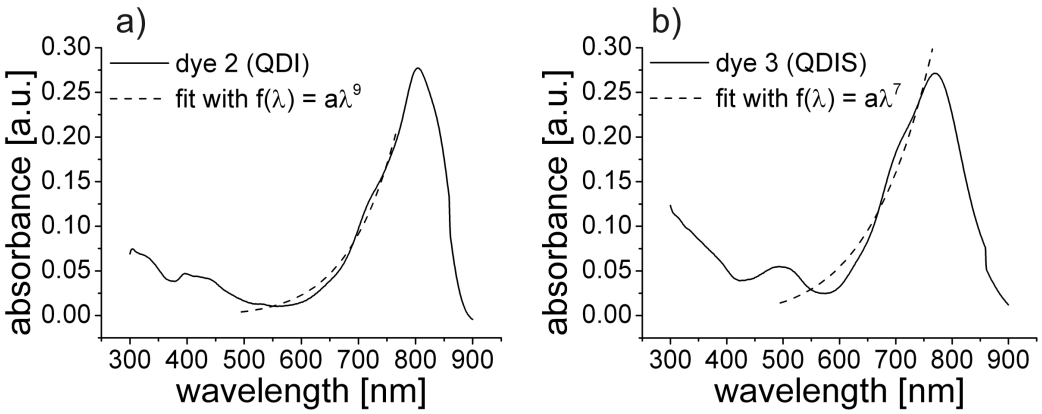

Figure 3.9: Absorption spectra of polystyrene films with dye 2 (QDI) (a) and dye 3 (QDIS) (b) including fit function.

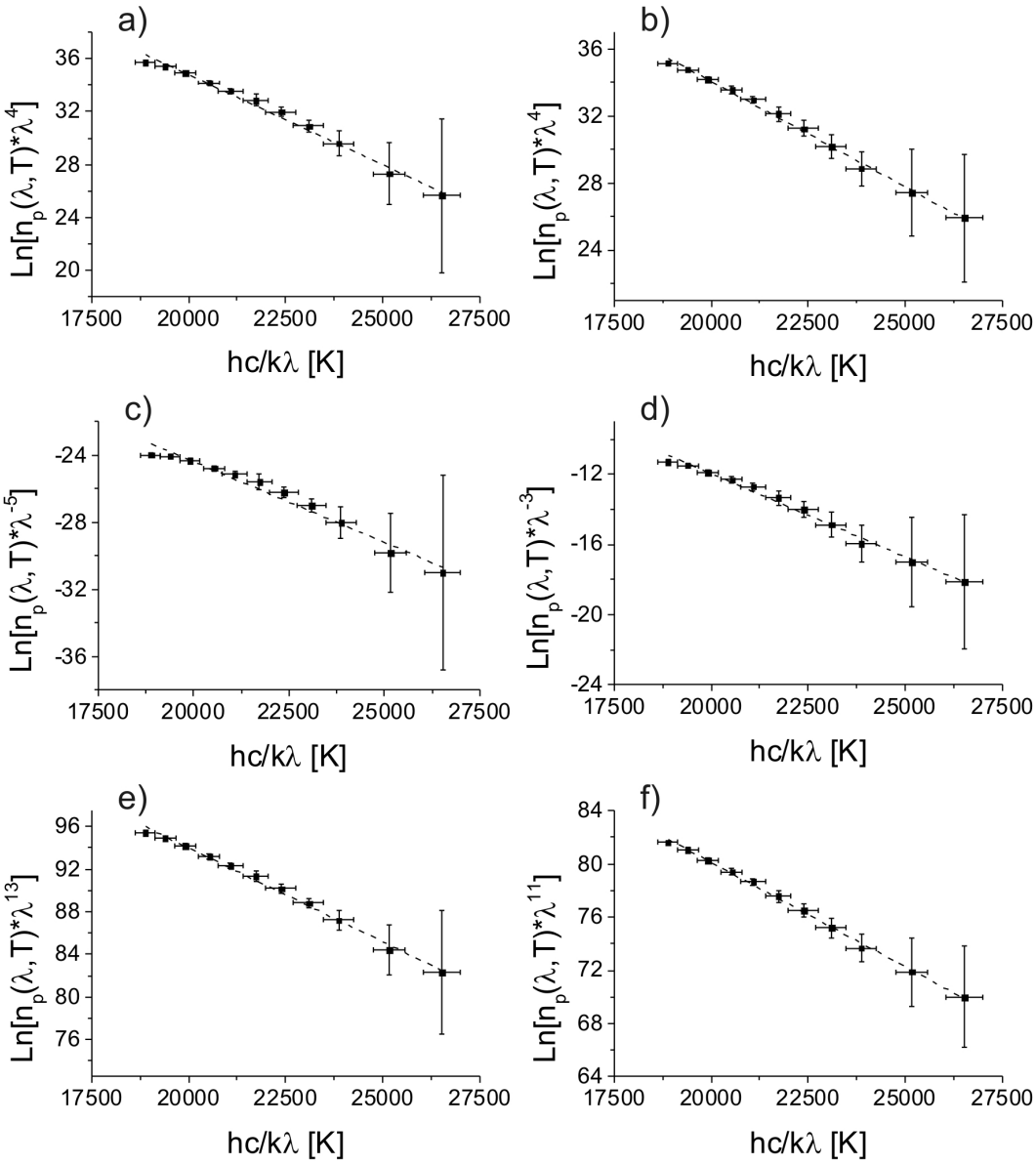

Figure 3.10: Integrated thermal emission at the center of the laser spot fitted with the linearized Planck formula for dye 2 (QDI) in the first column (a,c,e) and dye 3 (QDIS) in the second column (b,d,f). In (a) and (b) the linear Planck formula without correction (grey body approximation) according to equation 1.19 is applied. In (c) and (d) the emissivity was set according to equation 3.8 respectively 3.9. In (e) and (f) the polymer film was included as an absorption filter. Experimental parameters analogue to figure 3.1.

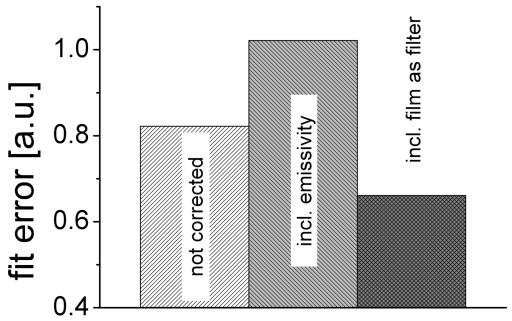

Figure 3.11: Results of the fit error for linear fits of polymer films including the different dyes (2 and 3).

In summary, the data analysis including the emissivity according to Kirchhoff's law results in a deterioration of the linear fit. The following explanation gives reason for this finding. The polymer films used for the measurements typically contain only 3-10 % of dye in respect to the polymer. Most of the heated matter is therefore the polymer itself. The polymer is almost completely transparent in the region of 500 to 760 nm, the range in which the thermal emission is recorded. The dye is responsible for the absorption characteristic in this region. Most of the emitting matter when heated is polymer, i.e. a matter with constant low absorptivity in the range of 500 to 760 nm. Consequently, Kirchhoff's law is not applicable here because the emitting polymer film is not one homogeneous matter.

A small influence of reabsorption can on the other hand be expected. Not only the surface of the polymer film emits thermal radiation. The most heated parts of the polymer film can be found at or just below the surface as can be shown by finite element simulations (figure 3.12). However, the simulations provide an explanation for higher deviations for thicker polystyrene films. The peak of the maximum temperature shifts to the inside of the polymer film with increasing film thickness. For 266 nm (figure 3.12 (a)) the maximum temperature is at the surface, for 1930 nm (figure 3.12 (c)) it is already shifted by about 300 nm underneath the film surface. The filtering effect should

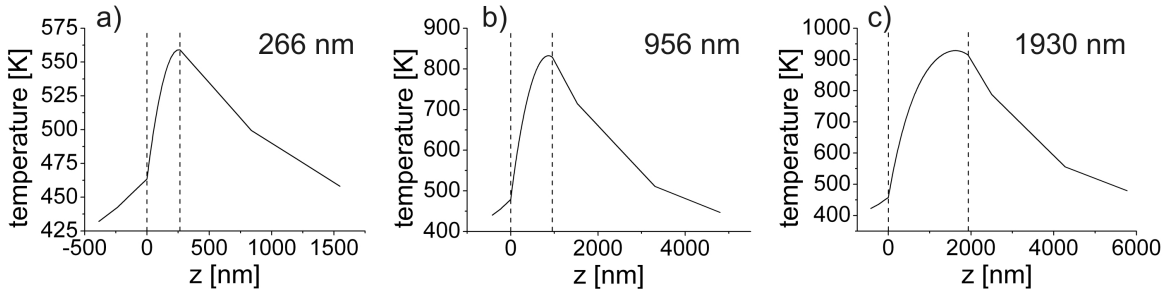

Figure 3.12: Simulated temperature distribution at the center of the spot (x = y = 0) for 266 nm (a), 956 nm (b) and 1930 nm (c) thick PS films. The dashed is marking the polymer film. Experimental parameters analogue to figure 3.1.

consequently be more pronounced for the thick film. Quantification of the amount of filtered thermal emission with respect to unfiltered emission from the surface is nevertheless difficult. Especially if the effect of ablation is considered. Holes are formed in the polymer film by the laser pulse as will be discussed later. This is neglected for the simulations.

In conclusion, the grey body approximation is the most meaningful approach.

3.1.3 Temperature measurements on heatable atomic force cantilever

As a reference system to laser heated polymers, the temperature distributions on heatable atomic force microscopy cantilevers were measured. The cantilevers used for this purpose incorporate a resistive heater at the tip. By tuning the electric potential and current, the tip can be heated. It can either be operated in steady-state, as it is done here, or the potential and current can be modulated. The latter is typically done in an AFM application to probe the softening point of materials. Figure 3.13 is showing a scanning electron microscope image and a 2D temperature graph of such a heatable cantilever.

Here, the prove of principle is provided that the temperature measurement method is

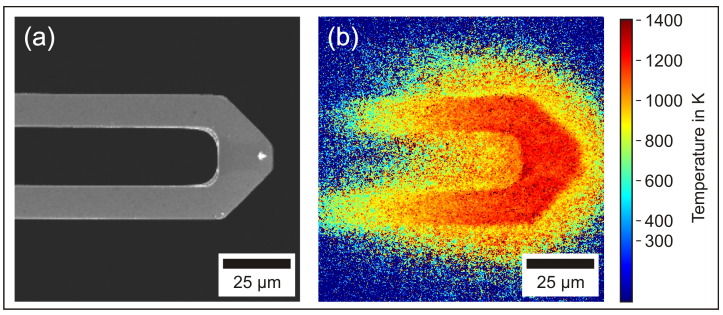

Figure 3.13: Scanning electronic microscope image (a) and 2D temperature graph (b) of heatable AFM cantilever (4.5 V, 8.31 mA), Integration time of 1000 µs.

not only applicable to laser heated polymer films but also to other systems. Additionally, the experiments demonstrate that not only the heated surface of the cantilever is visible, but also its heated air corona. This indicates an important fact for temperature measurements in laser heating experiment. Not only the surface of a laser heated polymer film, but also the surrounding heated air and eventually occurring hot ablation products are visible in the temperature measurements. The 2D temperature graphs show the entire heated matter in the focal volume of the objective.

If the integrated thermal emission at the tip of the cantilever is regarded (figure 3.14) a good agreement to the linear fit is found. The temperature resulting from the fit is 1115 ± 10 K. There is no deviation at small $hc/k\lambda$ (long wavelength) and no underlying additional trend as it was found for the laser heated polymer films. This indicates, that these effects can be addressed to the dye polymer sample and are not a general effect of the method. The error bars of the logarithm of the number of photons times the wavelength to the power of 4 (y-axis) increase in size for high $hc/k\lambda$ (small wavelength). However, this can be attributed to the lower signal-to-noise ratio at small wavelength.

Compared to the graphs for the laser heated polymer films (e.g. figure 3.1), the y-error bars are bigger for the cantilever. This is especially interesting because a higher temperature was regarded and a 1000 times longer integration time was used for the cantilever. Thermal fluctuations in the resistive heater of the cantilever can be a possible explanation. With the applied average, thermal fluctuations do not influence the mean

of the thermal emission. Therefore, the good agreement is present between the line fit and the experimental data. The error bars in figure 3.14 reflect the thermal fluctuations, i.e. the deviation from the mean. These fluctuations are higher than in the previously presented pulsed laser heating experiments.

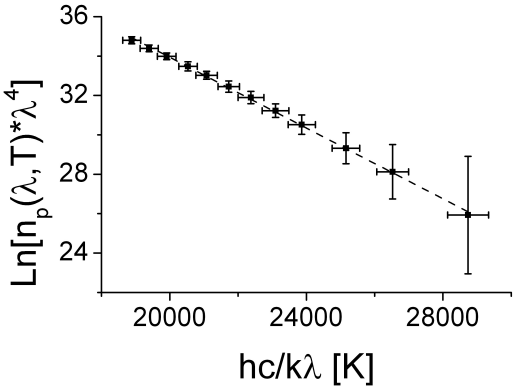

Figure 3.14: Integrated thermal emission of the tip of a heatable AFM cantilever fitted with the linearized Planck formula (Wien region, Eq. 1.19). Results are based an integration of an area of 1.3 × 1.3 µm^2) (based on emission data corresponding to figure 3.13).

3.2 Laser heating experiments on polystyrene samples

3.2.1 Time dependent measurements during pulsed laser heating

2D temperature graphs

In order to analyze and understand the temperature behavior in pulsed laser heating a temperature measurement was conducted with various delay times for two samples of different polymer film thickness (figure 3.15). The heating and the cooling phases are visible with a maximum temperature of about 600 K at a delay time of 14 µs for the thin film and up to 800 K, at some parts even more than 1000 K, for the thick film at a delay time of 16 µs.

The thick polymer film does reach higher temperatures because of two reasons. First, the absorption at the laser wavelength of the thick film is higher than for the thin film. With a higher absorption, more laser energy can be converted into heat leading to higher temperatures. Second, the polymer is roughly one order of magnitude less thermally conductive than the glass substrate. It is therefore insulating its own heat dissipation. The thicker the polymer film the better the insulation behavior.

For the thin film (figure 3.15 (a)) the temperature distribution is more or less following the Gaussian beam profile (figure 3.16). The fit yields a maximum temperature of 530 $\pm$ 10 K and a FWHM of 6.7 $\times$ 8.1 µm^2 at a delay time of 14 µs. Compared to the beam diameter (chapter 2.1.1), it is apparent that the size ratio between long and short axis of 1.8 is not maintained. Here, a ratio of 1.2 is found. This is most probably due to the high average applied and slight surface varieties from pulse to pulse. Even though the sample tilt is corrected for every experiment, a small tilt often remains. In consequence, the spot moves small portions in one direction from first to last pulse of a temperature measurement. This may lead to a broadening or even to deformations of the hottest region in the 2D temperature graphs in one direction. Here, most probably a broadening along the short axis took place.

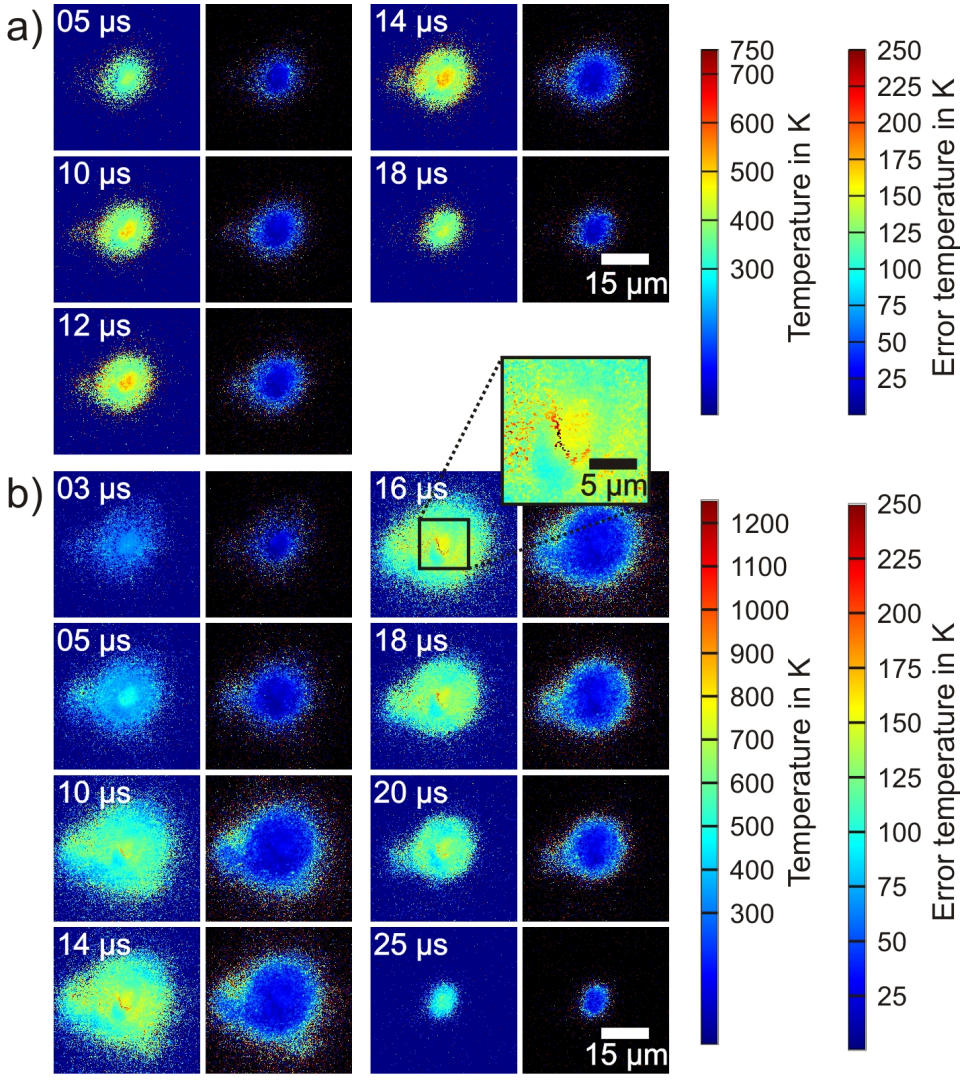

Figure 3.15: 2D temperature graphs of 266 nm (a) and 956 nm (b) thick PS film including dye 1 (QDIBr) at various delay times. Other parameters: 1 µs integration time, 15 µs laser pulse with a fluence of 1.56 J/cm^2.

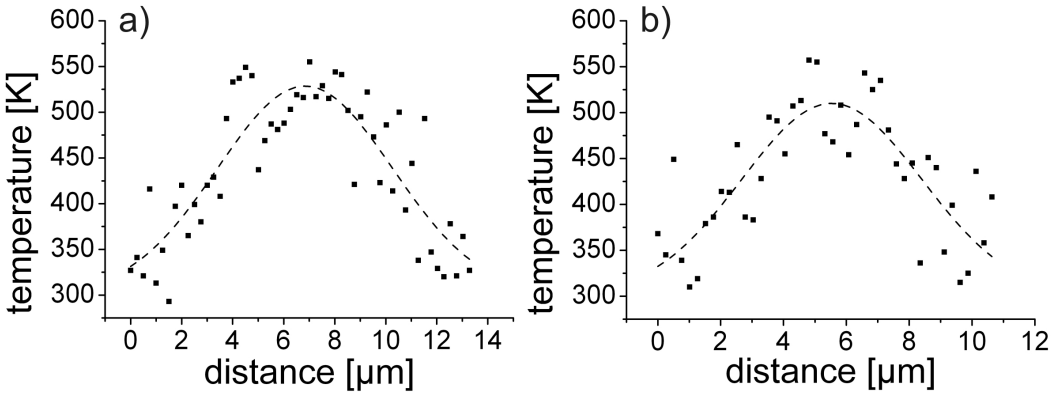

Figure 3.16: Line scan along long (a) and short (b) axis of the hot area in figure 3.15 (a), delay time of 14 µs including Gaussian fit function (dashed line).

In general the 2D temperature profile for the thin film can be divided in three zones. A hot core area, with 500-600 K and 4 × 6 µm^2 at maximum, a cooler corona, with 400-500 K and 16 × 18 µm^2 at maximum and a not heated surrounding.

For the thick film this kind of description is only possible for 3, 5, 20 and 25 µs, the start of the heating phase and the end of the cooling phase. In between, a more complex temperature distribution is found. The Gaussian beam profile is not maintained in the temperature graphs. A hot inner part of again 4 × 6 µm^2 at maximum is heated up to around 800 K at a delay time of 16 µs. However, the surrounding corona, with about 24 × 25 µm^2 at 16 µs delay time, shows an inhomogeneous temperature distribution. Although not as concentrated as in the center, a big area with temperatures of around 800 K can be seen. Only the more outer parts show a lower temperature of 500-600 K.

Influence of ablation

For the 956 nm thick film at 16 µs delay time, a crescent shaped area with a temperature above 1000 K was observed (figure 3.15 (b)). This area can be understood if the effect of the laser beam on the polymer film is taken into account. Ablation occurs for both films at the laser fluences applied here (figure 3.17). For the thin film ablation is limited, holes of about 10 nm are formed, 4 % of the film thickness. For the thick film holes of

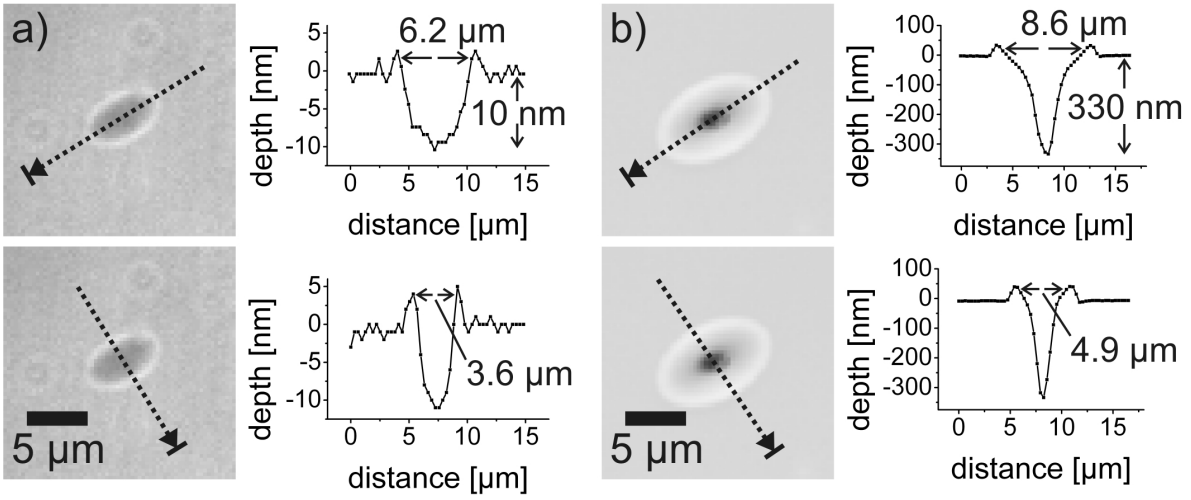

Figure 3.17: Confocal white light profiles of 266 nm (a) and 956 nm (b) thick PS film including dye 1 (QDIBr). 15 µs laser pulse with a fluence of 1.56 J/cm^2.

270 ± 60 nm are found, about a quarter of the film thickness.

One would expect a Gaussian temperature distribution with a Gaussian laser pulse profile. But the temperature distribution depends on the input energy which itself depends on two factors, the laser energy profile and the absorption profile. The latter is given by the local film thickness, i.e. the thickness of the absorbing matter. If only a small part of the film is ablated, the absorption profile stays uniform and it has no or only little influence on the temperature distribution. This is the case for the thin film. Whereas if considerable amount of the polymer film is ablated, less input energy is available. The center of the laser spot is still the point of highest laser energy, but not of highest energy input anymore. If an angle of incident of 0° would have been chosen, the Gaussian distribution would in this way be altered to a "flat-top" distribution. With the applied angle of incident, the crescent shaped areas are caused. These areas most likely represent the side walls of the ablation holes opposite of the laser, where the absorbing film was not reduced considerable and the laser energy is still high enough. However, I like to point out that the applied methods detects the thermal emission from all matter. Heated air, polystyrene or decomposition products from the ablation process of polystyrene, i.e. oligomeres, styrene or other compounds arising of

the styrene decomposition, might also be seen here. Most probably a combination of both is true. The process of decomposition of the side wall is visualized. The distortion of the temperature profiles can also be seen in the ablation profiles (figure 3.17 (b)). With the laser illuminating the sample from top right (analogue to the 2D temperature profiles in figure 3.15), the lower left part of the holes for the thick film is the deepest.

The maximal temperature observed for the thin film of 500-600 K led to an onset of ablation (figure 3.17 (a)). Comparing the diameter of the holes in the surface profiles with the temperature graphs they fit quite well. For the holes an average size of $3.5 \pm 0.1 \times 6.2 \pm 0.1$ µm^2 was found (measured on film level, compare figure 3.17) while the temperature range of 500-600 K extended up to 4×6 µm^2 (figure 3.15 (a)).

For the thick film, 800 K is reached in the center and considerable ablation was observed. Holes in the film show an average extension of $5.0 \pm 0.1 \times 8.7 \pm 0.1$ µm^2. The ablation holes did not agree with the temperature graph. The hot core area with 4×6 µm^2 represents the inner parts of the holes, but the corona with 24×25 µm^2 can not be found in the surface profiles. For the thin film 500-600 K already led to an onset of ablation, a temperature range exceeded by large parts of the corona. Regarding the inhomogeneous temperature distribution, it is most likely that the outflow of gaseous material is visualized. This can also explain the diffuse nature. The matter which is responsible for the thermal emission is not on the polymer surface but several micrometer above, and therefore not in the focus of the objective any longer. With the high average of individual pulse experiments for one 2D temperature graph (almost 2000 pulses), the resulting temperature distribution should be diffuse and inhomogeneous.

Center temperature and simulation

In order to better understand the heating and cooling process, the center temperature was calculated for all delay times. Therefore, 100 pixel (corresponding to an area of 1.3×1.3 µm^2) in the center of the spot were averaged. The experimental result was compared to the result of a finite element simulation (figure 3.18). In this simulation only energy conversion and heat dissipation was taken into account. Phase changes or the ablation

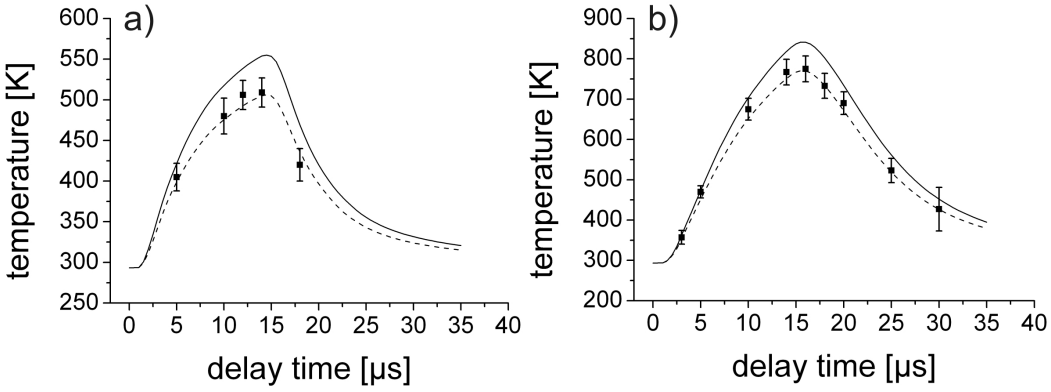

Figure 3.18: Center temperature vs delay time of 266 nm (a) and 956 nm (b) thick PS film including dye 1 (QDIBr). The squares represent an average of 1.3 × 1.3 µm^2 in the center of the 2D temperature graphs of figure 3.15. The continuous lines show simulated results assuming that all absorbed energy is converted into heat. For the dashed lines an energy loss of 20 % in (a) and 15 % in (b) was assumed.

process of the polymer were neglected. The simulated temperatures exceed the measured ones. Therefore, a loss factor was introduced in the volumetric heat source to fit the simulation to experiment. Possible loss mechanisms are fluorescence or phosphorescence, especially of the excited organic dye, or chemical degradation of the polymer film. The used dye is known to show moderate fluorescence [65].

Experimental and simulated curves agreed best when a loss of 20 % for the thin film and 15 % for the thick film was assumed. The difference of 5 % is not significant, considering the error bars in temperature. A higher loss factor was expected for the thick film with an ablation of about 25 % of the film thickness in contrast to only 4 % for the thin film. Thermal degradation and depolymerization of polystyrene are endothermic reactions. However, systematic errors cannot be excluded. An error in for example the absorption or film thickness measurement has a high influence on the result as they are both input values for the simulation.

Compare 2D temperature graphs to simulations

When comparing experimental and simulated 2D temperature distributions, good agreement was found for the thin PS film (figure 3.19 (a) and (b)). As an example, the 2D temperature distributions for a delay time of 14 µs are compared. The size of the core area in the measured temperature graph (red and orange), is slightly larger than the one in the simulation. This can be due to the fact that the temperature graph is the result of an average over almost 2000 laser pulses. A new, fresh sample area has to be used for every laser pulse. So small deviations from pulse to pulse are inevitable. Besides, deviations can also be possible due to misalignment of the sample tilt, already described earlier. Simulations showed that, due to the thermal diffusion, the ratio of long to short axis is reduced from 1.8 (beam diameter ratio) to 1.6. However, a ratio of 1.2, found here in the experiments, must be due to deviations from pulse to pulse or misalignment. The noise on the outer parts can be attributed to the low signal-to-noise ratio at lower temperature.

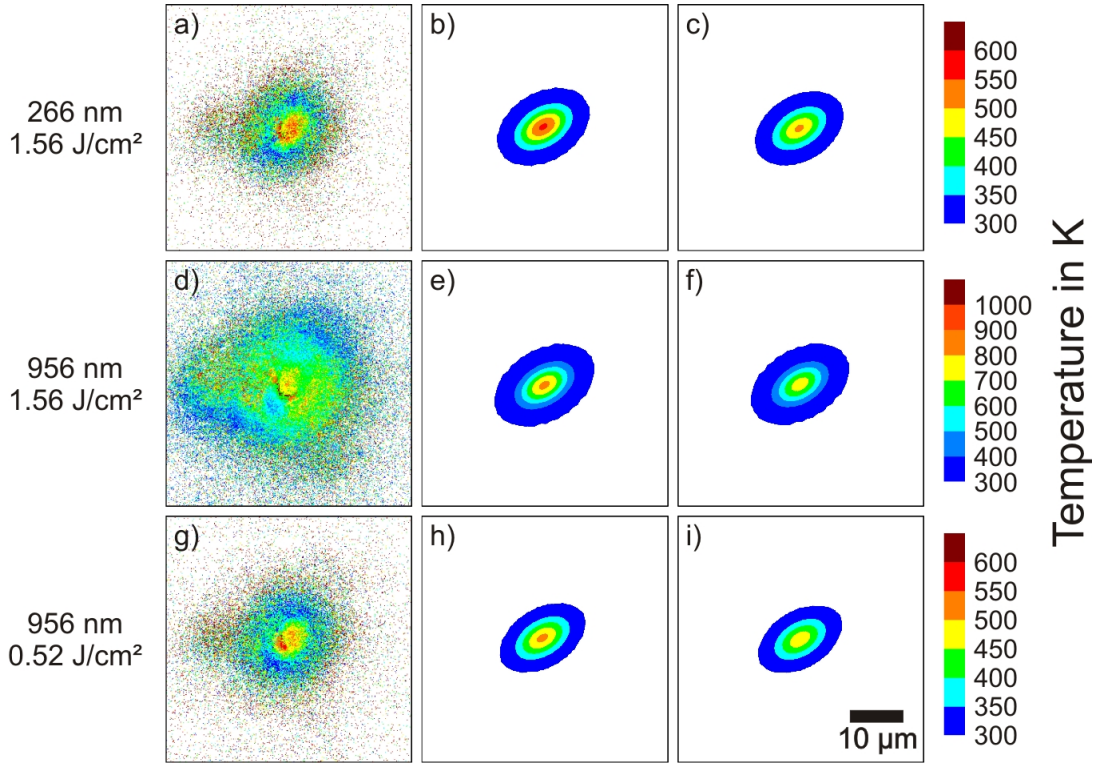

Figure 3.19: Measured and simulated 2D temperature graphs for 266 nm (a-c) and 956 nm (d-i) PS films. For 956 nm high laser power is shown in (d-f) and low laser power in (g-i). The first column (a,d,g) represents the measurement, the second simulated data with no energy loss (b,e,h) and the third with energy loss (c,f,i) (energy loss of 20 % in (c) and 15 % for (f) and (i)). Other parameters: delay time of 14 µs, integration time 1 µs, 15 µs laser pulse. Film thickness and fluence are given in the image.

When taking an energy loss of 20 % into account, the peak temperature and the width of the temperature profile are decreased (figure 3.19 (c)). Although the calculated average center temperature fits well with the simulation (figure 3.18), the 2D image does not show better agreement to the measurement than the no-loss image. The red and orange area (500-600 K) in the measured graph (figure 3.19 (a)) resemble more the no-loss image (figure 3.19 (b)). The measured data include noise, while a perfect Gaussian distribution is found in the simulation. This might also be induced by the small displacement from pulse to pulse. Additionally, the outflow of gaseous ablation products from the center might enhance the noisiness. In conclusion, the loss is overestimated by adjusting the simulation to match the measured center temperature with a loss factor. An adjustement is helpful in order to follow the time dependence of the temperature, but in general the no-loss simulation is preferable.

For the thick film case a comparison of the 2D temperature graph with the simulation shows some discrepancies (figure 3.19 (d to i)). For high laser power the experimentally observed hot area is larger than in the simulation (3.19 (d to f)). Only the temperatures in the center agree (yellow area). Here again, the measured temperature distribution agreed best with the simulation for a loss between 0 and 15 %.

The larger size of the heated area can be attributed to ablation. This was already indicated in the comparison between 2D temperature graphs and surface profiles (figure 3.15 and 3.17). Hot material being thrown out of the central hole into the surrounding atmosphere can cause the effect. This part is rather noisy, most likely because it is not in the focus of the objective any longer but some micrometer above the polymer surface. Ablated material was shown to be ejected with speeds in the order of the speed of sound by Lee et al. using ultrafast microscopy [2]. Therefore one might conclude that it should leave the field of view in a fraction of a microsecond and be invisible to the detector. However, a constant stream of material should still be visible. Especially the diffuse, noisy nature of the bulge area in the left part of figure 3.19 (d) supports this explanation. Overall, the comparison between experiment and simulation supports the hypothesis that a combination of different effects, heated surface, ablated material, and

heated gaseous products, lead to the shown 2D temperature graphs.

At low laser power (figure 3.19 (g to i)) the result on thick films is almost similar to the result for thin films. Only little ablation of 36 ± 2 nm in average (about 4 % of the film thickness) was found. Again, a broadening of the temperature zone in the measurement is visible. A crescent shaped area is observed, which cannot be seen in the simulation. However, the influence of ablation seems to be negligible. Just like for the thin film case, the 2D temperature graph fits well to the simulation.

Temperature dependence of heat capacity and thermal conductivity

Several assumptions are used for the simulation. It could already be shown that the ablation can have a significant influence on the result. However, implementing ablation would have complicated the simulation significantly and would introduce more adjustable parameters. Another assumption can easily be tested: the extrapolation of the heat capacity and the thermal conductivity of polystyrene. It is not trivial to use the extrapolation, especially not beyond the degradation temperature of the material itself. Therefore we tested the simulation using constant parameters instead of the extrapolation. The parameters for room temperature (293 K) and for 373 K, the glass transition temperature for high molecular weight polystyrene [52], were used. The assumption of constant parameters might thereby be justified by the fast time scale of the laser heating. The adjustment of the polymer properties to the temperature might be delayed and better be approximated by constant values for low temperature.

The result of the center temperature versus time is shown in figure 3.20. For thin films with a maximum center temperature of about 520 K, the simulations for constant and temperature dependent parameters both agree with experimental results. For the thick film, the simulated temperature rise is much higher. Using the temperature dependent parameters obtained by extrapolation provides the best agreement with the experiment. A description of the thermal parameters with constant values for 373 K does not result in a big deviation. In conclusion, the extrapolation of the thermal parameters even beyond melting or degradation temperature is feasible. A simplification of the model by using

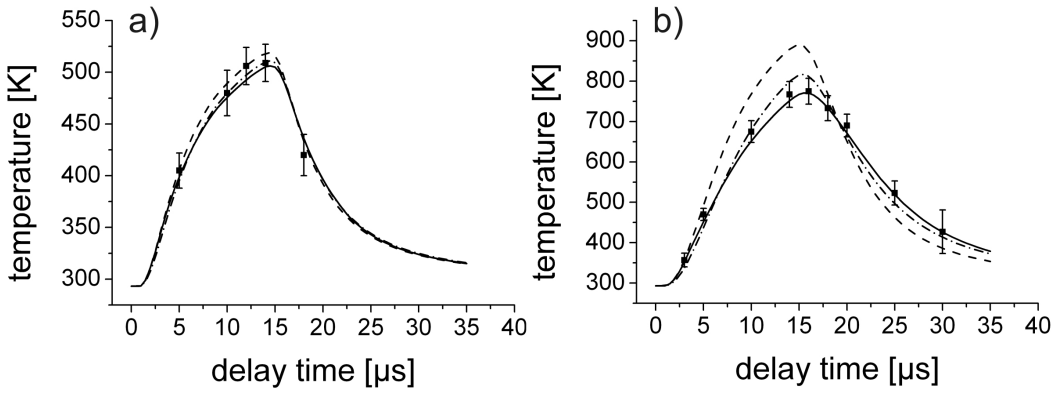

Figure 3.20: Influence of simulation parameters. Center temperature vs. delay time for different film thicknesses of 266 nm (a) and 956 nm (b) PS film; measured data is shown in squares. The compact line is showing simulation data incl. temperature dependent thermal conductivity $k(PS)$ and heat capacity $c_p(PS)$ for polystyrene, the dashed line simulation data including constant $k(PS)$ and $c_p(PS)$ according to literature at 293 K [66, 67] and the dashed-dotted line simulation data including constant $k(PS)$ and $c_p(PS)$ according to literature for 373 K [66, 67] (all simulations include 20 % (a) respectively 15 % (b) energy loss, experimental parameters see figure 3.15).

constant values given at the glass transition temperature is possible.

3.2.2 Ablation mechanism

The ablation mechanism for the polymer-dye sample system is photothermal since polystyrene is transparent at the NIR wavelength of the laser. The organic dye is absorbing and converting the laser light into thermal energy. A photochemical decomposition of the dye molecules can be ruled out. There are several counter arguments. The ablation holes do not have sharp edges, but are round. A decomposition of dispersed molecules would lead to explosive craters, not round holes. A second argument is the good agreement between temperature measurement and simulation (figure 3.18, 3.19). In the simulation the laser energy is coupled into the polymer film via a volumetric heat source. This

result supports the function of the dye molecule as a molecular heater.

Thermal decomposition for the polystyrene starts at 546 K, when measured at quasi-equilibrium heating rates of 10 K/min [52]. Regarding the temperature in the center of figure 3.15 (a) (266 nm polymer film) for delay times of 12 and 14 µs, this temperature agrees with the onset temperature observed here. However, the time scale is different by eight orders of magnitude. Applying the law of Arrhenius, the temperature for decomposition should increase if the temperature is applied only for a short time. For this reason, ablation should not occur at 500-600 K applied for few µs. Still, holes are formed, demonstrating polystyrene ablation. Spinodal decomposition, the instantaneous decomposition into gas and liquid droplets after superheating, can also be ruled out at these temperatures. Johnson et al. [4] suggested this as the ablation mechanism for resonant infrared laser heated polystyrene on the 10 microsecond time-scale. They estimated the temperature to be in the order of 1300 K for polystyrene for laser heating on the 10 microsecond time scale. A closer inspection of the ablation threshold respectively ablation at low temperature including more than two samples and a variation in laser power reveals a significant photomechanical contribution. This study is described later in this chapter.

For the thick film (figure 3.15 (b)), being in a 300 K higher temperature regime compared to the thin film, it might well be possible that the ablation mechanism or at least the dominating process of ablation is different. Thermal decomposition seems to be dominating, if the maximal temperature is well above the threshold. Applying again the law of Arrhenius, a temperature difference of 300 K allows a shift of the timescale by several orders of magnitude. Figure 3.19 supports this interpretation as well. The comparison between measured and simulated 2D temperature graphs indicates the turbulent outflow of hot, gaseous material (figure 3.19 (d) and (e)), as it would be expected for a thermal decomposition reaction.

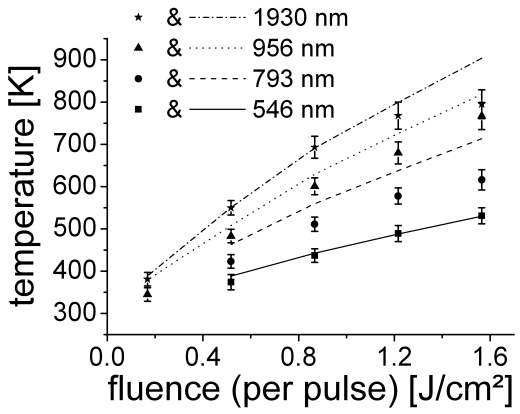

Figure 3.21: Center temperature (averaged over 1.3 × 1.3 µm^2) vs. laser fluence for different film thicknesses containing equal amount of NIR-dye; The points represent measured values, while the lines are showing the simulation with no energy loss. Other parameters: delay time of 14 µs, 1 µs integration time, 15 µs laser pulse.

3.2.3 Film thickness

An important finding of the measurement and the simulation is the high influence of the film thickness on the laser heating process. Therefore, polystyrene films of a thickness ranging from 546 nm to 1930 nm with equal dye-to-polymer ratio were exposed to different laser fluences. The 2D temperature graphs for a fixed delay time were acquired. The result, in form of the center temperature versus fluence including a comparison to simulation is shown in figure 3.21. For the simulation shown in this graphs no energy loss was taken into account. Within the experimental and systematic errors, good agreement was found, in particular for fluences up to 1 J/cm^2. Systematic errors include for example variations in film thickness, which have a high impact on the measured temperature. Not only the absorption of the film changes, but also the insulation of the most heated top part of the film by itself. For example in a simulation for the 956 nm PS film, a variation in film thickness of only 5 % results in a temperature difference of ± 20 K (1.04 µJ laser energy corresponding to a fluence of 1.56 J/cm^2, 14 µs delay time). Variations of the film thickness in this order of magnitude are typically found for the applied blade

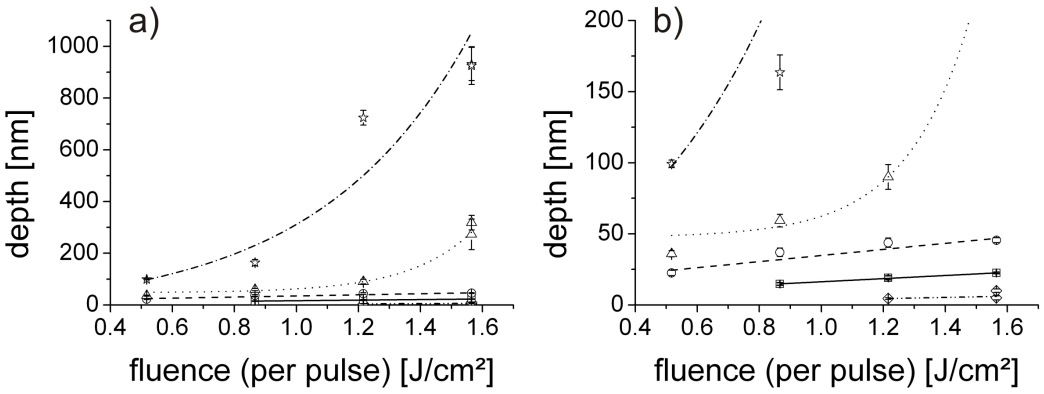

Figure 3.22: Ablation depth vs. laser fluence for different film thicknesses. Diamonds represents 266 nm, squares 546 nm, circles 793 nm, triangle 956 nm and stars 1930 nm; (a) is giving an overview while (b) shows the graph for small ablation depths. The lines are a guide for the eye. Other parameters: 15 µs laser pulse.

coating procedure. Film thickness and absorption are important for the measurement and are input parameters for the simulation. The comparison between experiment and simulation is sensitive to errors of these parameters.

At high fluences the difference between measurement and simulation is increasing. This is due to the ablation of the polymer film. Especially for the thickest film of 1930 nm the trend is visible. At the highest fluence, holes of 930 $\pm$ 70 nm in depth were formed, almost half of the film thickness. The temperature is decreased due to energy consumption of the ablation process. Additionally, if half of the film is lost, the absorption and the thermal insulation is considerable decreased. Both effects lead to lower temperatures. In contrast, for the 546 nm film, the deepest holes were found to be 23 $\pm$ 1 nm in depth at the highest fluence. Corresponding to a relative depth of about 4 %, no big influence on the temperature is obvious.

Overall, the graph shows that a prediction of the center temperature via simulation, excluding the ablation process or other energy loss, is in average overrating the experimental result by 33 K.

To look further into the ablation behavior, the hole depth for different laser fluences was measured (figure 3.22). Here again, the film thickness has an important influence. While the thinnest film shows even at the highest fluences only hole depths of several nanometer, for the thickest film about 1 µm of material is ablated. Not only the magnitude, but also the slope depends on film thickness. For thin films, the increase of hole depth versus fluence is less than for thicker films. Concerning the higher temperatures reached in figure 3.21, this can be expected. The higher absorption and the better thermal insulating behavior of thicker films play an important role again in this matter.

3.2.4 Ablation threshold

Figure 3.23 (a) shows the fluence threshold, for which ablation starts to occur. Fluences above which ablation could be observed and below which the polymer film remained unchanged are plotted. The threshold fluence is decreasing with increasing film thickness. This dependence can be explained with the increased absorption and the increased heat insulation of thick films due to the lower heat conductivity of the polymer ($\approx$ 0.15 W/(m K)) as compared to the glass substrate ($\approx$ 1 W/(m K)). As a result, thick films reach a higher temperature at lower fluence.

In figure 3.23 (b), the corresponding threshold temperature measured for 14 µs delay time is plotted versus film thickness. Being close to the end of the 15 µs laser pulse, this temperature is typically giving values close to the peak temperature reached (compare figure 3.18). Within the error, the threshold temperature was constant. The highest temperature without damage can be found at 406 $\pm$ 20 K for a film thickness of 266 nm, the lowest temperature with an ablation hole at 423 $\pm$ 23 K for 793 nm. This temperature is below the decomposition temperature of polystyrene at quasi-equilibrium heating rates (546 K) [52].

To look closer, one point in figure 3.23 is of special interest. For the 1930 nm film at a fluence of about 0.17 J/cm^2, instead of the typical ablation hole (figure 3.24 (a)), a peak can be found in the middle of the hole (figure 3.24 (b)). This shape indicates that the surface was only expanding and shrinking upon heating. The temperature for this point

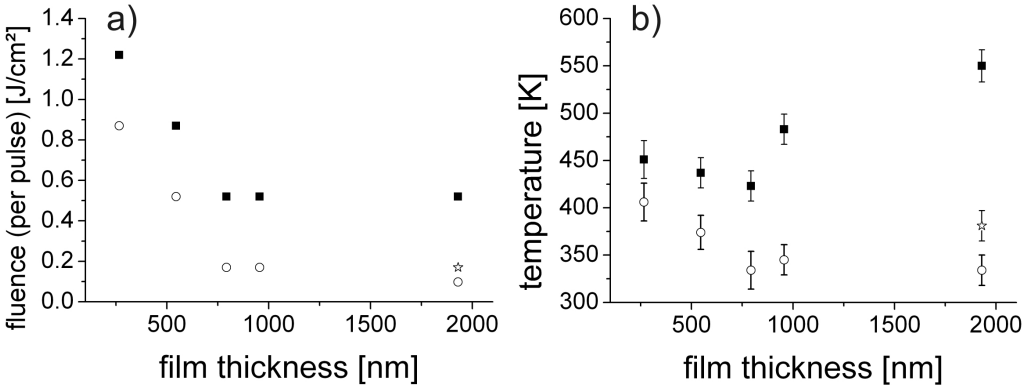

Figure 3.23: Laser fluence vs. film thickness (a) - above ablation threshold (squares), below threshold (circles) and with surface deformation (star). Corresponding center temperatures (b) (averaged over 1.3×1.3 µm^2), delay time of 14 µs, 1 µs integration time, 15 µs laser pulse.

is 381 ± 16 K, which is, within the error, the glass transition temperature of polystyrene [52]. The discrepancy between the temperature found here and the 406 ± 20 K found for the 266 nm film can be explained by the chosen delay time of 14 µs. By simulations, it can be shown that for the thin film this temperature is practically the peak temperature. For the thick film the peak temperature is reached at 17 µs delay time and about 20 K higher than the temperature at 14 µs delay time. So within experimental error the same peak temperature was reached. But for the thick film cooling down is a lot slower because of the thicker insulating polymer layer. This can explain why surface deformation is found for the thick film, but no change for the thin film. Most important, it supports the hypothesis of an ablation temperature just above glass transition.

Based on the surface profiles, the loss in volume for the ablation holes can also be calculated. Especially regarding the rim surrounding the holes (figure 3.17 and 3.24) the result is not trivial. Slightly above threshold, a volume loss of 0.025 ± 0.008 µm^3 was found (holes similar to figure 3.24 (a)), where the average rim volume was about 2/3 of the volume of the hole. For the case of figure 3.24 (b), also a small loss in volume was observed. In average, the volume was reduced by 0.014 ± 0.006 µm^3. This indicates that

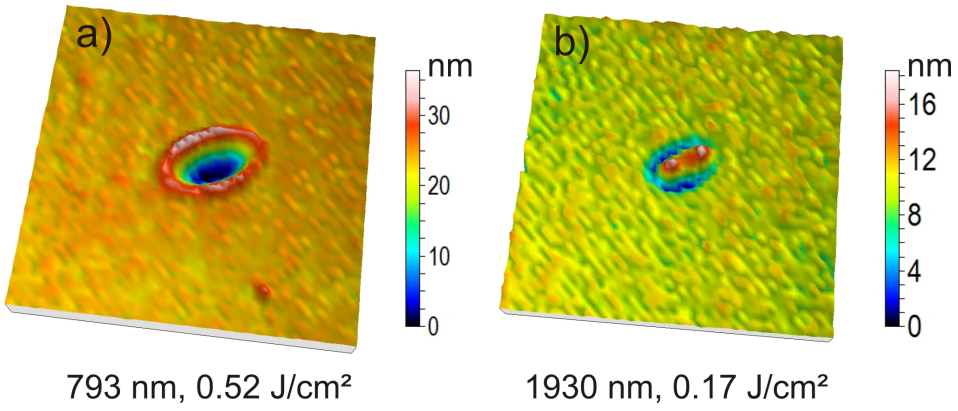

Figure 3.24: White light confocal profilometry 3D images of a typical hole after laser ablation slightly above threshold (a) and surface deformation by laser irradiation (b); 15 µs laser pulse, film thickness and fluence are given in the images. Each image shows 15 × 15 µm^2.

the shrinking after the expansion leads to a slightly changed density of the polystyrene. How much of the volume reduction in figure 3.24 (a) is lost to the gas phase is therefore questionable. However, some material is ablated otherwise the formation of the hole could not be explained.

The result leads to the following conclusion about the ablation mechanism at the threshold temperature: Polystyrene below its glass transition temperature is a rigid material with a tensile strength of about 40-50 MPa [52]. Local heating with the applied order of 10^7 K/s is accompanied by local thermal expansion. Since the material is confined, it cannot expand locally. A stress is built up. The glassy polymer withstands the stress cause of its rather high tensile strength. After the glass transition temperature is exceeded, the polystyrene gets softer. This enables the polymer to flow and expand normal to the surface. This was already shown in literature for laser heating of PMMA or PS by nanosecond time-resolved interferometry [25, 70]. Additionally, the volume expansion gets more pronounced across the glass transition [71]. The stress leads to the surface deformation (figure 3.24 (b)) or, if a critical stress is reached, to ablation (figure 3.24 (a)). This effect is called photomechanical or stress-assisted ablation. It is already

well known in literature [1, 11, 12]. Its application on a polymer with microsecond pulse duration and at the glass transition was, to my knowledge, not reported yet.

In consequence, polymer ablation according to this mechanism is more pronounced for polymers with high glass transition temperature or large volume expansion. If there is no substantial stress built up in the system due to thermal expansion, ablation will only occur when the temperature is high enough to generate thermal degradation or spinodal decomposition. This is an important conclusion for laser heating processes depending on, if ablation is desired or an unwanted secondary process, as it is for example for laser induced film formation.

3.2.5 Influence of molecular weight

The molecular weight is an important parameter for polymers. The glass transition temperature is molecular weight dependent, as well as the mechanical properties above glass transition. With the results from the previous chapter, an influence of molecular weight on the ablation behavior was expected. In order to investigate the influence, polystyrenes with different molecular weights were synthesized and applied in laser heating experiments. Three different molecular weights were chosen (table 3.2). A polymer with low molecular weight with a glass transition of 348 K and two polymers with high molecular weight and glass transition temperatures of 366 and 371 K. The first, the 4 kDa polystyrene, was expected to show a difference in ablation behavior while the latter, the 167 and 337 kDa, should not differ significantly. A difference of 5 K lies well inside the error for the pyrometry temperature measurement, i.e. cannot be resolved. The mechanical properties also resemble each other. They were however chosen to exclude that there are other influences of the molecular weight to the ablation behavior.

The film formation via blade coating depends on molecular weight, too. The coating parameters were adapted accordingly, so comparable polymer films were obtained. Two of the films, the film with lowest and highest molecular weight correspond in polymer-dye ratio (absorption per film thickness). The film thickness is different by 20 %. The third film with intermediate molecular weight is the thickest but absorbs least. The differences

M_w [g/mol]	T_g [K]	film thickness [nm]	α	α/d [1/m]
4380	348	1555	0.0679	43700
167000	366	2045	0.0558	27300
337000	371	1930	0.0895	46400

Table 3.2: Molecular weight, glass transition temperature (T_g, DSC, midpoint DIN), absorption (α) and absorption per film thickness (α/d) of thin polymer films incl. dye 1 (QDIBr).

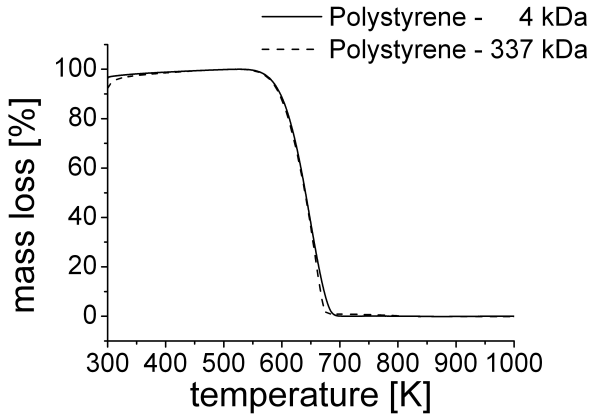

Figure 3.25: Thermogravimetric analysis of polystyrene of different molecular weight; heating rate 10 K/min in air (1 kDa = 1000 g/mol).

in absorption and insulation behavior caused by the difference in film thickness are significant and have to be considered for the interpretation.

When the two samples with lowest and highest molecular weight were compared in a thermogravimetric experiment, they did not differ within experimental error (figure 3.25). The thermal degradation on low heating rates (10 K/min) is typical a chain scission and depolymerization reaction with following evaporation and further degradation of styrene to carbon dioxide, water, benzene, toluene and other molecules in small amounts [15]. A polymer weight dependence was therefore not expected in accordance to the experiment. Additionally, any influence of synthesis for the different molecular weights can be ruled out.

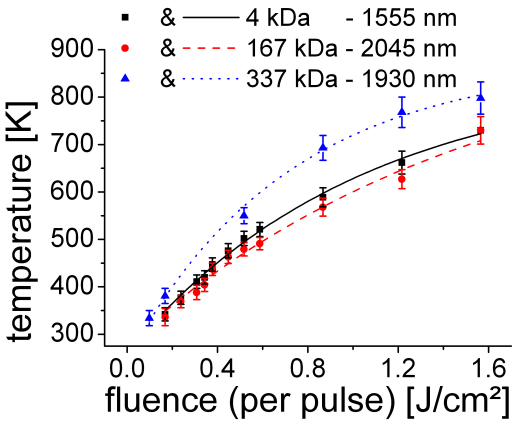

Figure 3.26: Center temperature (averaged over 1.3 × 1.3 µm^2) vs. laser fluence for polystyrene films of different molecular weights presented in table 3.2. The lines are a guide for the eye. Other parameters: delay time of 14 µs, 1 µs integration time, 15 µs laser pulse.

Ablation behavior

In order to analyze the laser ablation behavior of the different molecular weight films, a set of laser fluences were applied. Figure 3.26 shows the center temperature at constant delay time for the laser heating experiments. In the curves, the differences in film thickness and hence in absorption and insulation behavior are apparent. The best absorbing high molecular weight film reached highest temperatures at equal fluence (results were already shown in figure 3.21). The other two films were heated to about equal temperature for constant fluence. The medium molecular weight shows only slightly lower temperatures. Here, the two effects of less absorption and better insulation due to higher film thickness cancel each other out.

The small steps of fluence applied in figure 3.26 allow a study of the different states of ablation around the threshold fluence. In figure 3.27 and 3.28 surface profiles including line scans are presented. Both films show first a surface deformation, like it was found already in chapter 3.2.4, before ablation occurs. Here, even the transition from a peak like shape to holes for higher fluences is visible. Especially for the low molecular weight, this can be followed within four to five images. First, the peak broadens (0.31 J/cm^2).

Then the top is ablated (0.34 J/cm^2) and afterwards more and more of the peak, leading to the holes at higher fluences. For the higher molecular weight film (167 kDa, figure 3.28) the transition took place within the lowest three fluences, with a peak, then a peak with missing top part and finally a hole at fluences higher than 0.34 J/cm^2.

Furthermore, the low and high molecular weight samples did not differ qualitatively. The general topography was similar. However, the height and size of the peak at lowest fluence is more pronounced for the low molecular weight (4 kDa). A height of 41 nm was found in contrast to 17 nm for the high molecular weight (167 kDa). At higher fluences, the rims surrounding the peaks and the holes were more pronounced for the low molecular weight. This can be shown e.g. for a fluence of 0.34 J/cm^2. The spot size including the rim is about 1 µm bigger along the long axis for the 4 kDa polymer film than for the 167 kDa film. Whereas within experimental error the same center temperature was found for both, 4 and 167 kDa, at constant fluence (figure 3.26). Also the influence of the difference in film thickness by about 25 % can be excluded via finite element simulations. The FWHM (full width half maximum) of the temperature distribution along the long axis differs less than 0.1 µm (simulation with 0.23 µJ, corresponding 0.34 J/cm^2, comparison at delay time of 14 µs). The more pronounced rim size must therefore be due to the difference in molecular weight.

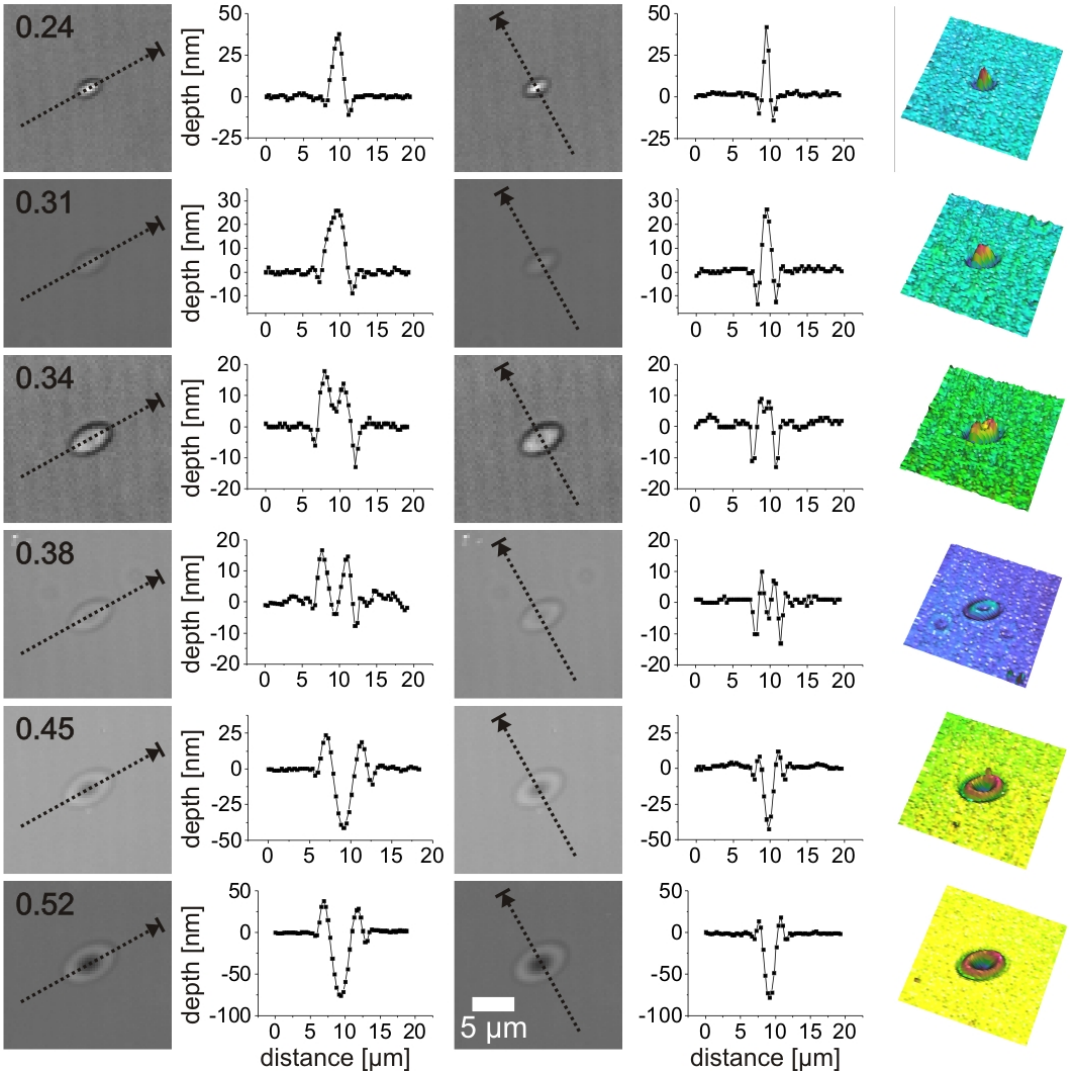

Figure 3.27: Surface profiles images of laser spots at different fluences (in J/cm^2) including line scans for long and short axis and 3D profiles (acquired with white light confocal profilometry). 15 µs laser pulse, molecular weight 4 kDa, film thickness 1555 nm, fluences are given in the images. Each image shows 20 × 20 µm^2.

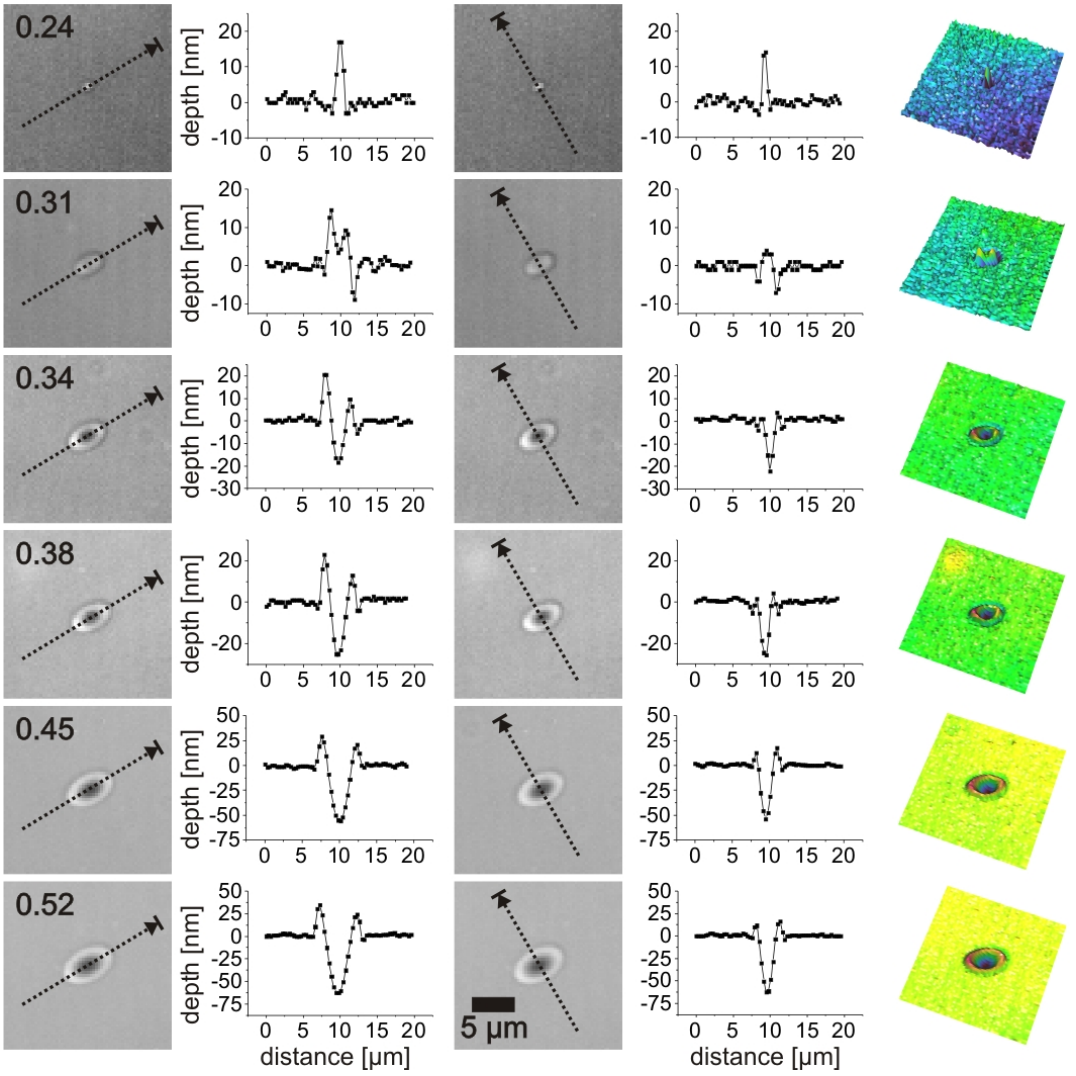

Figure 3.28: Surface profiles images of laser spots at different fluences (in J/cm^2) including line scans for long and short axis and 3D profiles (acquired with white light confocal profilometry). 15 µs laser pulse, molecular weight 167 kDa, film thickness 2045 nm, fluences are given in the images. Each image shows 20×20 µm^2.

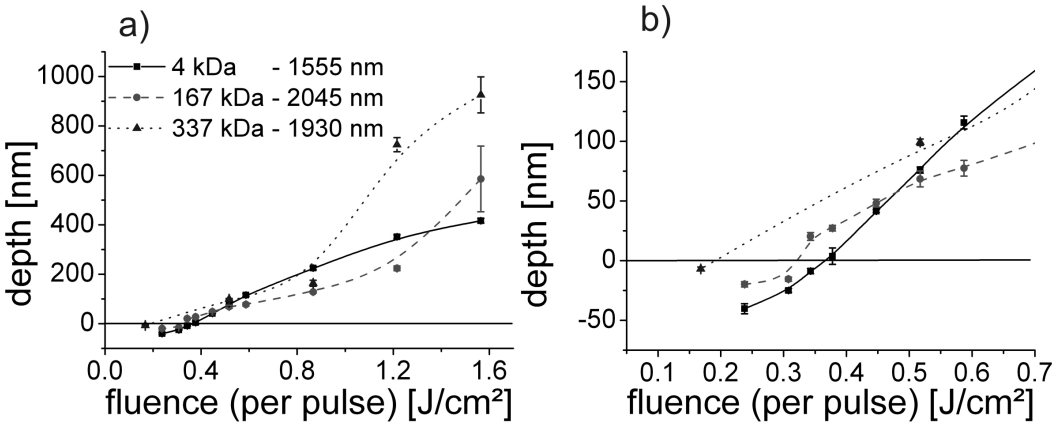

Figure 3.29: Ablation depth vs. laser fluence for different molecular weights (depth at the center of the spot). (a) is giving an overview while (b) shows the graph for small ablation depths. The lines are a guide for the eye. Other parameters: 15 µs laser pulse.

The depth versus fluence for all three molecular weights is shown in figure 3.29. The depth or height at the center is plotted. Therefore, "negative" depths, which are actually peak heights are resulting for low fluences. An influence of molecular weight is apparent. For high molecular weights, a first small increase in hole depth with fluence is followed by a larger increase for high fluences. Whereas the low molecular weight film shows a slow increase over the whole fluence range. Furthermore, as could already be seen in figure 3.27 and 3.28, the formation of a peak into the polymer film at low fluences is more pronounced for lower molecular weight. From an average 40 $\pm$ 4 nm it goes down to 20 $\pm$ 2 nm and finally to 7 $\pm$ 2 nm for the highest molecular weight. Although the significance of the last value is only marginal, being the only point for this molecular weight in the low fluence range.

To explain the different behavior, the molecular weight dependent properties need to be regarded. According to the results in the previous chapter, the hindered local expansion below glass transition and the change in mechanical properties at glass transition lead to the deformation and ablation at threshold fluence. In the experiment, larger deformation peaks were found for the low molecular weight. The stresses due to the

hindered expansion below glass transition should be smaller because of the lower glass transition temperature. The larger peak hight can however be explained with the lower viscosity of the low molecular weight polystyrene above glass transition [72, 73]. The peak increased in size for the next fluence step (figure 3.27, 0.31 J/cm^2) before the top was ablated (0.34 J/cm^2), in contrast to an ablation of the top at 0.31 J/cm^2 for the 167 kDa polystyrene (figure 3.28). This can be addressed to both, the lower viscosity and the lower stresses which were built up below glass transition for low molecular weight. The additional energy in the polymer film was dissipated into deformation, while for the 167 kDa polymer the critical stress for ablation was already exceeded.

For slightly higher fluences holes were formed with a slow increase in depth with fluence, more or less independent of molecular weight. The lower stress for the 4 kDa polystyrene might be canceled out by the lower energy which is necessary to remove material from the surface due to the lower viscosity. Therefore, similar hole depth are found in this range.

In the high fluence range, the ablation mechanism is dominated by a thermal decomposition reaction, as shown in chapter 3.2.2. While the thermal decomposition takes place in the center, a relatively large volume of the polymer is heated above glass transition. For the high molecular weight polymers, these holes are maintained after cooling down due to the high viscosity and the short time the material is heated above glass transition. For the low molecular weight, the polymer possesses the ability to fill parts of the hole from sidewards before cooling down. Therefore, a constant slow increase was found for the low molecular weight in contrast to the fast increase for the high molecular weight. The difference between the 167 and 337 kDa for high fluences was most probably due to the difference in polymer-dye ratio for both films.

The increased rim size for the low molecular weight can be explained by the lower glass transition. The temperature profile found in the temperature measurements at ablation threshold resemble, in agreement with the simulations, a Gaussian distribution. The polymer further outside from the spot may deform for the low molecular weight being above glass transition while it is still below glass transition for the high molecular weight.

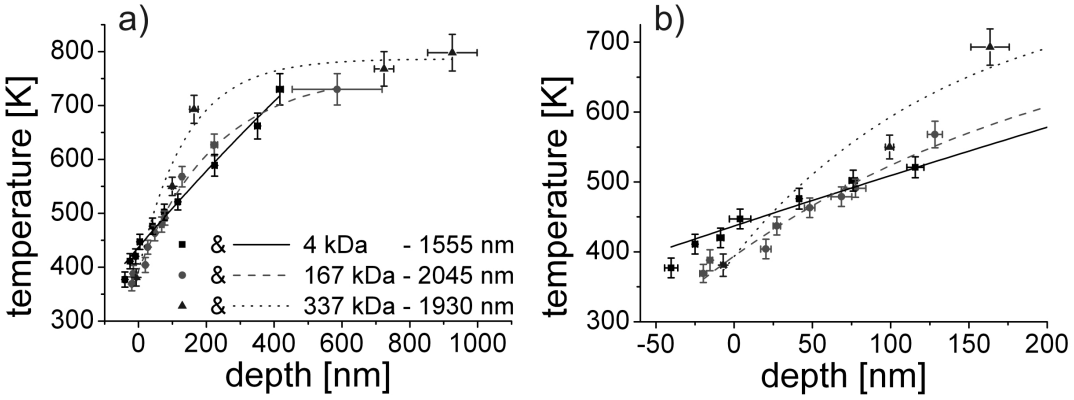

Figure 3.30: Center temperature vs. ablation depth for polymer films of different molecular weights. (a) is giving an overview and (b) a magnification at threshold; temperature at center area of 1.3 × 1.3 µm^2, delay time of 14 µs, 1 µs integration time, 15 µs laser pulse.

If the temperature is plotted versus depth (figure 3.30), a behavior for the different molecular weights is also apparent. Both high molecular weight samples show similar dependence. A fast increase in temperature for small hole depths and a saturation at around 700 to 800 K for deep holes. An almost linear behavior is found for the low molecular weight. Although this curve is also expected to level off at some point out of the fluence range of the laser, reaching a comparable saturation temperature of 700 to 800 K.

The explanation corresponds to the one above. In the low temperature regime, a difference in surface deformation for the same temperature was found before ablation, but a similar behavior for slightly higher temperatures. The range in which the temperature levels off for the high molecular weight matches the faster increase in depth with fluence. Thermal decomposition took place at this temperature for all molecular weights. However, the holes were filled partially for the low molecular weight while they remained for the high molecular weights.

M_w [g/mol]	T_g [K]	$T_{no\ change}$ [K]	$T_{deformation}$ [K]	$T_{threshold}$ [K]
4380	348	356	391	434
167000	366	352	385	402
337000	371	357	402	-

Table 3.3: Characteristic temperature for polystyrene ablation around threshold for different molecular weights. Glass transition temperature T_g (DSC, midpoint DIN), temperature with no change after laser pulse $T_{no\ change}$, temperature for first surface deformation $T_{deformation}$ and ablation threshold temperature $T_{threshold}$.

Ablation threshold

The temperature around the ablation threshold can be determined by figure 3.30 (b). The ablation threshold temperature is defined as the lowest temperature with a removal of material. This corresponds to the measured temperature for the peaks with a missing top in the surface profiles (in figure 3.27 at fluence 0.34 J/cm^2 and in 3.28 at fluence 0.31 J/cm^2). The resulting temperatures are however the measured temperatures at a delay time of 14 µs. In order to compare the different film thicknesses quantitatively, these temperatures need to be adapted according to their film thickness. Therefore, the maximum temperatures for the different film thicknesses were calculated based on finite element simulations analogue to chapter 3.2.4. The results are given in table 3.3. For the highest molecular weight only the data for the 1930 nm film was included. As already discussed in chapter 3.2.4, the assumption of comparing only the maximum temperature is not applicable for film thicknesses in the range of 266 nm up to 1930 nm. An ablation threshold temperature for the 1930 nm film could not be determined. The steps in fluence applied in this case were too large. It can however be estimated from figure 3.30 (b) to be in the same range as the ablation threshold temperature for 167 kDa.

The temperatures in table 3.3 do not show a strong dependence on molecular weight.

Especially, if it is considered, that the 167 kDa polymer does not differ significantly from the 337 kDa. The glass transition temperatures for both polymers lie well within the error of the temperature measurement and the mechanical properties are similar.

The only significant difference between the molecular weight samples is the higher ablation threshold temperature for the lowest molecular weight. An increase of 32 K was found. A difference for the 4 kDa polymer was already identified in the ablation behavior, i.e. in the analysis of the surface profiles. The lower viscosity of the low molecular weight above glass transition and the lower stress due to the lower glass transition temperature were responsible for more extended surface deformation. More laser energy could be dissipated by mechanical deformation of the polymer film. Thus, a critical stress necessary for ablation was built up for higher fluences and a higher ablation threshold temperature resulted due to the lower stresses and the ability to dissipate more energy into deformation.

For thinner low molecular weight films, an analogue raise in temperature of about 30-40 K can be expected. In comparison to the ablation threshold temperature found in chapter 3.2.4, a temperature of 450-60 K can be derived. A similar shift in ablation threshold temperature can also be expected for other low molecular weights. However, a more detailed study would be necessary in order to identify the quantitative dependence of the threshold temperature on molecular weight.

The temperature for first surface deformation was found to be independent of molecular weight (table 3.3). An average maximum temperature of 393 K results. A temperature which is above the glass transition temperature of the thermogravimetric experiments for all molecular weights. The lack of molecular weight dependence can have two explanations. The first is that the difference in glass transition temperature between low and high molecular weights is smaller for the high heating rates than it is in a DSC measurement. An experimental proof might be possible if rheology measurements would be conducted. Via the time-temperature-superposition procedure the glass transition or softening temperature of the material can be deduced in a wide frequency range. In this way, reasonable insight could be achieved for the 100 kHz regime, the interesting

regime for laser pulse duration of 15 µs. However, a second explanation for the lack of molecular weight dependence can also be found in the big error of the temperature measurement in the interesting temperature range of 350 to 400 K. This is definitely the lower detection limit. With error bars of about ± 15 K, resolving a difference in glass transition temperature of 18 respectively 23 K is difficult. Other polymers with a more pronounced dependence of glass transition temperature on molecular weight or higher glass transition temperatures would therefore be favorable.

3.2.6 Influence of dye concentration

The absorption of the polymer film is, besides the film thickness, one of the most important factors for the ablation behavior. Therefore, films with different dye-polymer ratio or dye concentration were prepared and illuminated at constant laser fluence. The film thickness was kept constant at about 2 µm. Figure 3.31 shows the resulting center temperature for the different samples. After a first linear increase the temperature levels off at about 800-900 K. A similar behavior was observed when plotting the center temperature versus fluence (figure 3.21 and 3.26). Only, the range regarded here is bigger than it was for the other two figures. There, some of the curves, especially in figure 3.21, showed exclusively the linear dependence found here for low concentrations. The analogy is simple to explain. Whether higher laser fluence or dye concentration are used, the result is analogous. More energy is available in the polymer film and converted into heat leading to higher temperatures.

With the temperatures acting upon the polymer film in figure 3.31, surface deformation respectively ablation holes are formed in the polymer film. The corresponding surface profiles are presented in figure 3.32. The whole spectrum from surface deformation to deep holes, almost extending through the complete film thickness are obtained. The first three images can be well compared to the images in chapter 3.2.5, dealing with the molecular weight dependence. The surface deformation is more pronounced here, with an average of 31 ± 1 nm, even though a polymer of high molecular weight polystyrene is used (337 kDa). However, the angle of incident is different between the

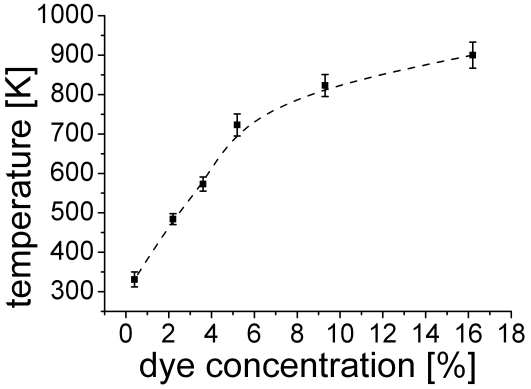

Figure 3.31: Center temperature vs. dye concentration (in relation to the polymer) for different polystyrene films. The film thickness is about 2 µm. Temperature at center area of 1.3 × 1.3 µm^2, delay time of 14 µs, 1 µs integration time, 15 µs laser pulse with a fluence of 1.09 J/cm^2.

two experiments. Here 67° was used instead of the typical 56°. This leads to a change in beam dimension of 17.7 × 6.9 instead of 12.3 × 6.9 µm^2 and hence to the difference in the affected area and in peak height. For higher concentrations, first the typical hole formation is observed. With increasing dye concentration, a transition from shallow to deep holes is apparent from 3.6 to 5.2 % of dye. From then on, the holes extent further in size and depth. The distortion of the holes along the long axis is due to the angle of incident. The effect is really prominent for the film with highest dye concentration, but already visible for a dye concentration above 5.2 %.

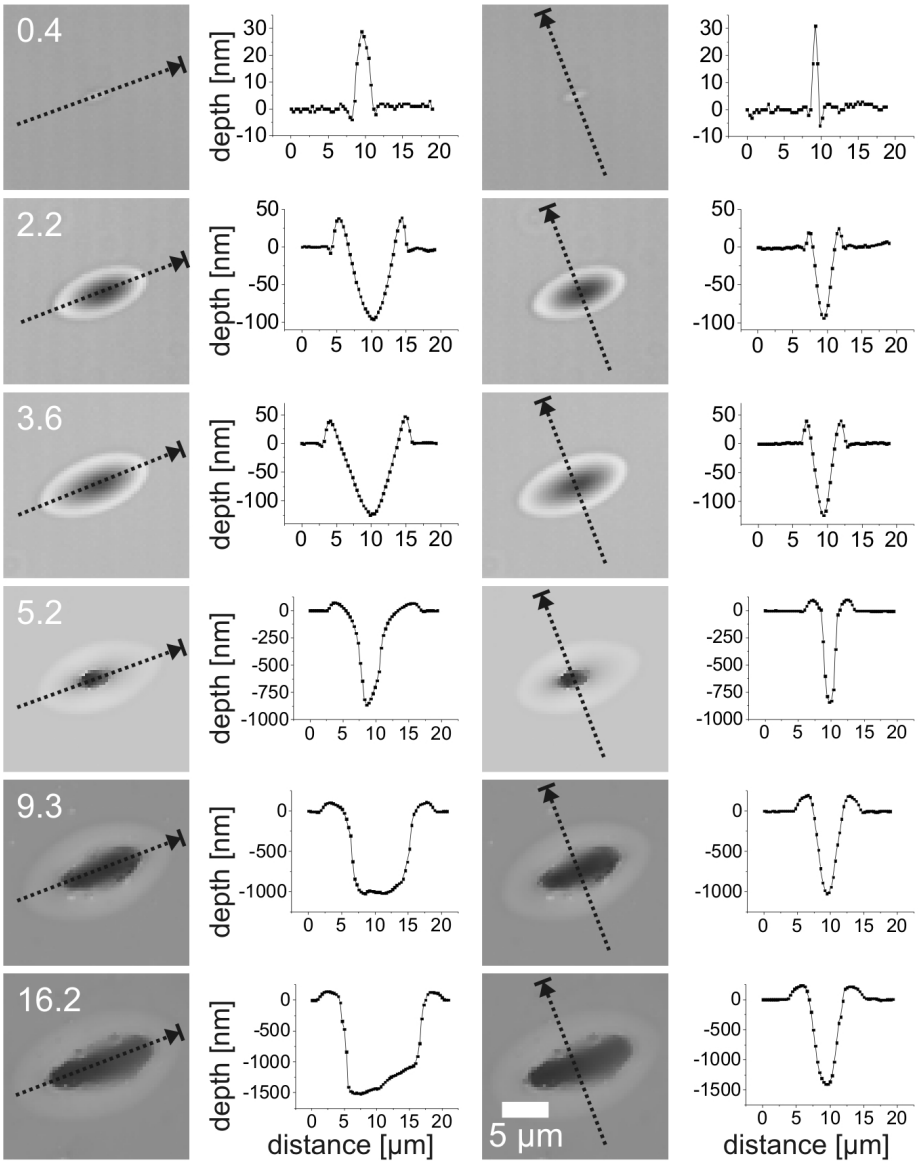

Figure 3.32: Surface profiles images of laser spots for different dye concentrations (in %) including line scans for long and short axis (acquired with white light confocal profilometry); dye concentrations are given in the images. Each image shows 20 × 20 µm^2. Experimental parameters see figure 3.31.

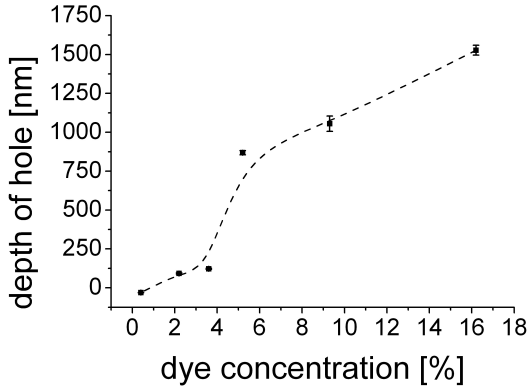

Figure 3.33: Ablation depth vs. dye concentration for different polystyrene films. Experimental parameters see figure 3.31.

The trend of increasing hole depth is plotted in figure 3.33. In the graph, one can follow the first small increase in hole depth and then the relatively fast transition from shallow to deep holes. This graph can also be compared to previous graphs, showing depth versus fluence instead of dye concentration (for example figure 3.22). In analogy to figure 3.31, the previous presented graphs were only showing the dependence for the first three to four points. The thickest film in figure 3.22 (film thickness dependence) for example showed the curve up to the fast increase. For the 956 nm film a steep increase can be seen for the highest fluence, but the rest of the films stay with the applied fluence range in the first linear regime. Overall an increase in hole depth for higher dye concentrations was expected. The steep increase at a certain dye concentration is however not explainable solely with figure 3.33.

The inflection point of the depth-versus-dye concentration curve (figure 3.33) lies in the same region as the change in slope for the temperature-versus-dye concentration curve (figure 3.31). Therefore the center temperature for the holes were plotted versus the ablation hole depth (figure 3.34). Here again, a change in slope is obvious between 3.6 and 5.2 % dye concentration (the third and the fourth point from left). And the change in slope is even more pronounced. It could already be shown in chapter 3.2.2 that the ablation mechanism or the dominating process of ablation is different at threshold

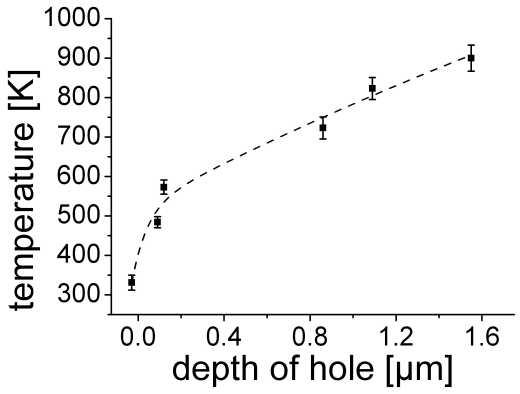

Figure 3.34: Center temperature vs. ablation depth for polystyrene films of different dye concentration. Experimental parameters see figure 3.31.

and well above threshold with the two examples of the thin (266 nm) and thick (956 nm) PS film. Here, the transition of the dominating effect between both, a photomechanical or stress-assisted ablation and a photothermally induced decomposition reaction can be seen. The first three points with lower dye concentration are dominated by the stress-assisted ablation, the last three by the thermal decomposition. The temperature dependence is reflecting the difference in energy consumption of both processes. In stress-assisted ablation, the energy is converted to kinetic energy. If a thermal decomposition reaction is occuring the energy is used to break chemical bonds. A process consuming typically much more energy. At higher temperatures, there might still be stress-assisted ablation, but the thermal decomposition is the major process.

When fitting the first and the last three points in figure 3.35 with straight lines, the two lines cross at a temperature of 745 K (at a dye concentration of 5.7 %). This corresponds well with findings in chapter 3.2.1 and 3.2.2. It designates a temperature to the transition of a stress-assisted ablation to photothermal degradation for polystyrene at 1 µs time scale.

In summary, with a series of polymer films of different dye concentration it could be shown, that increasing the dye concentration has a similar effect than increasing the fluence. A transition from stress-assisted dominated ablation to ablation dominated by

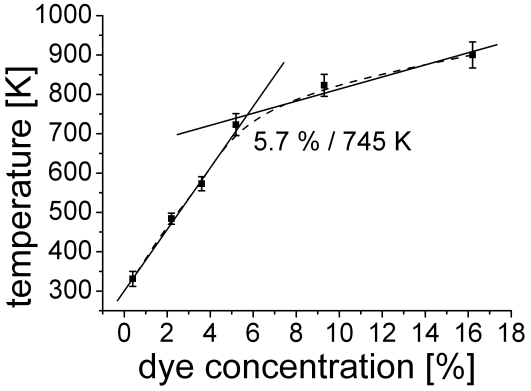

Figure 3.35: Center temperature vs. dye concentration (in relation to the polymer) for different polystyrene films analogue to figure 3.31 with two lines to illustrate the difference in slope and the transition in temperature dependence.

thermal degradation is apparent at around 750 K.

3.2.7 Ablation with different dyes

In chapter 3.1.2, experiments were already presented with polymer films doped with different dyes. Here, the influence on the ablation behavior of the different dyes is discussed. The 2D temperature graphs are presented in figure 3.36. Even though equal film thickness and dye concentration was used, dye 2 and dye 3 lead to a higher temperature. The absorption of these two dyes is higher at the laser wavelength, as already shown in the absorption spectra in figure 3.8. The higher temperature is consequently due to this fact. Apart, the 2D temperature graph of the three different dyes resemble each other. A crescent-shaped area is visible, more pronounced for dye 2 but also visible for dye 3 analogue to the time dependent study for dye 1 shown in figure 3.15 (b). Thermal degradation should occur at the temperatures reached here. The typical pattern of uneven temperature distribution in the corona is apparent.

The corresponding center temperatures are given in table 3.4. Even though dye 2 (QDI) has the highest absorption at the laser wavelength, the highest temperature is achieved with dye 3 (QDIS). This trend is already visible in the 2D temperature graphs

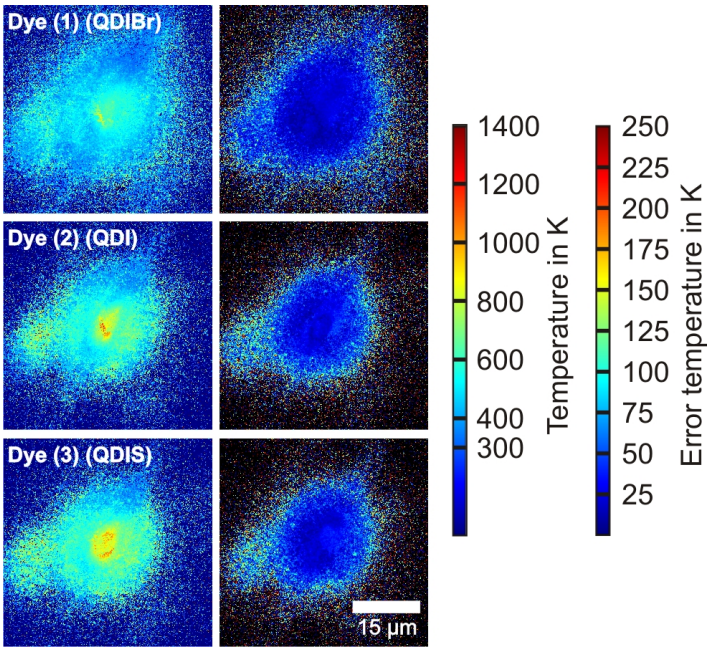

Figure 3.36: 2D temperature and error graphs of PS films including different dyes. Other parameters: 1 µs integration time, 14 µs delay time, 15 µs laser pulse with a fluence of 1.09 J/cm^2, film thickness about 2 µm.

Dye	absorption	center temperature [K]	error [K]
QDIBr	0.077	633	20
QDI	0.274	843	30
QDIS	0.196	879	26

Table 3.4: Center temperature for polystyrene films including different dye.

(figure 3.36). The yellow and orange region for dye 3 is bigger than the one of dye 2, indicating higher temperature.

The simple prediction of highest temperature for highest absorption fails. The polymer film with dye 2 has an absorption of 0.274, while the one with dye 3 shows only 0.196. The highest temperature should therefore be found for the film with dye 2. And the surface profile images 3.37 confirm this result. The hole formed by laser irradiation for dye 2 resembles more the one for 5.2 % in the dye concentration series (figure 3.32), the hole for dye 3 more the one for 9.3 %. Besides this fact, the hole shape are in principle the same already found for dye 1. If the energy input would be adapted, no difference would be expected.

The different behavior of the dyes can be explained with their chemical structures. All of them are based on the quarterylenediimide structure. Only the substitution of the side groups is changed. In figure 3.38 the differences are highlighted in red and blue (always only once, even though four red groups are substituted and two blue ones). In order to be an efficient molecular heater, on the one hand, the dye needs to absorb efficiently, being photo stable and well dispersible in the matrix. As already discussed in the introduction (chapter 1.2.6), quarterrylene dyes possess these properties in general [58]. With the choice of substitutions, the solubility and the photo stability is not altered considerably. The absorption spectra are influenced by the difference in electron donating or withdrawing ability of the side groups on the main aromatic system (figure 3.39). In principle all three spectra show the same characteristic. A shoulder (dye 2 and 3) or even a second peak (dye 1) is visible besides the maximum. A bathochromic shift of the absorption maximum is apparent from dye 1 to dye 3 and dye 2. Dye 1 (maximum

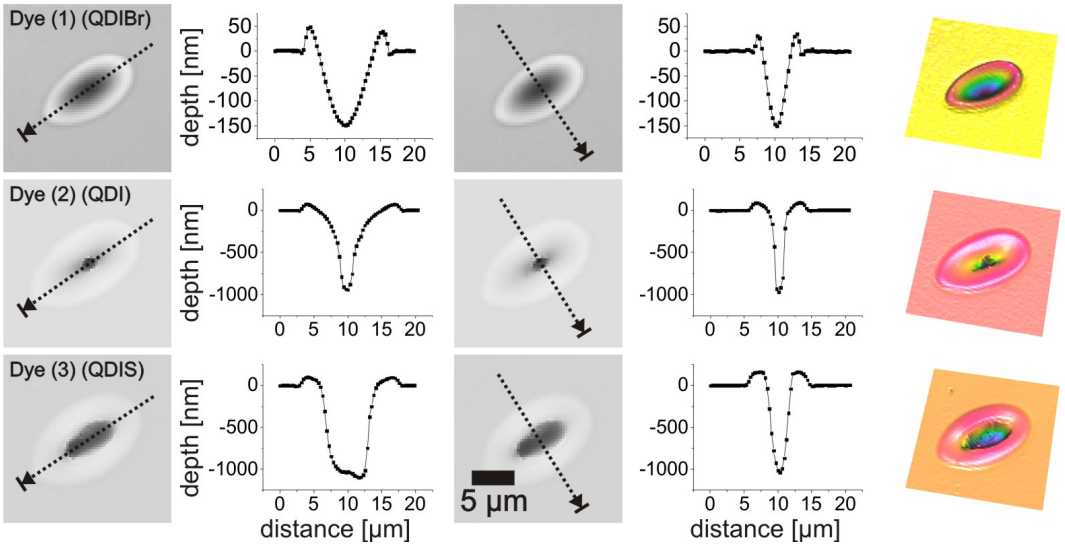

Figure 3.37: Surface profiles images of laser spots for different dyes including line scans for long and short axis (acquired with white light confocal profilometry). Each image shows 20 × 20 µm^2. 15 µs laser pulse with a fluence of 1.09 J/cm^2.

at 750 nm) and dye 3 (maximum at 769 nm) only differ in the aryl side group. The electron donating behavior of the phenoxy group seems comparable to the pyridinethiol group, leading to the small change in the maximum. Whereas if the bromine groups are omitted, as it is the case for dye 2, the maximum shifts more drastically to 804 nm, almost to the laser wavelength.

Dye 2 should be the best heater dye according to the provided arguments. However, the fluorescence of the dye molecules has to be taken into account. Dye 2 is known to show a fluorescence quantum yield of 5 % [59], whereas for the other two, the fluorescence quantum yield drops below the detection limit. In this way the discrepancy of lower absorption but higher temperature and deeper holes for dye 3 can be explained. But in principle all three dyes can be applied for laser heating or laser ablation of polymer films.

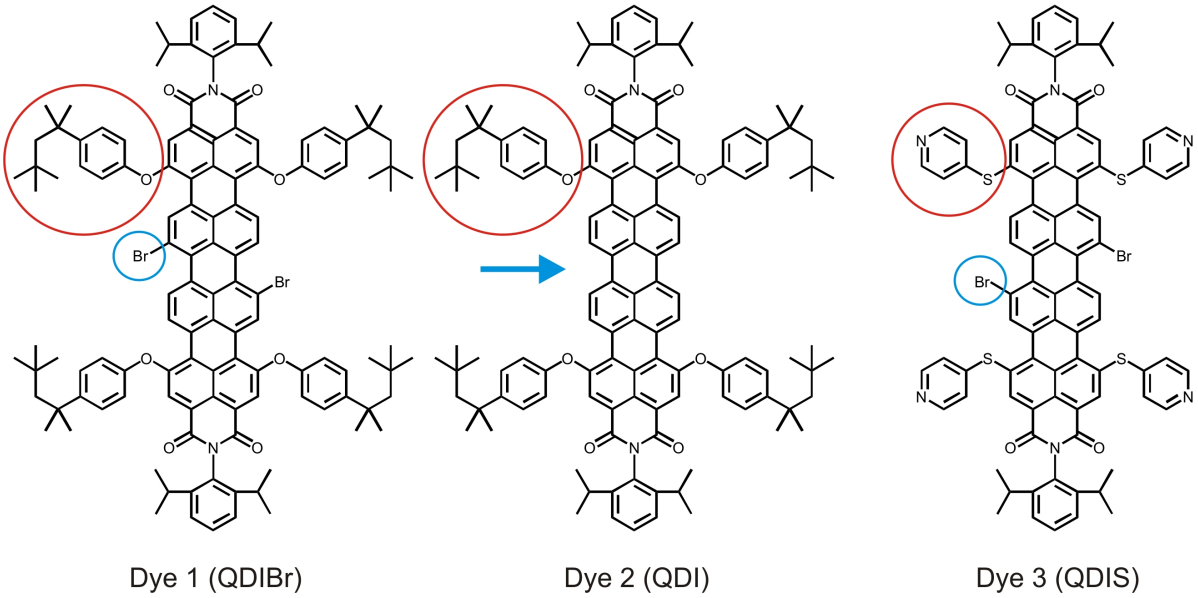

Figure 3.38: Chemical structures of different dyes. The differences in side chains are highlighted in red and blue.

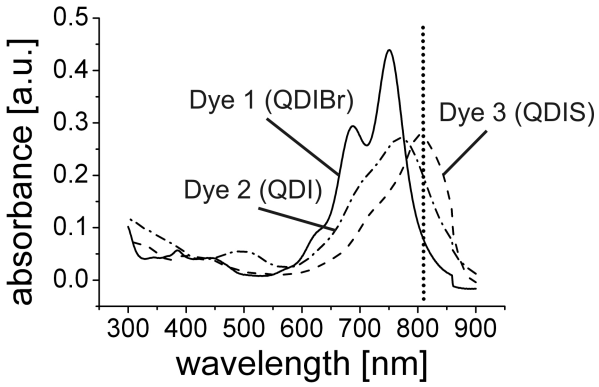

Figure 3.39: Absorption spectra of polystyrene films with different dyes. The dotted line represents the laser wavelength of 810 nm.

3.3 Laser heating of polymers with different thermal behavior

To get a more general view, it is of interest to compare the laser heating behavior of polystyrene to other polymers. The results for polystyrene suggest an influence of the glass transition behavior on the ablation threshold fluence and the thermal stability for fluences well above threshold. In this work poly(α-methylstyrene) was chosen as less stable and a polyimid as more stable polymer. Besides, the polyimid shows no glass transition in the range of room temperature up to the start of degradation while the poly(α-methylstyrene) exhibits a glass transition at 410 K, about 40 K above the glass transition temperature of the used polystyrene.

The stability at low heating rates can be followed in thermogravimetric experiments (figure 3.40). Poly(α-methylstyrene) is decomposing in one step like polystyrene. The small mass loss at the beginning (low temperature) can be addressed either to a measurement artifact or to small monomer or low molecular weight traces. In contrast, for the polyimid, a gradual mass loss of about 35 % is followed by a second sharp step with 65 %. Keeping in mind, that the molecular weight of the polyimid is low (2350 Da) and that the polymer is highly polydisperse (PDI = 3.15), monomer or oligomere fractions might be responsible for this dependence.

In addition, a triazene polymer was analyzed in order to investigate the laser heating behavior of a polymer typically applied in the LIFT technique (chapter 1.2.2). The thermal influence on ablation was already studied for pulse durations in the order of 10 ns [74], allowing comparison to faster time scale behavior. Figure 3.41 shows the thermogravimetric analysis. The first step with a weight loss of 62 % is addressed to the loss of the volatile fractions, nitrogen and the bifunctional secondary amin [75]. A degradation onset temperature of 500 K was obtained, lower than the 546 K of polystyrene or the 530 K for poly(α-methylstyrene), neglecting the first small mass loss. The glass transition temperature of the triazene polymer is at 336 K. This allows furthermore to study the influence of a low glass transition temperature.

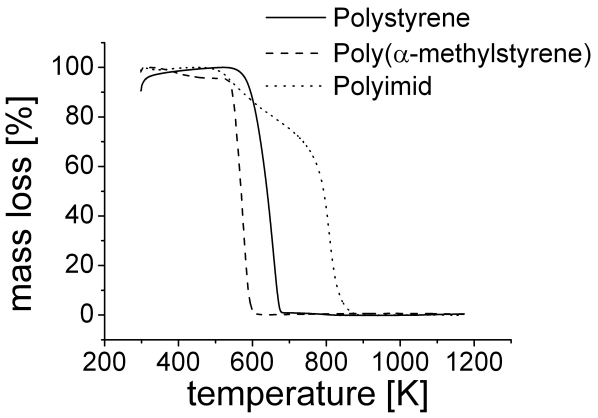

Figure 3.40: Thermogravimetric analysis of different polymers; heating rate 10 K/min in air.

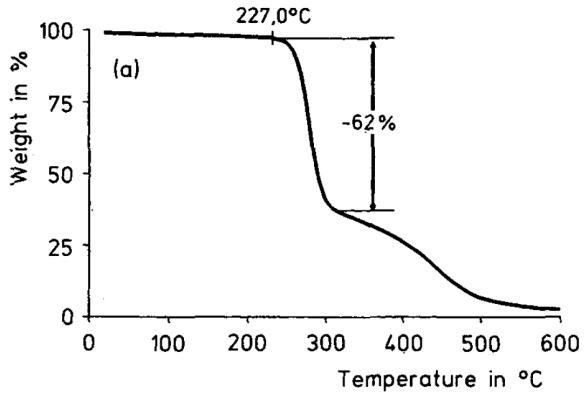

Figure 3.41: Thermogravimetric analysis of triazene polymer [75].

For the poly(α-methylstyrene) a thick film of more than 3 µm was chosen. Analogue to the 1930 nm PS film such a thickness allows the analysis of the threshold behavior and the behavior at high temperatures well above threshold by applying an appropriate fluence. For the polyimid a film of only 79 nm was used. Higher film thicknesses could not easily be obtained due to the low molecular weight. For the triazene polymer a film of 369 nm was chosen. This film thickness lies well within the discussed polystyrene films and enables good comparison. Thicker spin coated films suffer in quality, especially in terms of surface roughness. The properties of the films including two polystyrene films are summarized in table 3.5. The thinnest and the thickest polystyrene film already

Polymer	T_g [K]	film thickness [nm]	α	α/d [1/m]
Poly(α-methylstyrene)	410	3280	0.1900	57800
Polyimid	-	79	0.0822	1.04e6
Triazene polymer	336	369	0.1542	4.18e5
PS (337 kDa) - thick film	371	1930	0.0895	46400
PS (337 kDa) - thin film	371	266	0.0282	1.06e5

Table 3.5: Glass transition temperature (T_g, DSC, midpoint DIN, respectively for the triazene polymer from [75]), absorption (α) and absorption per film thickness (α/d) at the laser wavelenght of different polymer films (incl. dye 1 (QDIBr)) compared in this chapter.

introduced in chapter 3.2 are most comparable.

The absorption at the laser wavelength was adapted to the film thickness by choosing an appropriate concentration of the NIR dye. For the rather thick poly(α-methylstyrene) film, a concentration similar to the one for the 1930 nm polystyrene film was chosen. This is reflected in the small difference in absorption per film thickness which corresponds to the dye concentration in the polymer film. In contrast, a much higher concentration was used for the thin polyimid film. The absorption per thickness was increased by one order of magnitude for the 79 nm polyimid film compared to for the 266 nm polystyrene film. This was necessary in order to assure enough energy absorption to attain temperatures required for ablation of the polyimid. A higher dye concentration was also chosen for the triazene film. In this way, the behavior of the polymer at higher temperatures could be studied.

3.3.1 Poly(α-methylstyrene)

The poly(α-methylstyrene) film was illuminated with the laser at various fluences. The 2D temperature graph for the highest fluence is presented in figure 3.42. A typical temperature distribution was found, analogous to the polystyrene films discussed previously.

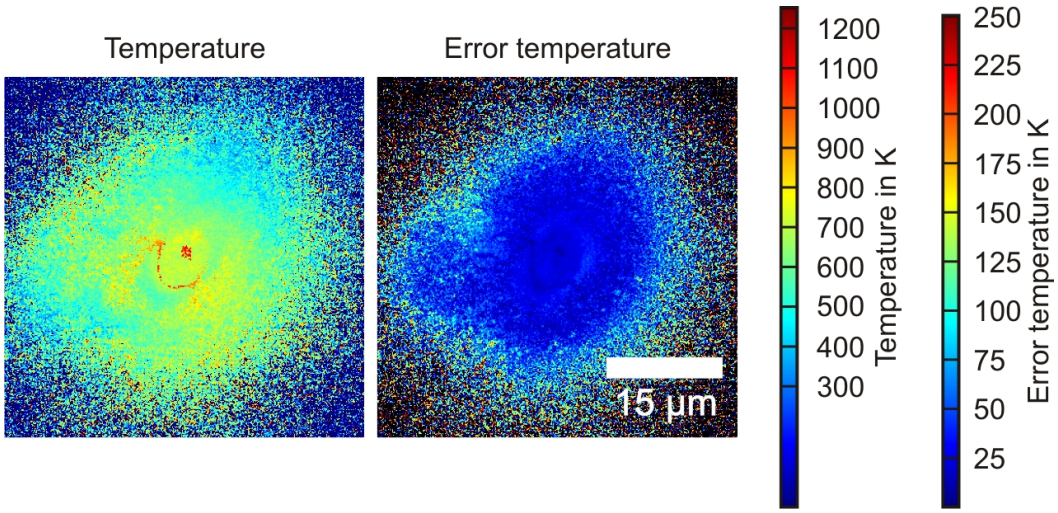

Figure 3.42: 2D temperature graphs of poly(α-methylstyrene) film with 3280 nm thickness. Other parameters: delay time of 14 µs, 1 µs integration time, 15 µs laser pulse, fluence 1.56 J/cm^2.

The crescent-shaped area is even more pronounced and well shaped. A hot spot in the center was also visible. The film thickness of more than 3 µm makes a difference in this matter. Even though material is ablated, the film is still thick enough in the center so the convolution of laser intensity, absorption and insulation effect results in highest temperature in the center.

The dependence of the center temperature on the fluence is plotted in figure 3.43. It is similar to the dependence of the 1930 nm PS film. Regarding the larger film thickness and the higher absorption per film thickness, a higher temperature was expected for the poly(α-methylstyrene) film. However, differences in polymer properties like the thermal conductivity, heat capacity and density can explain the similar behavior, in spite of the thicker insulating polymer layer and the higher energy input in contrast to the 1930 nm polystyrene film.

The holes found in the film after illumination (figure 3.44) can be compared to the ones of polystyrene films showed early. Only the holes around threshold are presented in the plot. The shape of deeper holes are analogous to the ones shown for dye concentration study of polystyrene in chapter 3.2.6, figure 3.32.

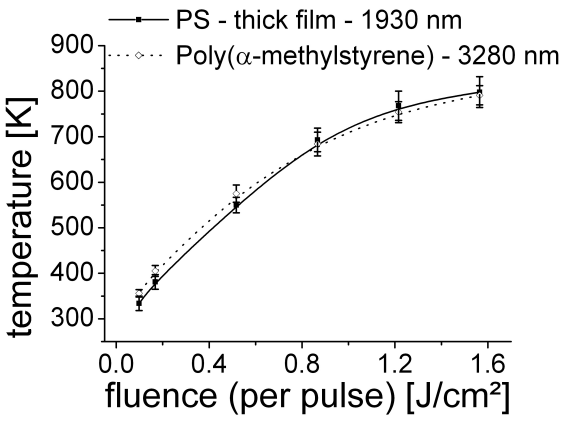

Figure 3.43: Center temperature (averaged over 1.3 × 1.3 µm^2) vs. laser fluence for poly(α-methylstyrene) film and comparable thick PS film. Experimental parameters: delay time of 14 µs, 1 µs integration time, 15 µs laser pulse. The lines are a guide for the eye.

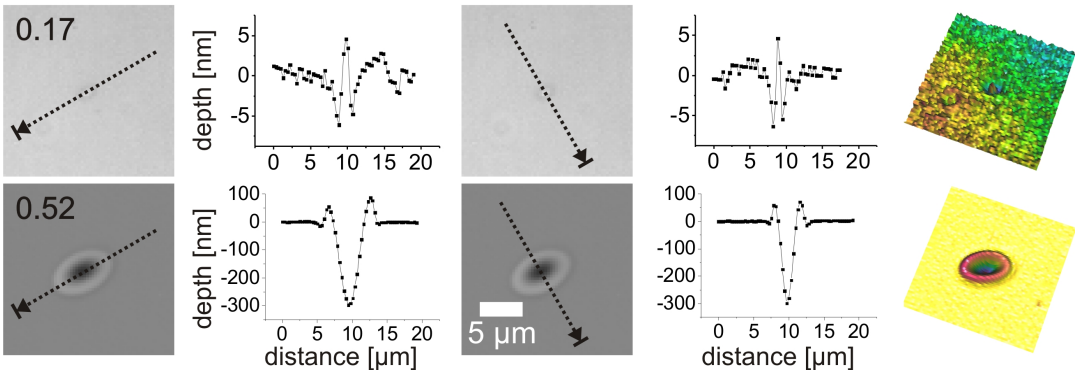

Figure 3.44: Surface profiles images of laser spots of the poly(α-methylstyrene) film at different fluences (in J/cm^2) including line scans for long and short axis and 3D profiles (acquired with white light confocal profilometry) for 15 µs laser pulses. Fluences are given in the images. Each image shows 20 × 20 µm^2.

For the surface deformation showed in figure 3.44 (fluence of 0.17 J/cm^2) a center temperature of 405 ± 12 K was measured for a delay time of 14 µs. Finite element simulations with the assumption of the thermal behavior of polystyrene, i.e. with a PS film with similar properties, film thickness and absorption, suggest a peak temperature which is 30 K higher at a delay time of 18 µs. So a temperature of 435 K results for first surface deformation of poly(α-methylstyrene). For polystyrene a temperature of 393 K was obtained for first surface deformation. This is in good agreement with the difference in glass transition temperature (table 3.5). The poly(α-methylstyrene) showed a glass transition 40 K above the one for polystyrene in a DSC experiment, and also about 40 K in the laser heating experiment. The next step in fluence is too big for further analysis of the threshold temperature. However, the result strongly supports the hypothesis of a stress-assisted ablation for poly(α-methylstyrene) at threshold above glass transition, just like it was found for polystyrene.

The similarity of the 2D temperature graphs shown here (figure 3.42) and for polystyrene (for example figure 3.15 (b)) also suggests an ablation dominated by thermal degradation at higher fluences, well above threshold.

If the ablation depth for higher fluences is regarded (figure 3.45), the difference in thermal stability is obvious. At the same fluence deeper holes can be found for the poly(α-methylstyrene) film compared to the polystyrene film. Although, as was shown for polystyrene films of different film thickness in chapter 3.2.3 (figure 3.22), the influence of film thickness and absorption should not be neglected in this graph.

Therefore, the center temperature is plotted versus depth including polystyrene films of various film thicknesses (figure 3.46). In this plot the different thermal stability of polystyrene in contrast to poly(α-methylstyrene) is obvious. While the data points for polystyrene all fall on the same master curve, deeper holes are found for constant temperature for the poly(α-methylstyrene). The deviations from the master curve for polystyrene can be explained if the applied assumption is considered. The temperature at a delay time of 14 µs is plotted. For thin films, this coincides with the peak temperature, for the thicker films it does not.

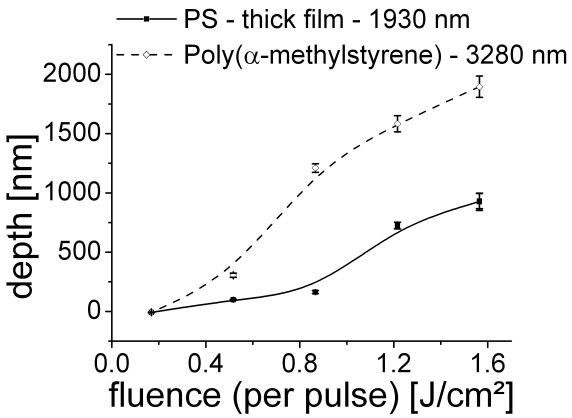

Figure 3.45: Ablation depth vs. laser fluence for poly(α-methylstyrene) film and comparable thick PS film; 15 µs laser pulse. The lines are a guide for the eye.

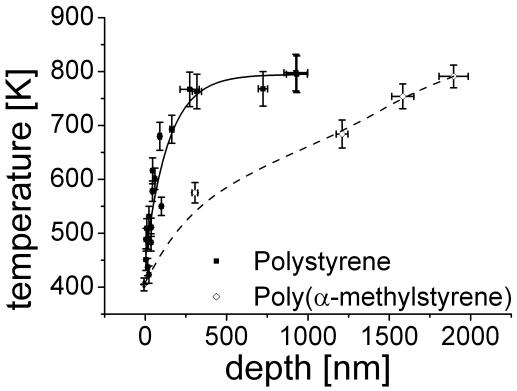

Figure 3.46: Center temperature vs. ablation depth for poly(α-methylstyrene) film and PS films of various film thicknesses; temperature at center area of 1.3 × 1.3 µm^2, delay time of 14 µs, 1 µs integration time, 15 µs laser pulse. The lines are a guide for the eye.

In conclusion, it could be shown, that poly(α-methylstyrene) ablates analogous to polystyrene. Stress-assisted ablation is found at the threshold temperature which is transforming to an ablation dominated by thermal degradation at higher temperatures. The temperature for an onset of the surface deformation is shifted by +40 K compared to polystyrene, just like the glass transition of poly(α-methylstyrene). A threshold temperature for ablation could not be determined, but it can be expected to be shifted equally to higher temperatures. According to the result for polystyrene, an ablation threshold temperature of 460 K results for poly(α-methylstyrene). At higher fluences, the thermally less stable poly(α-methylstyrene) shows more pronounced ablation at equal temperatures, as it would be expected from the lower thermally stability found in the thermogravimetric experiment.

3.3.2 Polyimid

The 2D temperature graph for polyimid (figure 3.47) differed from the previously shown for poly(α-methylstyrene) (figure 3.42). Due to the film thickness, the polyimid film resembles much more the thin polystyrene film in figure 3.15 (a). A differentiation in a hot core area, a corona at lower temperature and a not heated surrounding was observed. A Gaussian shape could be found in line scans along long and short axis (figure 3.48).

The center temperature of 721 ± 25 K was considerably higher than the 509 ± 18 K found for the thin polystyrene film. The size of the most heated core area is more or less maintained with 4 × 5 µm^2, but the corona is reduced in size to 8 × 11 µm^2. The latter can be explained by the small film thickness of only 79 nm. Much more energy can be dissipated in the z direction (perpendicular to the film surface) through the substrate. The dissipation along the x and y direction is therefore limited.

The temperature dependence for various fluences is shown in figure 3.49. In comparison to the 266 nm PS film, a higher temperature was found. This can be expected regarding the high absorption of the polyimid film (table 3.5). The dye-polymer ratio is increased resulting in a higher absorption per film thickness by one order of magnitude in respect to the thin PS film. In that way, even for the low film thickness of 79 nm,

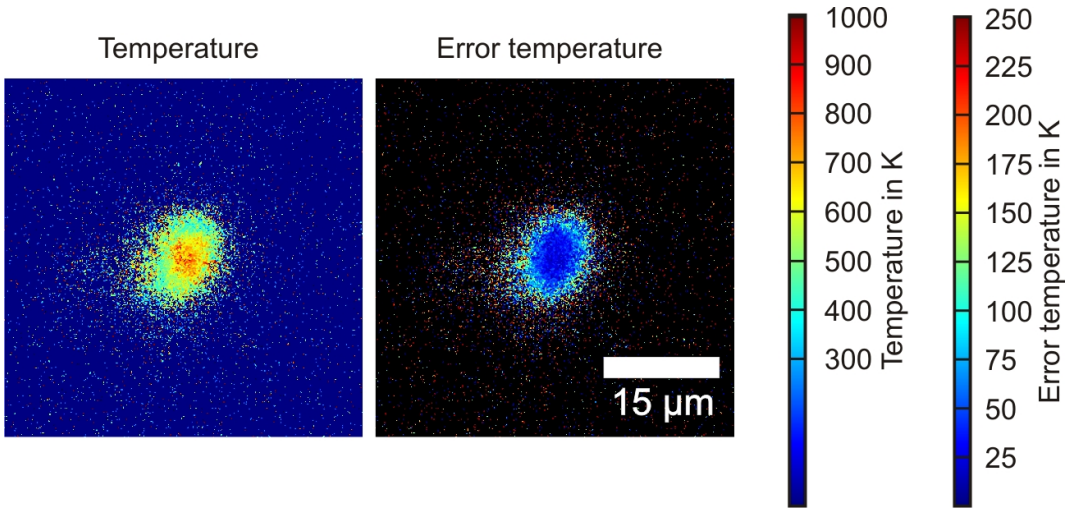

Figure 3.47: 2D temperature graphs of polyimid film with 79 nm thickness. Experimental parameters: delay time of 14 µs, 1 µs integration time, 15 µs laser pulse, fluence 1.56 J/cm^2.

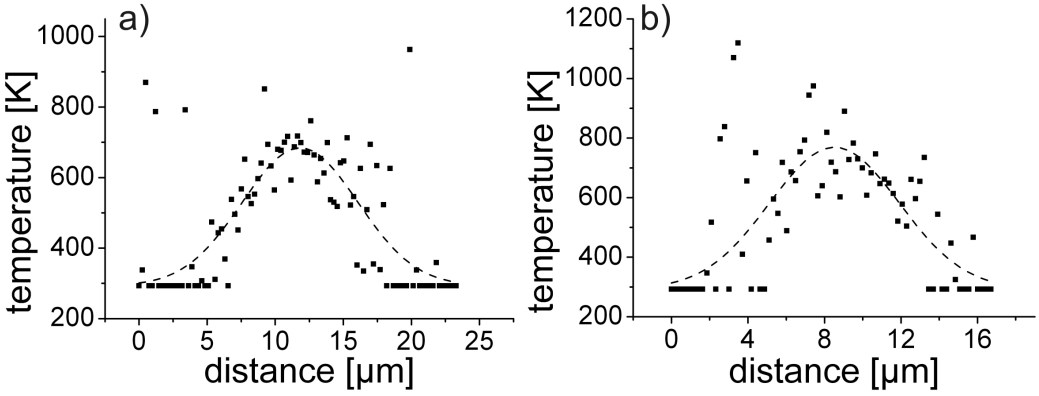

Figure 3.48: Line scan along long (a) and short (b) axis of the hot area in figure 3.47, including Gaussian fit function (dashed line).

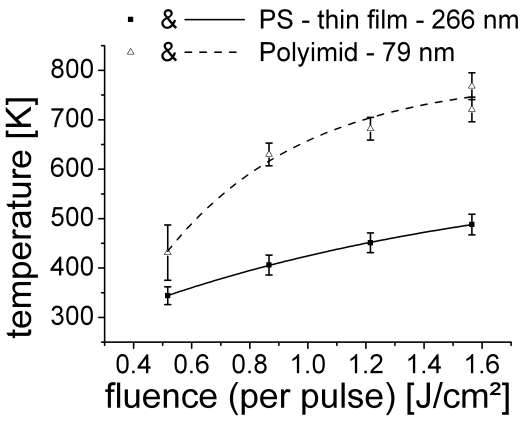

Figure 3.49: Center temperature (averaged over 1.3 × 1.3 µm^2) vs. laser fluence for polyimid film and comparable thin PS film. Experimental parameters: delay time of 14 µs, 1 µs integration time, 15 µs laser pulse. The lines are a guide for the eye.

more laser energy is kept and converted into heat than in the case of the PS film. The general dependence of the temperature versus fluence is comparable. Although even higher similarities could be found when the curve shape is compared to the ones shown for the thick PS or the poly(α-methylstyrene) film in figure 3.43.

Ablation holes can also be found for the applied laser fluences (figure 3.50). Compared to the film thickness, ablation led to relatively deep holes of in average 15 nm (19 % of the film thickness) in the polyimid film at 1.56 J/cm^2. The shape of the holes differed from the shapes for polystyrene and poly(α-methylstyrene). There was no surrounding rim visible and no surface deformation below threshold was observed. With a temperature of 630 ± 23 K, holes of about 6 nm were formed. The polyimid does not show a glass transition in the temperature zone from room temperature up to the degradation temperature (table 3.5). Surface deformation and stress-assisted ablation should therefore not occur. The absence of the typical rim can also be addressed to this fact. The polyimid stays rigid up to degradation so no rim is formed.

The ablation depth versus fluence for the polyimid is plotted similar to the poly(α-methylstyrene) (figure 3.51). Only three points are available from experiments, which

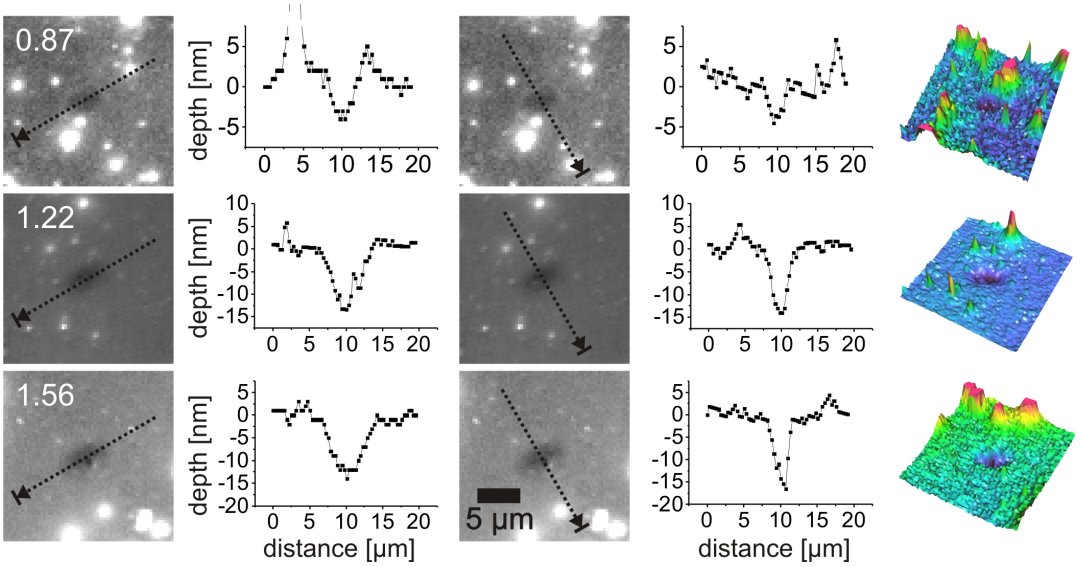

Figure 3.50: Surface profiles images of laser spots of the polyimid film at different fluences (in J/cm^2) including line scans for long and short axis and 3D profiles (acquired with white light confocal profilometry) for 15 µs laser pulses. Fluences are given in the images. Each image shows 20 × 20 µm^2.

suggest a linear dependence in the applied range. A similar trend can also be assumed for the thin polystyrene film. Although the number of data points is actually too small and the error bars are too big to allow a reliable analysis. More experiments, especially with thicker polyimid films, would be necessary to get further inside. The general finding of higher ablation depths for the polyimid film can be addressed to the higher absorption of the polyimid film compared to the PS film.

In order to prove that the polyimid film shows higher thermal stability in laser ablation, as it would be expected, analysis of a plot showing the center temperature versus ablation depth is needed (figure 3.52). Results for polystyrene films with various thicknesses are included. The polyimid was ablated at higher temperatures than polystyrene, as can be seen when the polystyrene mastercurve is compared to the polyimid data. This indicates the higher thermal stability.

A threshold temperature for polyimid can be calculated from the data in this chapter. No polymer is ablated at 431 K. However, holes were formed for temperatures of 630 K

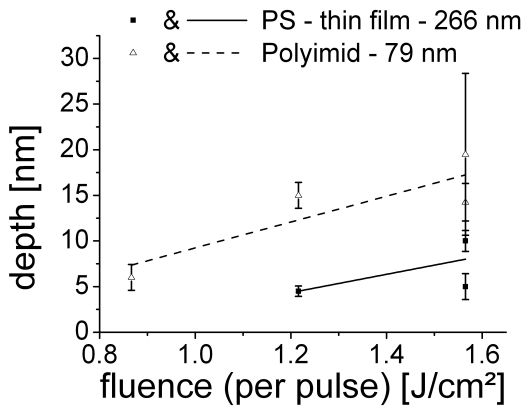

Figure 3.51: Ablation depth vs. laser fluence for polyimid film and comparable thin PS film; 15 µs laser pulse. The lines are a guide for the eye.

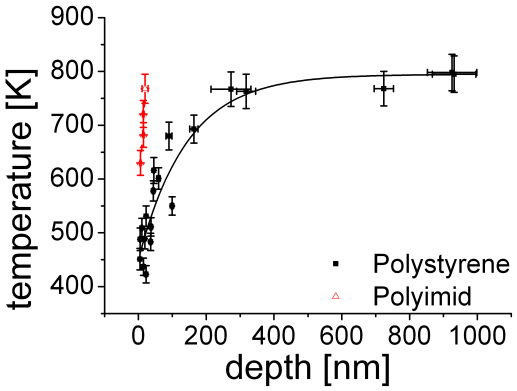

Figure 3.52: Center temperature vs. ablation depth for polyimid film and PS films of various film thicknesses; temperature at center area of 1.3 × 1.3 µm^2, delay time of 14 µs, 1 µs integration time, 15 µs laser pulse. The lines are a guide for the eye.

and higher. The threshold temperature lies consequently between 431 and 630 K. In order to determine the temperature with more precision, a line fit is used (figure 3.53). In that way, a threshold temperature of about 570 K can be deduced. Although, regarding the number and distribution of the data points, this is a rough approximation.

For polyimid, thermal degradation is proposed as the dominant mechanism of ablation, from threshold to high fluences. No evidence for stress-assisted ablation could be found. Compared to thermogravimetric data, the ablation threshold temperature of 570 K is above the start of first degradation of low molecular mass portions at 485 K. With the difference in time scale of eight orders of magnitude, an even higher temperature would have been expected, as discussed in chapter 3.2.2 for polystyrene. However, the data for polystyrene only allows to determine the temperature for a change of dominating mechanism, 750 K (chapter 3.2.6), not for the onset of degradation.

In chapter 3.2.1, the thermal decomposition could also be related to an uneven temperature distribution in the corona in the 2D temperature graphs (figure 3.19 (d)). Whereas a Gaussian shape was found for the polyimid film. However, the temperature distribution has to be brought into context with the film thickness. For a 1 µm polymer film, with ablation of about one third of the film, the amount of ablated material leaving through the gas phase is far higher than for the 79 nm polyimid film with 15 nm deep ablation holes. This can explain the difference in temperature distribution, even though the same mechanism is proposed for the ablation of both, the polyimid and the polystyrene film well above threshold.

With the polyimid, the laser heating and ablation behavior of a polymer without glass transition between room and degradation temperature was analyzed. No surface deformation before threshold and no stress-assisted ablation at threshold was found. In addition, the ablation holes showed a different shape compared to polystyrene or poly(α-methylstyrene), which can be attributed to the absence of a glass transition. The higher thermal stability is also obvious (figure 3.52), although thicker polyimid films would be favorable for a better comparison of the temperature dependence on ablation depth. A threshold temperature for ablation was determined to be about 570 K.

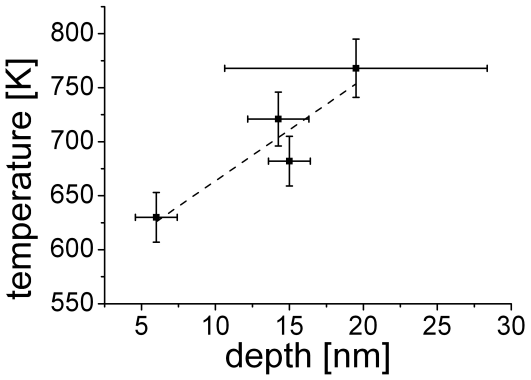

Figure 3.53: Center temperature vs. ablation depth for polyimid film including line fit to find the threshold; temperature at center area of 1.3 × 1.3 µm^2, delay time of 14 µs, 1 µs integration time, 15 µs laser pulse.

3.3.3 Triazene Polymer

When comparing 2D temperature distributions measured on a 369 nm thick triazene polymer film (figure 3.54) to the ones of the 266 nm PS film in chapter 3.2.1 (figure 3.15 (a)), a different behavior is obvious. At the delay time of 14 µs, the core area for the triazene polymer is broader and more circular with about 8 × 8 µm^2 compared to the 4 × 6 µm^2 of the PS film. The corona does not show the typical Gaussian temperature distribution of the thin PS film. In this respect, the temperature graph resembles more the 956 nm thick PS film (figure 3.15 (b)). The inhomogeneous temperature distribution was attributed to the outflow of gaseous decomposition products. The same can be proposed here. The four times higher absorption per film thickness of the triazene polymer film is providing more energy being converted into heat, allowing stronger ablation than in the case of the thin PS film. The polymer is decomposing into gaseous products, inducing the inhomogeneous distribution in the corona. A crescent shaped area is also visible, especially in figure 3.54 at 14 µs delay time. Overall, besides the more circular core area, the 2D temperature graphs are qualitatively similar to the graphs measured for the PS films.

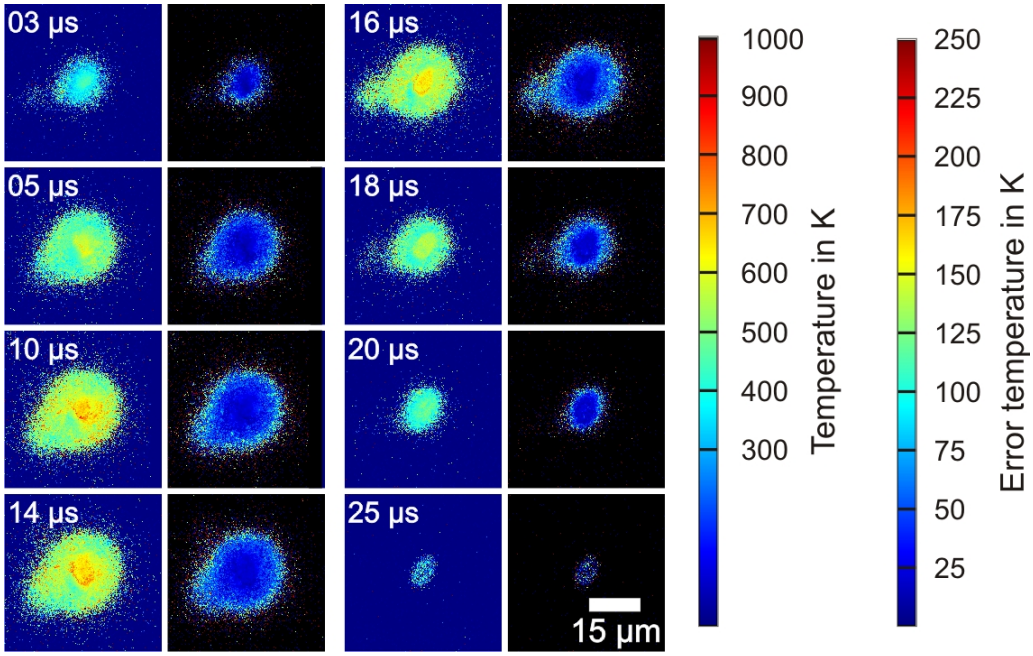

Figure 3.54: 2D temperature and error graphs of triazene polymer film with 369 nm thickness at various delay times (given in the upper left corner). Experimental parameters: 1 µs integration time, 15 µs laser pulse, fluence 1.56 J/cm^2.

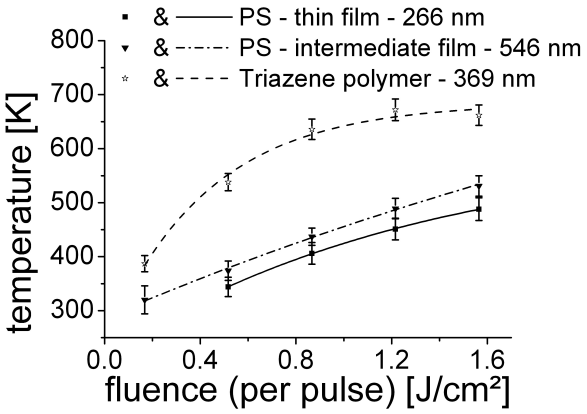

Figure 3.55: Center temperature (averaged over 1.3 × 1.3 µm^2) vs. laser fluence for triazene polymer film and comparable thin PS film. Experimental parameters: delay time of 14 µs, 1 µs integration time, 15 µs laser pulse. The lines are a guide for the eye.

The dependence of temperature versus fluence is presented in figure 3.55. In contrast to both thin PS films with 266 and 546 nm thickness, the fluence shows a different behavior. After a first increase until a fluence of 0.87 J/cm^2, the temperature levels off below 700 K. The higher dye-polymer ratio for the triazene polymer led to a higher energy input than it is the case for both thin polystyrene films. For a polystyrene film of higher dye-polymer ratio or of higher film thickness a similar dependence of temperature versus fluence can be observed, only with a higher plateau temperature. Examples can be found in chapter 3.2.3, figure 3.21 for the 1930 nm PS film or chapter 3.2.6, figure 3.31 (dye concentration and fluence can be exchanged as discussed in chapter 3.2.6).

The surface profiles of the 79 nm triazene polymer film for different fluences are given in figure 3.56. Only a small rim is surrounding the holes. Otherwise, the topography is alike polystyrene ablation holes. Thermogravimetric experiments showed a lower temperature for the start of the degradation than for polystyrene or poly(α-methylstyrene) [75] (compare figure 3.41 respectively table 3.5). The smaller rim can be explained this way. The thermal load at the outer parts of the spot is high enough to decompose the less stable triazene. Whereas the more stable polystyrene and poly(α-methylstyrene) are

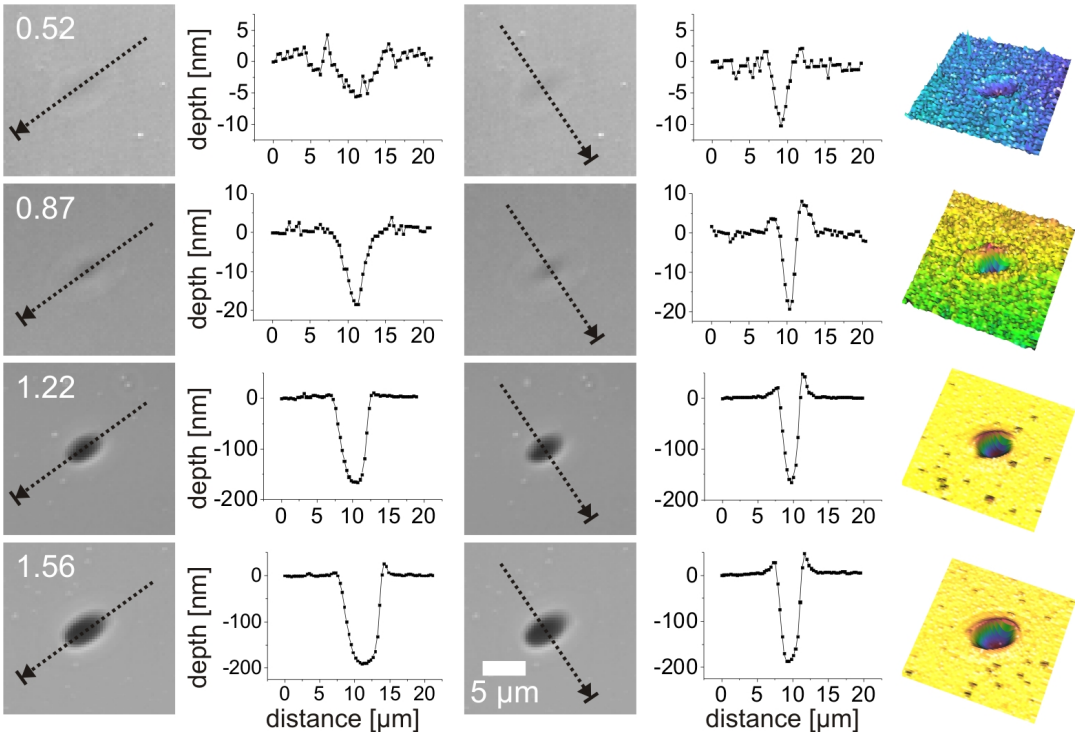

Figure 3.56: Surface profiles images of laser spots of the triazene polymer film at different fluences (in J/cm^2) including line scans for long and short axis and 3D profiles (acquired with white light confocal profilometry) for 15 µs laser pulses. Fluences are given in the images. Each image shows 20 × 20 µm^2.

only deforming. Furthermore, no surface deformation was observed before ablation occurred. However, the step in fluence from 0.17 to 0.52 J/cm^2 is rather big, so it might be occurring in between. In general, stress-assisted ablation was expected for the triazene polymer, but less pronounced than for polystyrene due to the lower glass transition temperature. The glass transition is with 336 K only about 40 K above room temperature. So deformation stresses due to hindered expansion of the polymer should be limited.

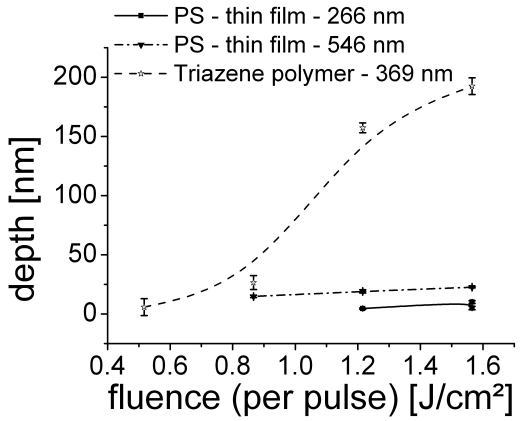

Figure 3.57: Ablation depth vs. laser fluence for triazene polymer film and comparable thick PS film; 15 µs laser pulse. The lines are a guide for the eye.

When plotting the depth of the ablation holes versus fluence the higher dye-polymer ratio induces a drastic increase of ablation for the triazene polymer film. The dependence of the depth corresponds to the finding for the thickest PS film in chapter 3.2.3 (figure 3.22). As already discussed for the poly(α-methylstyrene) and the polyimid, the graph does not allow a conclusion on the thermal stability of the triazene polymer when laser heated.

Therefore the center temperature is plotted versus the ablation depth in combination with the data of polystyrene for various film thicknesses (figure 3.58). While shallow holes are formed at higher temperatures for the triazene polymer, deep holes are found for lower temperatures when compared to the polystyrene mastercurve. A cross-over of the curves is given at about 170 nm and 680 K. Less pronounced stress-assisted ablation was expected for the triazene polymer. At the same time, lower thermal stability should be apparent at elevated temperatures following the result of the thermogravimetric comparison. These two arguments can provide an explanation for the dependence presented in figure 3.58. The polystyrene holes at low temperatures are deeper because higher stresses were effective on the polymer, due to a higher glass transition temperature. At higher temperatures, the thermal degradation is taking over as dominating ablation mechanism. The triazene polymer with its lower thermal stability shows consequently

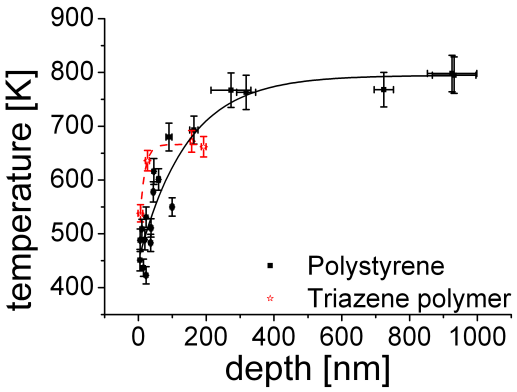

Figure 3.58: Center temperature vs. ablation depth for triazene polymer film and PS films of various film thicknesses; temperature at center area of 1.3 × 1.3 µm^2, delay time of 14 µs, 1 µs integration time, 15 µs laser pulse. The lines are a guide for the eye.

more extensive ablation. The transition temperature can be estimated to be around 650-680 K, with the change in slope in figure 3.58, analogue to the approach for the dye concentration series of polystyrene (chapter 3.2.6, figure 3.35).

An ablation threshold can only be estimated. It lies within the range of 387 ± 15, at which no change could be observed on the illuminated polymer films and 538 ± 16 K with ablation holes (shown in figure 3.56). A line fit based on the last two data points for the triazene polymer in figure 3.59 yields about 510 K. This temperature is well above the glass transition of the polymer, and by 10 K above the degradation temperature at low heating rates. Applying the law of Arrhenius, with the difference in time scales by eight orders of magnitude, thermal degradation should not occur yet. Therefore, the suggested ablation mechanism at threshold would be stress-assisted, just like for polystyrene. The experiments of Furutani et al. [76] support this finding. They could show via nanosecond time-resolved interferometry, that laser heated triazene polymer is expanding below the ablation threshold respectively prior to ablation.

Regarding the temperatures for first surface deformation in combination with the glass transition temperature for polystyrene, a surface deformation was expected for 387 K,

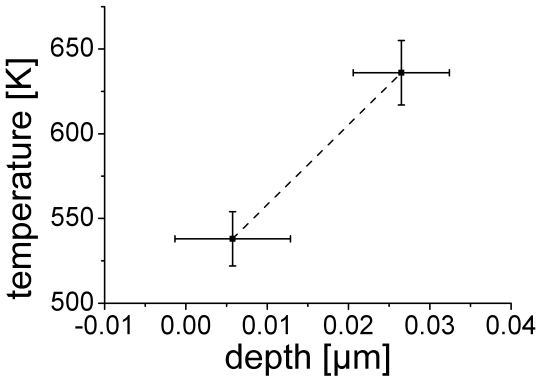

Figure 3.59: Center temperature vs. ablation depth for triazene polymer film including line fit to find the threshold; temperature at center area of 1.3 × 1.3 µm^2, delay time of 14 µs, 1 µs integration time, 15 µs laser pulse.

i.e. at a fluence of 0.17 J/cm^2, but no change was found. Either it goes undetected by the technique in use, confocal white light profilometry, or the glass transition temperature is shifted further to higher temperatures due to the fast heating rates compared to the case of polystyrene.

The results can be compared with a laser heating experiment of the same polymer from literature with a 30 ns laser pulse [74]. In this study, even though conducted with a UV laser, the thermal nature of the mechanism could be proven by variation of film thickness and substrate. Threshold temperatures in the order of 1500 K were determined by modeling the process. A 1D heat conduction model was applied. With the difference of the pulse duration by three orders of magnitude and a spot size of 500 µm, while staying with the film thickness in the 100 nm range, it is reasonable that the influence of the lateral heat diffusion can be neglected. If the law of Arrhenius is applied, this time to compare the result of the temperature measurement to a faster process, the increase in temperature seems overrated. The temperature for the start of thermal degradation is shifted from 500 K on the time scale 60 s (thermogravimetric experiments) to 650-680 K on the time scale of 10 µs for the laser heating as shown in this work. Consequently, a higher temperature in the order of 700-800 K would be

expected for a 30 ns laser pulse. Extensive superheating would therefore be proposed at a temperature of 1500 K calculated by Fardel et al. [74]. This is difficult to justify regarding the studies of Furutani et al. on a slightly different triazene polymer [76]. They could show via nanosecond time-resolved interferometry, that the triazene polymer reacts by expansion and ablation on the 10 ns time scale. Besides, even though the laser ablation process in the studies of Fardel et al. are thermally dominated, a stress-assisted as well as an UV induced photochemical component may not be neglected. Both would rather lower the threshold temperature. The calculation of a temperature for faster pulsed laser heating based on Arrhenius law remains however difficult. A reliable source for the activation energy of the decomposition reaction is not available. Furthermore, the reaction pathway of the thermal decomposition reaction might be altered by the fast pulsed heating.

In summary, a higher ablation threshold temperature and a less pronounced stress-assisted ablation was found for the triazene polymer than for polystyrene. This could be addressed to the lower glass transition temperature and the lower stresses due to hindered expansion in the glassy state. At higher fluences, the lower thermal stability of the triazene polymer led to a more pronounced ablation than it was found for polystyrene as expected.

A comparison to the threshold temperature proposed in literature yielded a notable deviation. However, the differences in experimental setup, especially in laser pulse time scale and wavelength might be responsible for this deviation.

4 Summary and conclusion

It was demonstrated that temperature measurements based on spectral pyrometry are well applicable in order to analyze laser heating effects on polymers. A time resolution of 1 µs and a spatial resolution of 1 µm was achieved. The general approach of data analysis, making use of the Wien approximation was discussed. An influence of the emissivity on the analysis was considered but could be ruled out as important factor. Heatable atomic force cantilever were chosen for a reference measurement. In this way, it could be shown that the temperature measurement setup can be applied beyond laser heating applications. In addition, it could be proven that the heated air is also contributing to the thermal radiation signal and consequently visible in the temperature graphs.

Laser heating and ablation behavior of various polymers including polystyrene of different molecular weights, poly(α-methylstyrene), a polyimid and a triazene polymer were investigated. Therefore, dye-sensitized films of the polymers were illuminated by laser light of various laser fluences. The 2D temperature profiles and the time dependent temperature behavior was studied.

Full 3D finite element simulations were conducted for polystyrene films. This was especially important to understand the influence of sample parameters like the film thickness and dye concentration. Ablation or phase changes of the polymer were neglected in the simulations. Nevertheless, the time dependent behavior of the temperature in the center of the spot could well be followed if an energy loss was considered as long as ablation was limited. For extensive ablation, a drastic lower center temperature was obtained than predicted by simulations. Comparison of measured and simulated 2D temperature graphs revealed the effect of ablation on the measurement. Heated air and hot,

outflowing gaseous material was visible for the detector just like the heated surface. An inhomogeneous temperature distribution was caused surrounding the spot. Overall, through the combination of measured and simulated data, the laser heating behavior on the microsecond time scale could well be understood and predicted.

Two different ablation mechanism could be identified for photothermal laser ablation of polymers on the 10 µs time scale, photomechanical or stress-assisted ablation and ablation due to thermal decomposition. A photomechanical or stress-assisted ablation was found for polymers with a glass transition between room temperature and the degradation temperature. In this case, stress was generated due to the hindered thermal expansion in the glassy state. At the transition, the polymer got softer and was able to expand locally, normal to the surface. If a critical stress was exceeded, material was accelerated from the surface at the transition, i.e. ablation occurred. The ablation threshold temperature for these polymers was determined to be several 10 K above the glass transition temperature. At higher fluences and thus higher temperatures, thermal decomposition took over as dominating ablation mechanism. For polymers which do not undergo glass transition in the range between room temperature and the degradation temperature, thermal decomposition was found at the ablation threshold. For these polymers, the ablation threshold temperature depends on the thermal stability. Due to the fast heating rates in laser ablation, temperatures found in thermogravimetric experiments for the onset of degradation were shifted to higher temperatures in agreement with the law of Arrhenius.

An extensive superheating of microsecond laser heated polymers could not be observed at threshold, as it is discussed in literature. Even for high temperatures measured for high laser fluences, it is questionable if the polymer is superheated or if the heated matter consists of hot air or hot products from the degradation process.

In the case of polymers undergoing stress-assisted ablation, different molecular weights also showed differences in ablation behavior. The lower glass transition and viscosity above glass transition led to a higher ablation threshold temperature. In addition, the extent of the features formed after laser irradiation were altered due to the lower

viscosity above glass transition for low molecular weights. Surface deformation peaks below ablation threshold were more pronounced and depths of ablation holes at higher fluences were decreased. However, more detailed studies would be necessary to quantify the dependence of the ablation threshold temperature and the extent of the feature sizes on molecular weight.

5 Outlook

With the knowledge acquired in this work, it is possible to investigate more complex laser heating problems. Ablation on samples with high surface roughness can be one example. Besides, the analysis of laser induced film formation of latex particles becomes possible to interpret. Ablation is typically an unwanted side effect. Film formation is based on the laser induced glass to rubber transition of the polymer, just like photomechanical or stress-assisted ablation. The understanding of the basics in ablation mechanism allows the modification of the material or laser parameters, like illumination time in order to avoid or at least minimize the effect.

Furthermore, the reference measurement of the heatable cantilever gives raise to the extension of the measurement method to fields in which heat transfer physics at small size scales or fast time scales matter. The distance between a surface and a heatable tip of an atomic force microscope is for example crucial for its heat transfer and its temperature. If the sample surface is well defined, this problem can be calculated or simulated. With the temperature measurement method used in this work, a confirmation of such a calculation or simulation is possible. For more complex surfaces which are curved or rough and on which simulation can not be conducted easily, experimental data can be crucial for identification and understanding of the important physical processes.

Bibliography

[1] D.E. Hare, J. Franken, and D.D. Dlott. Coherent raman measurements of polymer thin-film pressure and temperature during picosecond laser-ablation. *J. Appl. Phys.*, 77(11):5950, 1995.

[2] I.Y.S. Lee, X.N. Wen, W.A. Tolbert, D.D. Dlott, M. Doxtader, and D.R. Arnold. Direct measurement of polymer temperature during laser ablation using a molecular thermometer. *J. Appl. Phys.*, 72(6):2440, 1992.

[3] S. Kuper, J. Brannon, and K. Brannon. Threshold behavior in polyimide photoablation - single-shot rate measurements and surface-temperature modeling. *Appl. Phys. A-Mater.*, 56(1):43, 1993.

[4] S.L. Johnson, D.M. Bubb, and R.F. Haglund. Phase explosion and recoil-induced ejection in resonant-infrared laser ablation of polystyrene. *Appl. Phys. A-Mater.*, 96(3):627, 2009.

[5] A.N. Magunov. Spectral pyrometry (review). *Instrum. Exp. Tech.+*, 52(4):451, 2009.

[6] S.G. Garanin and O.N. Krokhin. High-power lasers and laser fusion. *Her. Russ. Acad. Sci.+*, 81(3):204, 2011.

[7] D. Meschede. *Gerthsen Physik*. Springer-Verlag, Berlin, Heidelberg, New York, 23th edition edition, 2006. p.841.

[8] J.C. Miller and R.F. Haglund. *Laser Ablation and Desorption*. Academic Press, San Diego, 1998.

[9] J.D. Majumdar and I. Manna. Laser processing of materials. *Sadhana-Acad. P. Eng. S.*, 28:495, 2003.

[10] T. Lippert. *Laser application of polymers*, volume 168 of *Polymers and Light*. Springer-Verlag Berlin, Berlin, 2004. 51-246.

[11] S.G. Koulikov and D.D. Dlott. Ultrafast microscopy of laser ablation of refractory materials: ultra low threshold stress-induced ablation. *J. Photoch. Photobio. A*, 145(3):183, 2001.

[12] I. Itzkan, D. Albagli, M.L. Dark, L.T. Perelman, C. von Rosenberg, and M.S. Feld. The thermoelastic basis of short pulsed-laser ablation of biological tissue. *P. Natl. Acad. Sci. USA*, 92(6):1960, 1995.

[13] C.L. Beyler and M.M. Hirschler. Thermal decomposition of polymers. In P. J. DiNenno and pp., editors, *SFPE Handbook of Fire Protection Engineering*, page 1110. NFPA, Quincy, 3rd edition edition, 2001.

[14] S.L. Malhotra, J. Hesse, and L.-P. Blanchard. Thermal decomposition of polystyrene. *Polymer*, 16(2):81, 1975.

[15] J. Mullens, R. Carleer, G. Reggers, M. Ruysen, J. Yperman, and L.C. Vanpoucke. The oxidative-degradation of polystyrene studied by the coupling of thermogravimetry with other techniques. *B. Soc. Chim. Belg.*, 101(4):267, 1992.

[16] R. Larciprete and M. Stuke. Direct observation of excimer-laser photoablation products from polymers by picosecond-uv-laser mass-spectroscopy. *Appl. Phys. B-Photo.*, 42(3):181, 1987.

[17] H. Fukumura, N. Mibuka, S. Eura, H. Masuhara, and N. Nishi. Mass-spectrometric studies on laser-ablation of polystyrene sensitized with anthracene. *J. Phys. Chem.*, 97(51):13761, 1993.

[18] D. M. Bubb, M. R. Papantonakis, J. S. Horwitz, R. F. Haglund, B. Toftmann, R. A. McGill, and D. B. Chrisey. Vapor deposition of polystyrene thin films by intense laser vibrational excitation. *Chem. Phys. Lett.*, 352(3-4):135, 2002.

[19] D. M. Bubb, B. Toftmann, R. F. Haglund, J. S. Horwitz, M. R. Papantonakis, R. A. McGill, P. W. Wu, and D. B. Chrisey. Resonant infrared pulsed laser deposition of thin biodegradable polymer films. *Appl. Phys. A-Mater.*, 74(1):123, 2002.

[20] S. L. Johnson, H. K. Park, and R. F. Haglund. Properties of conductive polymer films deposited by infrared laser ablation. *Appl. Surf. Sci.*, 253(15):6430, 2007.

[21] R. Srinivasan. Ablation of polymers and biological tissue by ultraviolet-lasers. *Science*, 234(4776):559, 1986.

[22] T. Lippert. Interaction of photons with polymers: From surface modification to ablation. *Plasma Process. Polym.*, 2(7):525, 2005.

[23] T. Lippert, R.L. Webb, S.C. Langford, and J.T. Dickinson. Dopant induced ablation of poly(methyl methacrylate) at 308 nm. *J. Appl. Phys.*, 85(3):1838, 1999.

[24] S.G. Koulikov and D.D. Dlott. Time-resolved microscopy of laser photothermal imaging. *Opt. Photonics News*, 11(6):26, 2000.

[25] T. Masubuchi, H. Furutani, H. Fukumura, and H. Masuhara. Laser-induced nanometer-nanosecond expansion and contraction dynamics of poly(methyl methacrylate) film studied by time-resolved interferometry. *J. Phys. Chem. B*, 105(13):2518, 2001.

[26] I. Bozsoki, B. Balogh, and P. Gordon. 355 nm nanosecond pulsed nd:yag laser profile measurement, metal thin film ablation and thermal simulation. *Opt. Laser Technol.*, 43(7):1212, 2011.

[27] I. Apitz and A. Vogel. Material ejection in nanosecond er : Yag laser ablation of water, liver, and skin. *Appl. Phys. A-Mater.*, 81(2):329, 2005.

[28] G. Bounos, A. Kolloch, T. Stergiannakos, E. Varatsikou, and S. Georgiou. Assessment of the attained temperatures and of melting in the nanosecond irradiation of doped poly(methylmethylacrylate) at 308, 248, and 193 nm via the examination of dopant reactivity. *J. Appl. Phys.*, 98(8):9, 2005.

[29] E. Rebollar, G. Bounos, A. Selimis, M. Castillejo, and S. Georgiou. Examination of the influence of molecular weight on polymer laser ablation: polystyrene at 248 nm. *Appl. Phys. A, Mater.*, 92(4):279, 2008.

[30] H.N. Yu, D.D. Dlott, and R.R. Kearney. Time-resolved microscopy analysis of laser photothermal imaging media. *J. Imaging Sci. Techn.*, 50(5):401, 2006.

[31] J. Bohandy, B.F. Kim, and F.J. Adrian. Metal deposition from a supported metal-film using an excimer laser. *J. Appl. Phys.*, 60(4):1538, 1986.

[32] D.P. Banks, K. Kaur, R. Gazia, R. Fardel, M. Nagel, T. Lippert, and R.W. Eason. Triazene photopolymer dynamic release layer-assisted femtosecond laser-induced forward transfer with an active carrier substrate. *Epl-Europhys. Lett.*, 83(3):6, 2008.

[33] R. Fardel, M. Nagel, F. Nuesch, T. Lippert, and A. Wokaun. Fabrication of organic light-emitting diode pixels by laser-assisted forward transfer. *Appl. Phys. Lett.*, 91 (6):3, 2007.

[34] D.B. Chrisey, A. Doraiswamy, R.J. Narayan, T. Lippert, L. Urech, A. Wokaun, M. Nagel, B. Hopp, M. Dinescu, R. Modi, and R.C.Y. Auyeung. Excimer laser forward transfer of mammalian cells using a novel triazene absorbing layer. *Appl. Surf. Sci.*, 252(13):4743, 2006.

[35] P. Serra, M. Duocastella, J.M. Fernandez-Pradas, and J.L. Morenza. Liquids microprinting through laser-induced forward transfer. *Appl. Surf. Sci.*, 255(10):5342, 2009.

[36] M.S. Brown, N.T. Kattamis, and C.B. Arnold. Time-resolved dynamics of laser-induced micro-jets from thin liquid films. *Microfluid. Nanofluid.*, 11(2):199, 2011.

[37] C.B. Arnold, P. Serra, and A. Pique. Laser direct-write techniques for printing of complex materials. *MRS Bull.*, 32(1):23, 2007.

[38] F.P. Incropera and DeWitt D.P. *Introduction to Heat Transfer*. Wiley, New York, 1.edition edition, 1985.

[39] A. Majumdar. Scanning thermal microscopy. *Annu. Rev. Mater. Sci.*, 29:505, 1999.

[40] C.C. Williams and H.K. Wickramasinghe. Scanning thermal profiler. *Appl. Phys. Lett.*, 49(23):1587, 1986.

[41] V.A. Kopev, I.A. Kossyi, A.N. Magunov, and N.M. Tarasova. Thermometry based on the intensity distribution in a thermal-radiation spectrum. *Instrum. Exp. Tech.+*, 49(4):573, 2006.

[42] S.C. Gupta, S.G. Love, and T.J. Ahrens. Shock temperature in calcite (caco(3)) at 95-160 gpa. *Earth Planet. Sci. Lett.*, 201(1):1, 2002.

[43] D.A. Boness and J.M. Brown. Bulk superheating of solid kbr and csbr with shock-waves. *Phys. Rev. Lett.*, 71(18):2931, 1993.

[44] S. Rekhi, J. Tempere, and I.F. Silvera. Temperature determination for nanosecond pulsed laser heating. *Rev. Sci. Instrum.*, 74(8):3820, 2003.

[45] G.M. Batanov, N.K. Berezhetskaya, V.A. Kop'ev, I.A. Kossyi, and A.N. Magunov. Thermometry of microwave discharge in powder mixtures by the thermal radiation spectrum. *High Temp.*, 46(1):124, 2008.

[46] F. Seronde, P. Echegut, J.P. Coutures, and F. Gervais. Emissivity of oxides - a microscopic approach to glass coatings. *Mater. Sci. Eng. B-Solid State Mater. Adv. Technol.*, 8(4):315, 1991.

[47] O. Rozenbaum, D.D. Meneses, Y. Auger, S. Chermanne, and P. Echegut. A spectroscopic method to measure the spectral emissivity of semi-transparent materials up to high temperature. *Rev. Sci. Instrum.*, 70(10):4020, 1999.

[48] H. Tanaka, S. Sawai, K. Morimoto, and K. Hisano. Evaluation of hemispherical total emissivity for thermal radiation calorimetry. *Int. J. Thermophys.*, 21(4):927, 2000.

[49] S. Chen, I.Y.S. Lee, W.A. Tolbert, X.N. Wen, and D.D. Dlott. Applications of ultrafast temperature jump spectroscopy to condensed phase molecular dynamics. *J. Phys. Chem.*, 96(18):7178, 1992.

[50] X.N. Wen, W.A. Tolbert, and D.D. Dlott. Multiphonon up-pumping and molecular hot-spots in superheated polymers studied by ultrafast optical calorimetry. *Chem. Phys. Lett.*, 192(2-3):315, 1992.

[51] X.N. Wen, W.A. Tolbert, and D.D. Dlott. Ultrafast temperature-jump in polymers - phonons and vibrations heat up at different rates. *J. Chem. Phys.*, 99(5):4140, 1993.

[52] J. Brandrup, E.H. Immergut, and E.A. Grulke. *Polymer Handbook*. Wiley, New York, 4.th edition edition, 1999. V 87-96.

[53] D.E. Hare and D.D. Dlott. Picosecond coherent raman-study of solid-state chemical-reactions during laser polymer ablation. *Appl. Phys. Lett.*, 64(6):715, 1994.

[54] C. Kohl, T. Weil, J. Q. Qu, and K. Mullen. Towards highly fluorescent and water-soluble perylene dyes. *Chem.-Eur. J.*, 10(21):5297, 2004.

[55] Y. Geerts, H. Quante, H. Platz, R. Mahrt, M. Hopmeier, A. Bohm, and K. Mullen. Quaterrylenebis(dicarboximide)s: near infrared absorbing and emitting dyes. *J. Mater. Chem.*, 8(11):2357, 1998.

[56] T. Weil, T. Vosch, J. Hofkens, K. Peneva, and K. MÃ$\frac{1}{4}$llen. The rylene colorant family - tailored nanoemitters for photonics research and applications. *Angew. Chem. Int. Edit.*, 49(48):9068, 2010.

[57] A. Rademacher, S. Markle, and H. Langhals. Soluble perylene fluorescent dyes with high photostability. *Chem. Ber.-Recl.*, 115(8):2927, 1982.

[58] A.C. Grimsdale and K. Mullen. The chemistry of organic nanomaterials. *Angew. Chem. Int. Edit.*, 44(35):5592, 2005.

[59] Y. Avlasevich, C. Li, and K. Mullen. Synthesis and applications of core-enlarged perylene dyes. *J. Mater. Chem.*, 20(19):3814, 2010.

[60] R.S. Kappes, C. Li, H.-J. Butt, and J.S. Gutmann. Time-resolved, local temperature measurements during pulsed laser heating. *New J. Phys.*, 12:10, 2010.

[61] R.S. Kappes, F. Schoenfeld, C. Li, J.S. Gutmann, and H.-J. Butt. Temperature analysis of laser heated polymers on microsecond time scales. *Appl. Phys. A-Mater.*, 106(4):791, 2012.

[62] R.S. Kappes. *Desing und Aufbau einer Temperaturemessstation zur Untersuchung von Laserheizeffekten bei Polymerfilmen.* Diplomarbeit. University Mainz, Mainz, 2008.

[63] F. Davard and D. Dupuis. Flow visualisation experiments in a blade coating process. *J. Non-Newton. Fluid*, 93(1):17, 2000.

[64] S.G. Hahm, S. Choi, S.H. Hong, T.J. Lee, S. Park, D.M. Kim, J.C. Kim, W. Kwon, K. Kim, M.J. Kim, O. Kim, and M. Ree. Electrically bistable nonvolatile switching devices fabricated with a high performance polyimide bearing diphenylcarbamyl moieties. *J. Mater. Chem.*, 19(15):2207, 2009.

[65] Y. Avlasevich, S. Muller, P. Erk, and K. Mullen. Novel core-expanded rylenebis(dicarboximide) dyes bearing pentacene units: Facile synthesis and photophysical properties. *Chem.-Eur. J.*, 13(23):6555, 2007.

[66] Y. Sakakibara, I. Yamada, S. Hiraoka, and T. Aragaki. Thermal-conductivity of polystyrene above and below the glass-transition temperature. *J. Chem. Eng. Jpn.*, 23(4):499, 1990.

[67] E. Marti, E. Kaisersberger, and E. Moukhina. Heat capacity functions of polystyrene in glassy and in liquid amorphous state and glass transition dsc and tmdsc study. *J. Therm. Anal. Calorim.*, 85(2):505, 2006.

[68] R.D. Lide. *CRC Handbook of Chemistry and Physics*. CRC Press, Boca Raton, 87th edition edition, 2006. Chap. 12, p.207.

[69] J. Huang and P.K. Gupta. Temperature dependence of the isostructural heat capacity of a soda lime silicate glass. *J. Non-Cryst. Solids*, 139(3):239, 1992.

[70] T. Mito and H. Masuhara. Laser-induced nanometer expansion and contraction dynamics of polystyrene films depending on its molecular weight. *Appl. Surf. Sci.*, 197:796, 2002.

[71] R. Greiner and F.R. Schwarzl. Thermal contraction and volume relaxation of amorphous polymers. *Rheol. Acta*, 23(4):378, 1984.

[72] C. M. Roland, K. L. Ngai, and D. J. Plazek. Modes of molecular motion in low molecular weight polystyrene. *Macromolecules*, 37(18):7051, 2004.

[73] R. Buchdahl, L. E. Nielsen, and E. H. Merz. Rheology of thermoplastics .2. recoverable and nonrecoverable deformations of polystyrene between 90-degrees-c and 240-degrees-c as a function of molecular weight. *J. Polym. Sci.*, 6(4):403, 1951.

[74] R. Fardel, M. Nagel, T. Lippert, F. Nuesch, A. Wokaun, and B. S. Luk'yanchuk. Influence of thermal diffusion on the laser ablation of thin polymer films. *Appl. Phys. A-Mater.*, 90(4):661, 2008.

[75] O. Nuyken, J. Stebani, T. Lippert, A. Wokaun, and A. Stasko. Synthesis and characterization of novel triazeno-group containing photopolymers. *Macromol. Chem. Physic.*, 196(3):739, 1995.

[76] H. Furutani, H. Fukumura, H. Masuhara, T. Lippert, and A. Yabe. Laser-induced decomposition and ablation dynamics studied by nanosecond interferometry .1. a triazenopolymer film. *J. Phys. Chem. A*, 101(32):5742, 1997.

List of publications

R.S. Kappes, C. Li, H.-J. Butt, J.S. Gutmann. Time-resolved, local temperature measurement during pulsed laser heating. *New J. Phys.*,12:10, **2010**.

R.S. Kappes, F. Schoenfeld, C. Li, J.S. Gutmann, H.-J. Butt. Temperature analysis of laser heated polymers on microsecond time scales. *Appl. Phys. A-Mater.*, 106:791, **2012**

S. Lenz, M. Bonini, S.K. Nett, M.C. Lechmann, S.G.J. Emmerling, **R.S. Kappes**, M. Memesa, A. Timmann, S.V. Roth, J.S. Gutmann. Global scattering functions: a tool for grazing incidence small angle X-ray scattering (GISAXS) data analysis of low correlated lateral structures. *Eur. Phys. J.-Appl. Phys.*, 51:10601, **2010**

J.W. Ochsmann, S. Lenz, S.G.J. Emmerling, **R.S. Kappes**, S.K. Nett, M.C. Lechmann, S.V. Roth, J.S. Gutmann. PS-b-PEO Block Copolymer Thin Films as Structured Reservoirs for Nanoscale Precipitation Reactions. *J. Polym. Sci. Pol. Phys.*, 48(14):1569, **2010**

List of presentations

24.03.2009

Tagung der Deutschen Phyiskalischen Gesellschaft, Dresden, Germany

R.S. Kappes and J.S. Gutmann, *Investigation of Laser Heating Effects on Polymer Films* **(poster presentation)**

08.06.2009

Frontiers in Polymer Science, Mainz, Germany

R.S. Kappes and J.S. Gutmann, *Investigation of Laser Heating Effects on Polymer Films* **(poster presentation)**

22.03.2010

Tagung der Deutschen Phyiskalischen Gesellschaft, Regensburg, Germany

R.S. Kappes, J.S. Gutmann, *Temperature Measurements within a Laser Heating Process on Polymer Films* **(oral presentation)**

10.06.2010

Spring Meeting of the European Material Research Society, Strasbourg, France

R.S. Kappes and J.S. Gutmann, *Temperature Measurements during a Laser Heating Process on Polymer Films* **(poster presentation)** awarded with the poster prize

29.04.2011

Spring Meeting of the Material Research Society, San Francisco, CA, USA

R.S. Kappes, J.S. Gutmann, H.-J. Butt, *Time-resolved, local Temperature Measurements during pulsed Laser Heating* **(oral presentation)**